This manuscript is a non-peer reviewed preprint submitted to EarthArXiv

Title: Single-blind test of nine methane-sensing satellite systems from three continents

Authors: Evan D. Sherwin[1,*], Sahar H. El Abbadi[1], Philippine M. Burdeau[1], Zhan Zhang[1], Zhenlin Chen[1], Jeffrey S. Rutherford[1,a], Yuanlei Chen[1], Adam R. Brandt[1]

Author Affiliations:

[1] Department of Energy Science & Engineering, Stanford University, Stanford, California 94305, United States

[a] Present affiliation: Highwood Emissions Management, Calgary, Alberta T2P 2V1, Canada

[*] Correspondence: evands@stanford.edu

Abstract

Satellite-based remote sensing enables detection and mitigation of large point sources of climate-warming methane. These satellites will have the greatest impact if stakeholders have a clear-eyed assessment of their capabilities. We performed a single-blind test of nine methane-sensing satellites from three continents and five countries, including both commercial and government satellites. Over two months, we conducted 82 controlled methane releases during satellite overpasses. Six teams analyzed the resulting data, producing 134 estimates of methane emissions. Of these, 80 (58%) were correctly identified, with 46 true positive detections (34%) and 34 true negative non-detections (25%). There were 41 false negatives and 0 false positives, in which teams incorrectly claimed methane was present. All eight satellites that were given a nonzero emission detected methane at least once, including the first single-blind evaluation of the EnMAP, Gaofen 5, and Ziyuan 1 systems. In percent terms, quantification error across all satellites and teams is similar to aircraft-based methane remote sensing systems, with 55% of mean estimates falling within ±50% of the metered value. Although teams correctly detected emissions as low as 0.03 metric tons of methane per hour, it is unclear whether detection performance in this test is representative of real-world field performance. Full retrieval fields submitted by all teams suggest that in some cases it may be difficult to distinguish true emissions from background artifacts without a known source location. Cloud interference is significant and appears to vary across teams and satellites. This work confirms the basic efficacy of the tested satellite systems in detecting and quantifying methane, providing additional insight into detection limits and informing experimental design for future satellite-focused controlled methane release testing campaigns.

Keywords:
Methane, hyperspectral imaging, remote sensing, satellite, single-blind, controlled release

Satellite-based remote sensing systems continue to find large point-source emissions of climate-warming methane across the globe [1–8]. Such systems empower stakeholders in industry and government to take corrective action, both to mitigate individual sources and to inform estimates of total methane emissions, particularly in oil and natural gas systems, where many of the largest sources have been observed [1–12].

A considerable fleet of point-source methane-sensing satellites is now in orbit, including purpose-built and repurposed instruments [13]. In the coming years, this number will increase substantially [13].

These satellites will have the greatest positive environmental impact if their results are widely believed by a broad array of stakeholders across the world. Single-blind controlled methane release testing, in which teams estimate methane emissions from a metered source without knowing the true value, is an important and widely-used method of independently determining the capabilities of a methane sensing system [14–20].

In the first such single-blind release testing satellite systems, Sherwin et al. tested five satellites: the commercial GHGSat-C and WorldView-3 systems and the government-supported PRISMA, LandSat 8, and Sentinel-2 systems. In that study five teams analyzed data from different subsets of these satellites [14]. This test demonstrated that, across the array of these five satellites, this

approach can be used to detect emissions ranging from 0.20 [0.19, 0.21] metric tons of methane per hour (henceforth t/h), for the most sensitive systems, to 7.2 [6.8, 7.6] t/h. Relative quantification error was comparable to aircraft-based methane sensing systems [14]. Sample size was modest, however, with some satellites collecting only one measurement, limiting generalizability of the results without additional data collection.

In addition, several methane-sensing satellites have launched since the previous test concluded in 2021, including the German EnMAP system and the Chinese Gaofen 5-02 Advanced Hyperspectral Imager (GF5) and Ziyuan 1-02E Advanced Hyperspectral Imager (ZY1) [21–23]. Although these satellites were not primarily designed to sense methane, scientists have used similar systems to detect substantial methane point sources from oil and natural gas infrastructure [24].

This work conducts single-blind testing of nine distinct satellite systems, focusing on detection and quantification performance for releases ranging from 0.03-1.6 t/h. In addition, we take steps to evaluate the generalizability of our results through a highly transparent experimental design, in which all teams submit full methane retrievals for the scene surrounding the release. This approach provides insight into which identified methane emissions are unambiguously detected and which might be difficult to distinguish from artifacts if the source location were not known.

Materials and Methods

We employed a fixed-location single-blind controlled methane release experimental design to evaluate point-source methane sensing systems from October 10th to November 30th. Participating teams were aware of the existence, timeframe, and precise location coordinates of the test. Teams were not informed during a given observation whether gas would be released, nor of the size of released emissions. Teams were informed of an approximate upper bound of 1.5 t/h. Teams were not given the precise configuration of Stanford equipment on the ground, though large equipment may have been visible from space in some cases.

Metered controlled release volumes – including releases with zero-volume – were retained by the Stanford team and not given to teams until all estimates were submitted by all participants for all stages of the test. Analysts estimated the presence and magnitude of methane emissions for each overpass, with a reporting approach in compliance with the Advancing Development of Emissions Detection (ADED) protocol for airplane and satellite systems [25]. More information is provided in the Supporting Information (SI), Section S.1.1.

We performed releases during overpasses of nine satellite constellations: the commercial satellites GHGSat-C (GSC) of Canada and the US-based WorldView-3 (WV3), as well as publicly-funded satellites, including the German Environmental Mapping and Analysis Program (EnMAP), the Chinese Gaofen 5 (GF5), Ziyuan 1 (ZY1), and Huanjing 2 (HJ2), the Italian PRecursore IperSpettrale della Missione Applicativa (PRISMA), the US LandSat (LS) 8 and 9, and the pan-European Sentinel-2 [26–29,21,30–32,23,33]. With the exception of the GHGSat-C constellation, none of these satellites was explicitly designed for methane sensing, but their data have instead been applied to this end. Analysis teams first attempted to estimate emissions volumes using available data from satellites and wind reanalysis products. In some cases,

multiple teams assessed the same observation from an instrument, providing an opportunity to empirically assess variability due to source quantification algorithms, which participating teams were not required to release. See the SI, Section S3 for the details each team elected to share about their algorithms.

These satellites range from high-sensitivity/narrow swath to low-sensitivity/large swath, as illustrated in Table 1. Revisit time is also anticorrelated with instrument sensitivity. The Sentinel-2 and LandSat 8/9 systems have estimated detection limits of roughly 1-5 t/h [34], but each satellite in these constellations covers the bulk of the world's landmass every 10-16 days with a swath of 185-290 km [31,35]. GHGSat, EnMAP, GF5, PRISMA, WorldView-3, and ZY1 are targeted "point-and-shoot" systems, with higher resolution but narrower swaths of 12-60 km [26–29,21,30,23]. Existing publicly available information does not specify whether HJ2 is targeted or has global coverage, but its swath of 800 km suggests it is capable of global coverage [33]. See the SI, Section S1 for additional discussion of the capabilities of each satellite system.

Table 1. Key characteristics of each participating satellite constellation, from lowest to highest swath width, which is roughly proportional to an instrument's minimum methane detection limit. Global coverage refers to a configuration that passively covers most of Earth's surface over some number of orbits, while targeted coverage refers to a "point-and-shoot" instrument that must be pointed to a particular location. Constellation size includes only active satellites. Adapted with permission from Sherwin et al. 2023 [14].

Satellite	Coverage	Constellation size	Swath [km]	~Revisit time (per satellite)	Data availability
GHGSat-C [26,27]	Targeted	8[§]	12	14 days	Commercial
WorldView-3 [28]	Targeted	1	13.1	4.5 days[‡]	Commercial
PRISMA [29]	Targeted	1	30	7 days	Public
EnMAP [21]	Targeted	1	30	27 days[†]	Public
Gaofen 5 (GF5) [30,36,37]	Targeted	1	60	5-8 days[*]	Government
Ziyuan 1 (ZY1) [23]	Targeted	1	60	1-3 days[*]	Government
Landsat 8/9 [31]	Global	2	185	16 days	Public
Sentinel-2 [35]	Global	2	290	10 days	Public
Huanjing 2 (HJ2) [33]	Global	2	800	≤4 days[*]	Government

[§]Three of these GHGSat C satellites were launched after the conclusion of testing.
[‡]For best resolution within 20° off nadir. WorldView-3 has 1-day revisit time at lower guaranteed resolution.
[†]For best resolution within 30° off nadir. EnMAP has 4-day revisit time at lower guaranteed resolution [13].
[*]Revisit times for GF5, ZY1, and HJ2 are inferred, at least in part, from overpass schedules submitted by NJU.

This test does not include the TROPOMI system on the Sentinel-5P satellite, which has a detection limit far above the maximum of the release apparatus used in this study [38]. We inquired about tasking the Earth Surface Mineral Dust Source Investigation (EMIT) satellite, launched by the US National Aeronautics and Space Administration (NASA) in July 2022 [39], but the system was not available to participate in this test.

Participating analysis teams include private companies GHGSat [40], Kayrros [41], Maxar [42], and Orbio Earth [43], as well as the Land and Atmosphere Remote Sensing (LARS) group of university researchers from Universitat Politècnica de València (Luís Guanter, Javier Roger Juan, and Javier Gorroño Viñegla [6,24,44,45]) and Nanjing University (Fei Li, Huilin Chen, and Yongguang Zhang [46]). Each analysis team had the opportunity to submit estimates for all satellites tested,

with the exception of the GHGSat-C satellites, to which GHGSat had sole access. See the SI, Section S3 for a description of each team and its members, as well as a list of invited teams that declined to participate.

Materials

For the full test period, our experimental equipment was located near Casa Grande, Arizona, south of Phoenix, Arizona in the United States, with the release stacks located at [32.8218205°, -111.7857730°].

The methane source was two trailers of compressed natural gas, shown in Figure 1, which passed through a pressure regulation and reheating apparatus. The gas was then transmitted to the metering and release trailer via an 3" shipping hose at an exit pressure of roughly 150-200 psig (1.03-1.37 Mpa), passing through one of three possible Coriolis meters before release through one of two stacks, at a release height of either 7.3 or 3.0 m above ground level [47], shown in the SI, Figure 1. This testing setup approximately mimics an unlit flare or tank vent on an oil and gas production site or other facility.

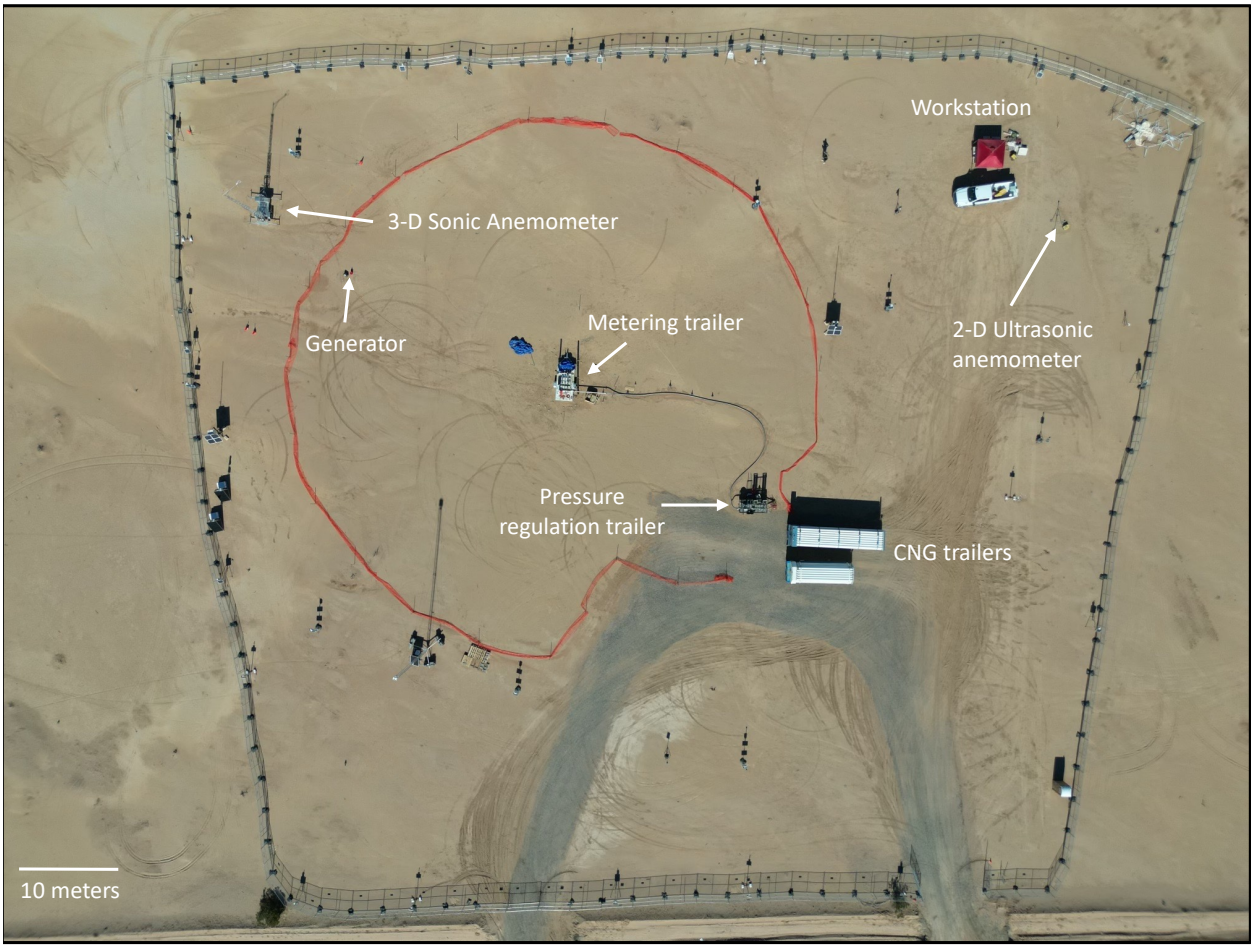


Figure 1. Aerial photograph of the site. Note that the workstation is ~60 m from the release apparatus and ~50m from the compressed natural gas (CNG) trailers. Reproduced with permission from El Abbadi et al. [47].

Achievable release rates for the three Coriolis meters, installed in pipes of different diameter, were 2 – 30 kilograms per hour (kg/h), 30 – 300 kg/h, and 300 – 2,000 kg/h for natural gas. See El Abbadi et al. 2023 for further detail [47].

Safety

All natural gas equipment fabrication, operation, and transportation was conducted by personnel affiliated with Rawhide Leasing, a gas services contractor. Stanford personnel contributed to assembly of some equipment, but did not operate natural gas release equipment or pass within our 100-foot (30.5 m) safety perimeter fence during active releases. The research workstation, from which Stanford researchers coordinated data collection and related field operations, was ~60 m away from any equipment through which natural gas flowed.

In addition, Stanford researchers periodically monitored plume dissipation in real time via a FLIR GasFinder 320 infrared camera and continuously paid attention to olfactory signals from the gas, which was odorized. The infrared camera showed clearly that the plume dissipated well before reaching any on-site personnel. Equipment design contributed to this intrinsic safety, because the emission source was elevated off the ground and gas often exited at a high vertical velocity, particularly at larger release volumes, accelerating natural methane lofting. When Stanford researchers detected gas smell during testing, they diligently checked infrared footage of the plume and/or ambient wind conditions to ensure safety of all personnel onsite.

Data logging

Stanford researchers collected data logs directly from the Coriolis gas flow meters, accounting for modest timestamp offsets as described in El Abbadi et al. 2023 [47].

Data collection procedures

All satellite-coincident releases began at least 15 minutes before the scheduled satellite overpass time, provided by participating teams.

Stanford personnel set all release levels remotely, using WiFi-enabled control software deployed on a laptop computer. For releases conducted on or before October 20th, Stanford personnel set a desired flow rate, with an automated control system adjusting valves in real-time to target that rate. After it became clear that this approach resulted in unnecessary flow rate variability, releases from October 21st on were conducted by setting the relevant valve to a desired level of openness, improving flow stability while slightly reducing the system's ability to target a specific release rate (although this system still represents a major improvement over the manual approach employed in Sherwin et al. 2023 [14]). Flow can fluctuate during the releases due to shifts in pressure, temperature, and simple turbulent flow through the system. All performed releases except four had flow variability with a 5-minute 95% confidence interval within ±10% of mean flow. On November 15, a GF5 satellite acquisition was rescheduled without notice to the Stanford team for a time that happened to be one minute after conclusion of a different satellite release, resulting in flow variability within ±20% of the 5-minute mean. Three additional releases exceeded a 5-minute flow variability 95% confidence interval of ±10%: the October 11th

GHGSat-C overpass (in which the instrument was not tasked), the October 17th WorldView-3 release of 0.042 [0.034, 0.050] t/h, and the November 30th PRISMA release of 0.98 [0.87, 1.08] t/h.

Interference from other sources was examined and found to be minimal. Over the course of the experiment, we tested the Carbon Mapper, GHGSat AV, Kairos Aerospace, MethaneAIR, and Scientific Aviation aerial methane sensing systems [47], all of which are more sensitive than any of the satellites tested. These aircraft, which also surveyed the nearby area during the process of data collection, found no detectable methane sources outside our test site. This strongly suggests that our test was free of interference from significant confounding methane sources. The only evidence of modest possible landfill interference comes Scientific Aviation, whose highly sensitive in situ measurement technology found modest and diffuse methane concentration enhancements over a nearby landfill, potentially impacting only one of the three days of testing, and only one of the seven measurements conducted on that day [47].

Flow rate uncertainty

Sources of uncertainty in measured methane flow rates include variability in actual natural gas flow rates (represented as the standard deviation of metered natural gas flow over a 5-minute period), rated meter uncertainty, and uncertainty in gas composition, which can vary even for a consistent supplier. We used highly precise Coriolis meters, which have manufacturer rated uncertainty of 0.25% of the flow rates used in this study [47]. Natural gas composition for the gas used in these releases, derived from measurement stations on the transmission pipeline that supplied the gas used in this test, ranged between 93.6% [93.3%, 93.9%] and 95.4% [94.7%, 96.1%] methane, described further in the SI, Section S.1.2 and in reference [47]. We propagate these sources of error into our metered values using code listed in data and code availability statement. See El Abbadi et al. 2023 for further discussion of sources of metering uncertainty and our method of determining flow rate uncertainty, as well as detailed gas composition data [47].

Following Sherwin et al. 2023, we use a 5-minute averaging period used to compute flow variability [14]. This is based on the fact that a plume traveling with a relatively slow average wind speed of 2 m/s, the minimum observed 5-minute average wind speed for any valid satellite measurement, would traverse 600 m within 5 minutes (300 seconds). By this distance, much of the originally emitted methane has likely dissipated into background concentrations, with the bulk of the methane enhancement detected by a satellite remaining closer to the release point.

Experimental design

This single-blind field trial employed a two-stage experimental design, modeled on Sherwin et al. 2023 [14]. This approach aims to disentangle the effect of wind speed uncertainty from other sources of methane quantification uncertainty, e.g. due to algorithmic differences.

Stanford personnel released metered quantities of methane from the test site via procedures described above and in reference [47]. The Stanford ground team and contract personnel operating equipment communicated no information to participating teams regarding metered flow rates, metered wind speed or direction, or the precise location of ground-based equipment. Teams were given a rough range of possible overall flow rates, from below 0.01 t/h to roughly 1.5 t/h. To facilitate efficient tasking of government satellites, LARS and NJU were informed in advance

that weekend releases in November would be cancelled and all such dates were excluded from single-blind analysis for those teams. In addition, participating teams were not informed of the details of the equipment or its configuration, or the diameter of the pipes and hoses involved, although teams were informed that the test would use compressed natural gas as the methane source.

After each team submitted final stage 1 estimates based on the above information, we proceeded to stage 2 estimates. In stage 2, Stanford provided 10 m wind speed and direction data from our on-site ultrasonic anemometer (shown in Figure 1) and teams were allowed to re-estimate emissions based on measured ground wind conditions rather than re-analysis products as in stage 1. All teams submitted stage 1 and stage 2 estimates, with the respective timelines described in the SI, Section S.2.10. Note that turnaround time for results in this study may not be representative of commercial or field performance.

All tested satellites detected methane

For the eight satellites given nonzero methane emissions, at least one analysis team correctly detected methane. The single HJ2 measurement, using the HJ2B satellite, was rescheduled without notice to a time in which Stanford was not releasing methane.

In total, the nine tested satellites conducted 82 overpasses. Six analysis teams analyzed data from between 1 – 8 satellites each, resulting in a total of 492 potential estimates. Stanford filtered many of these estimates from analysis before teams submitted results, for various reasons (e.g. due to release system malfunction or prior notice to teams tasking government satellites that there would be no weekend releases in November). In addition, most teams opted to submit estimates for only a subset of all available satellites. See the SI, Section S.1.3 for further discussion of data exclusion criteria.

Of the 139 estimates not filtered by Stanford, in five instances (3.6% of the total), teams filtered estimates using internal quality control criteria related to cloud cover, image clipping, or other factors that could compromise the ability to produce a valid methane estimate. GHGSat filtered three retrievals from the GHGSat-C satellite due to clouds (see Figure 8 and the SI, Section S4 for sky images and further discussion of clouds). LARS filtered two WorldView-3 retrievals due to cloud cover (November 22th) and inconsistent wind, and possible effects of human-made surface features (October 10th). As a result, a total of 134 estimates included valid methane detection estimates.

Of these 134 estimates, 80 (58%) were identified as either a true positive or true negative, correctly determining the presence or absence of methane, as shown in Figure 2. True positives represent 46 (34%) of total estimates with valid detection estimates, with 34 (25%) true negatives. Note that for Sentinel-2, we consider non-detection of an 0.005 t/hr release on November 28th to be a true negative, as this value is more than two orders of magnitude below existing estimates of the detection threshold of this system [14,34].

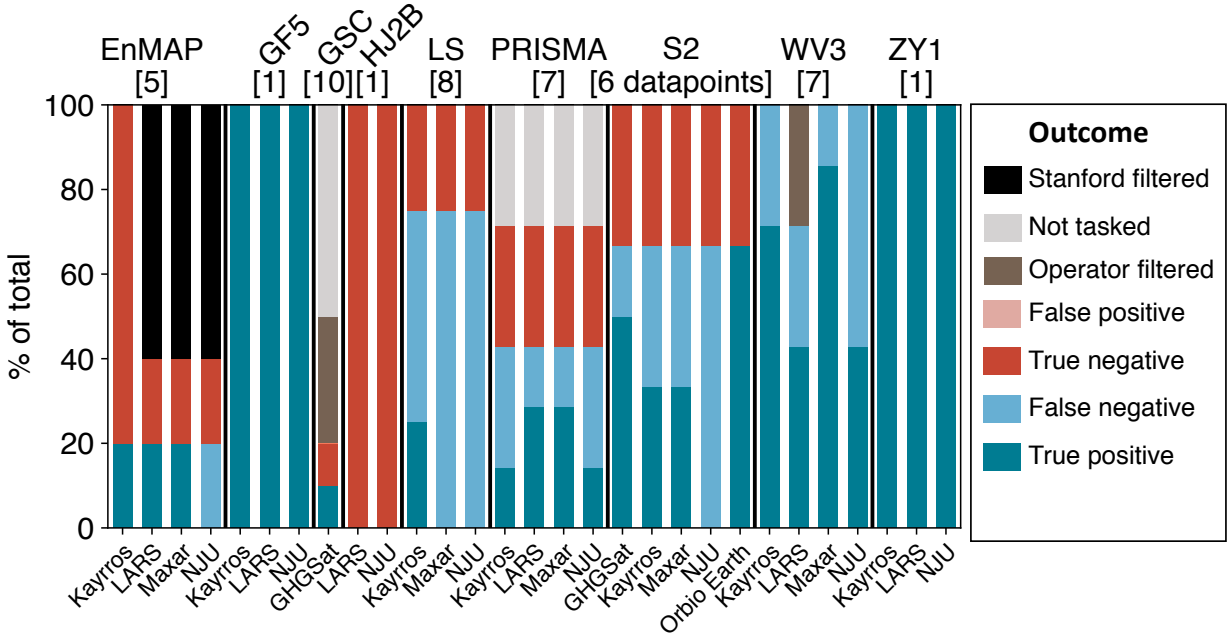


Figure 2. Detection performance by satellite and team. The total number of measurements per satellite is listed in brackets, excluding measurements filtered by Stanford across all teams. All teams analyzing data from the three Chinese satellites, Gaofen 5-02 Advanced Hyperspectral Imager (GF5), Ziyuan 1 (ZY1), and Huanjing 2B (HJ2B) all correctly classified all emissions. Detection performance varied substantially across the Sentinel-2 (S2) and LandSat 8/9 (LS) wide-area satellites. On several days, anticipated measurements from PRISMA and GHGSat-C (GSC) were not collected because the satellite was not tasked. In others, e.g. two WorldView-3 retrievals from LARS, no retrieval was conducted due to concerns over image clipping or excessive cloud cover. No teams submitted false positives, in which they reported the presence of methane when none was released.

Of the 41 false negatives (30%), most (25) are concentrated in the lower-sensitivity Sentinel-2 and LandSat 8/9 systems. There is substantial variability in false negative rates across teams. For example, Orbio Earth correctly classifying all valid Sentinel-2 releases. GHGSat missed only one Sentinel-2 release, and NJU detected none. This highlights that analysis of identical spectral data can produce very different results. As in Sherwin et al. 2023, there were no false positives, defined as incorrect reports of the presence of methane [14].

In several cases, a satellite was not tasked during an overpass for which the Stanford team conducted a release, either due to technical issues, scheduling issues, or miscommunications between the Stanford team and the operator. This occurred for five GHGSat overpasses and two PRISMA overpasses, resulting in a total of 13 Not Tasked estimates from participating teams for these two satellites, 9% of all estimates not filtered by Stanford.

First-time single-blind detections from Chinese and European satellites

This work includes the first-ever single-blind test of the Chinese Ziyuan 1 (ZY1), Gaofen 5 (GF5), and Huanjing 2B satellites (HJ2B), as well as the European EnMAP satellite. Previous studies have used a subset of these satellites to detect and quantify point-source emissions with estimated magnitudes as small as 0.5 t/h, but have not performed ground-truth testing [24].

Figure 3 shows masked methane plume images from ZY1, GF5, and EnMAP, over a standard optical satellite image background, for emissions of roughly 1 t/h. Masking refers to the process of spatially differentiating a methane emission from background noise. The HJ2B acquisition was rescheduled without prior notice to the Stanford team to a time at which no release took place, which all teams analyzing HJ2B data correctly identified as a non-emission. We present images from all teams analyzing satellite data from these measurements, including LARS, Kayrros, NJU, and Maxar. See the SI, Section S4 for masked and unmasked plume images for all satellites and teams.

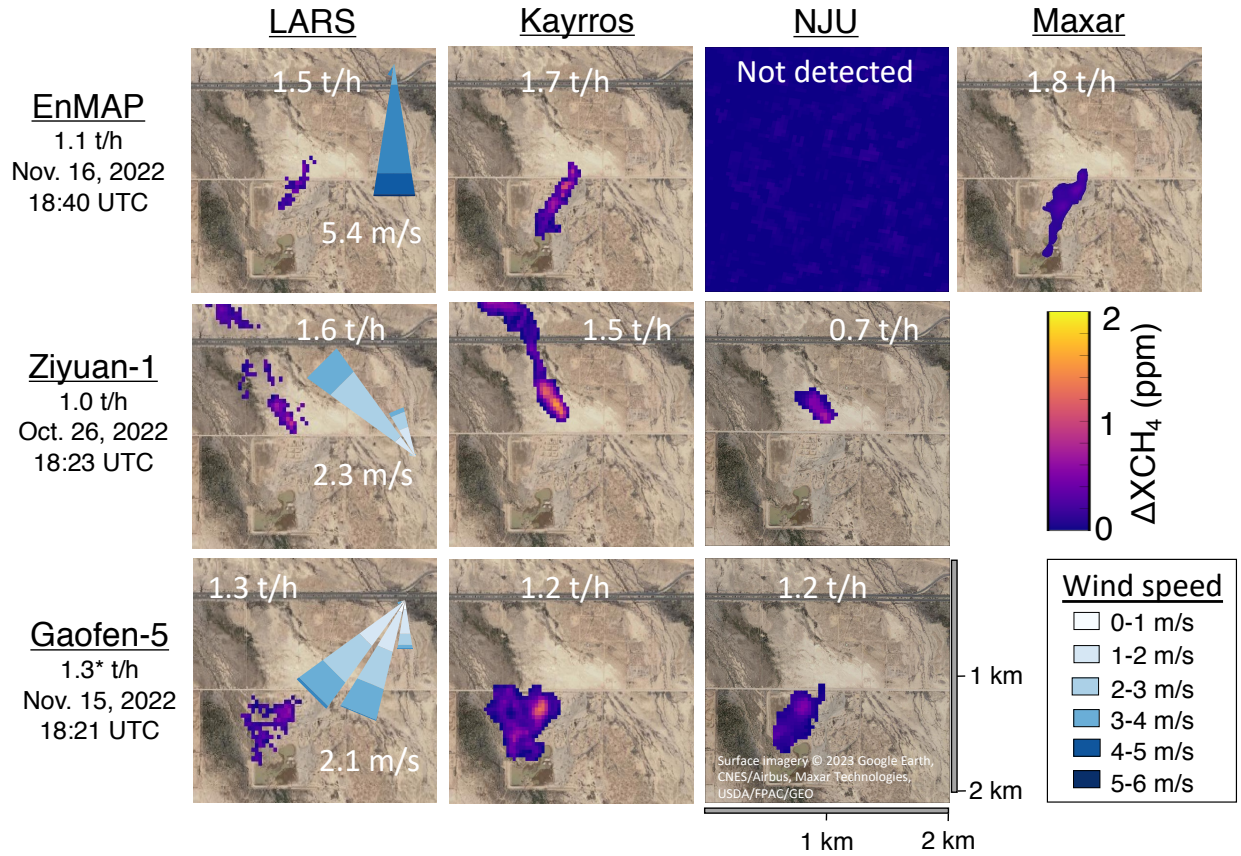


Figure 3. Visualization of detected emissions for the newly-tested European and Chinese satellites, using the release closest to 1 t/h in all cases. The true measured emission rate, as well as the timestamp are shown below the satellite name. Mean estimated volume from each team/satellite pair, as well as a 5-minute wind rose of measured 10-meter wind speed and the direction toward which the wind was blowing, are superimposed on the corresponding picture. The wind rose represents a histogram of one-second wind measurements in each direction, broken down by wind speed. Where an emission was not detected, we show the full unmasked retrieval field. Cloud-free surface imagery © 2023 Google Earth, CNES/Airbus, Maxar Technologies, USDA/FPAC/GEO.

Note that, as was observed in Sherwin et al. 2023, teams analyzing precisely the same spectral data can produce methane plume masks with very different shapes [14]. Each row represents a distinct satellite, while each column shows estimates from a distinct team. For example, the first row shows estimates for the November 16th EnMAP satellite measurement, for which four teams submitted estimates. Three of the four teams detected the emission. LARS, Kayrros, and Maxar all show masked plumes traveling in roughly the same direction, but the Kayrros and Maxar plumes are fairly contiguous, while the LARS plume is smaller and contains disjunct or tenuously-connected clusters of estimated methane enhancements. Overall, masks from LARS

are more conservative and less spatially contiguous than other teams. However, quantification estimates from LARS, Kayrros, and Maxar all have overlapping quantification intervals, demonstrating that the results are not statistically distinguishable across these three teams (NJU did not detect this EnMAP emission). Even with cases with large mean differences, e.g. October 26th estimates for ZY1, which range from 1.6 [1.2, 2.0] t/h for LARS to 0.7 [0.6, 0.9] t/h for NJU, the 95% confidence intervals overlap. These findings suggest that many factors influence quantification performance, even when working with identical spectral data, but large uncertainties make disentangling these differences a challenge. Further analysis of these algorithmic differences is beyond the scope of this work, as teams were not asked to provide algorithmic details, which are often proprietary. Further experimentation may enable analysis of general trends in advantages of one algorithm over another, but the order-100 number of datapoints here is insufficient to make such judgements.

Wind can vary substantially in speed and direction even on five-minute timescales relevant to methane quantification, as shown in wind roses inset in the left-most panel for each satellite in Figure 3. This variability clearly influences plume formation, with emissions with steadier wind directions and higher speed, such as the EnMAP and ZY1 measurements shown here (5.4 [3.7, 7.2] m/s and 2.3 [1.0, 3.7] m/s average wind speed, with a wind direction circular standard deviation of 16° and 11°, respectively), resulting in narrower plumes. The highlighted GF5 measurement has slower and more variable winds and a wider plume in all three retrievals (2.1 [0.3, 4.0] m/s, with a wind direction circular standard deviation of 18°).

Quantification performance approaches aircraft-level accuracy

Releases in this study covered a wide range of emission rates, as low as 0.0332 [0.0328, 0.0336] t/h, analogous to a medium-sized liquids unloading event at an oil and gas production site [48], and as high as 1.48 [1.43, 1.52] t/h, analogous to a medium-sized unlit flare [49]. For all detected emissions, mean estimates for all satellite-team combinations are between -56% and 456% of the metered value (Figure 4; see also SI, Section S4), with 55% of nonzero estimates falling within ±50% of the metered value. Excluding estimates from Maxar, which discovered after submitting results that its estimates were likely a factor of 2.3 too high due to a misinterpretation of a deprecated spectral absorption library, this fraction rises to 63% [50]. The latter overall performance approaches that of the satellites and teams tested in Sherwin et al. 2023, in which 75% of estimates fell within ±50% of the metered value, demonstrating a relative error profile similar to that observed in aircraft-based methane remote sensing technologies [14]. Direct comparison with the results in Sherwin et al. 2023 is complicated by the fact that releases in this study focused on smaller emissions, with a maximum of roughly 1.5 t/h instead of 7.2 t/h. Aircraft-based methane remote sensing technologies tested in El Abbadi et al. tend to have modestly better quantification performance in percentage terms, with 68-80% of estimates from Carbon Mapper, GHGSat, Kairos Aerospace, and MethaneAIR falling within ±50% of the metered value [47], a substantial improvement over prior tests of the same technologies [18,51].

See the SI, Section S4 for error summary statistics by satellite and team. Error bars in metered values along the x-axis are generally too small to be visible, with the notable exception of the GF5 measurement, which was rescheduled without notice to a time that happened to be one minute after releases had concluded for a different satellite.

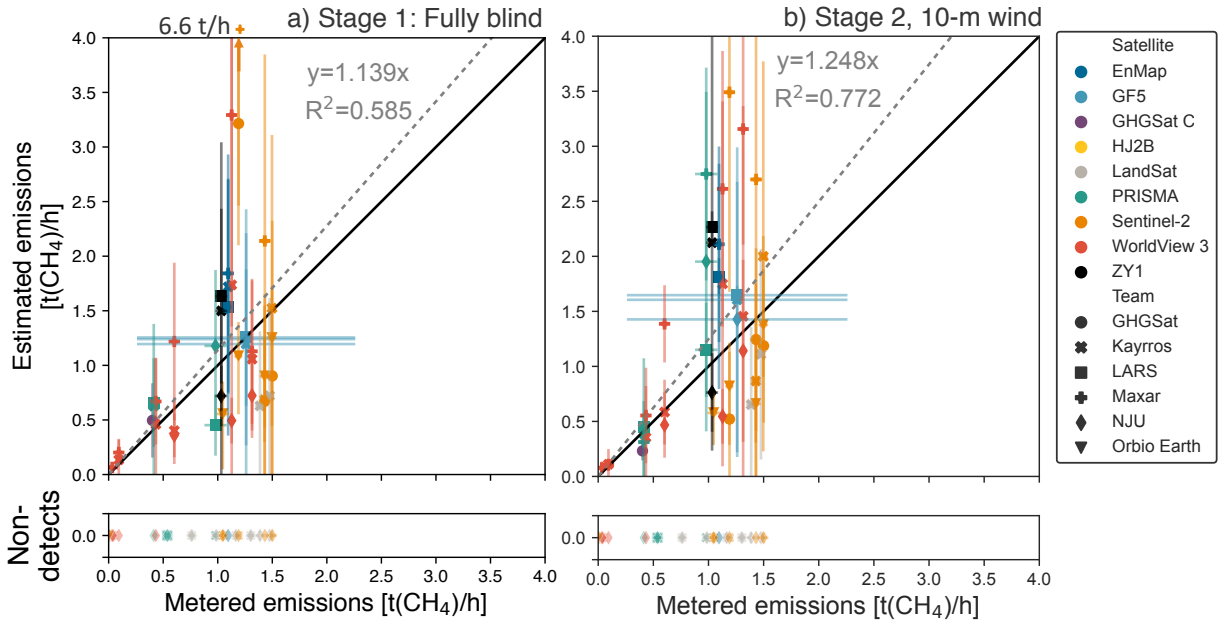


Figure 4. Methane quantification performance by satellite and team. Metered emissions compared with single-blind estimates for each overpass with successfully reported data, with 95% X and Y confidence intervals. a) Fully blind stage 1 results using modeled wind speed estimates. Note one Sentinel-2 estimate exceeds the y-axis limit at 6.6 t(CH_4)/h. b) Stage 2 results using on-site 10 m wind speed and direction measurements. LARS WorldView-3 quantification estimates are excluded from the main analysis, as stage 1 estimates were submitted after wind data had been unblinded to a member of the LARS team not involved in analyzing WorldView-3 data, while corresponding stage 2 estimates were submitted after release volumes were unblinded. Note that Maxar submitted PRISMA estimates for stage 2 only. The grey dashed lines represent an ordinary least squares fit with the intercept fixed at zero, with slope and uncentered R^2 displayed. Maxar has since determined that its estimates were likely artificially high, potentially introducing upward bias into aggregate statistics [50]. The black solid lines denote exact 1:1 agreement. See the SI, Section S4 for satellite- and team-specific results.

In stage 2 of the test, teams produced updated results using measured 10 m wind data from an on-site three-dimensional ultrasonic anemometer, though still blind to released volumes. Applying an ordinary least squares linear fit to all quantified emissions, with the intercept set to zero, we see a modest increase in slope, rising from 1.139 [0.832, 1.446] in stage 1 to 1.248 [1.037, 1.459] in stage 2 (Figure 4).

Interpretation of these results is complicated by the fact that the Maxar team discovered after submitting blinded results that the spectral library underlying their estimates contained an error that likely artificially inflated their estimates by a factor of 2.3, discussed in detail in a white paper produced by Maxar personnel [50]. This is consistent with the Maxar-specific parity chart in the SI, Section S4, alongside other satellite- and team-specific results, which shows a regression best fit line of 2.334 [1.030, 3.638] and an uncentered R^2 of 0.96, indicating a close linear fit. Excluding Maxar results, the Stage 1 slope for all remaining teams falls to 0.897 [0.716, 1.078], with a Stage 2 slope of 1.010 [0.841, 1.180], almost perfect average agreement with metered values. These slopes are 21% and 19% below the respective estimates in which Maxar values were included.

Note that LARS WorldView-3 quantification estimates are excluded from the main analysis, as stage 1 estimates were submitted after wind data had been unblinded to a member of the LARS team not involved in analyzing WorldView-3 data, while corresponding stage 2 estimates were submitted after release volumes were unblinded. Although the Stanford team believes all LARS quantification estimates for WorldView-3 were submitted without leveraging unblinded data, we must exclude them from the main analysis. This does not affect the integrity of detection estimates, as only wind measurements were unblinded when these were first submitted. See the SI, Section S4 for LARS WorldView-3 quantification results.

After incorporating on-site wind measurements, the uncentered R^2 increases from 0.585 to 0.772, a substantial improvement in goodness-of-fit. Excluding Maxar results, these numbers rise to 0.768 and 0.826, respectively. The linear fit presented here treats all estimated emission rates from all team as independent datapoints. Note that uncentered R^2 values from such a linear fit, with a zero intercept, have a different interpretation than R^2 values from nonzero-intercept regressions and should not be compared directly. See Sherwin et al. 2023, SI Section S5 for further explanation of the reasons for an ordinary least squares fit with the intercept fixed to zero [14]. This improved average linear fit with in situ wind does not necessarily translate to lower error for each individual satellite, as shown in the SI, Section S4, alongside additional regression results.

Confidence intervals submitted by teams appear to be modestly overconfident. For Stage 1 estimates, the metered value is within the provided 95% confidence interval only 70% of the time, somewhat below the expected value of 95% for perfectly-calibrated 95% confidence intervals. For Stage 2, this fraction falls to 52%, although mean error improves. Note that these values combine results from multiple satellites and teams, and thus represent an overall sense of the performance of satellite-based methane sensing systems as a technology class. Additional data collection is needed to characterize the performance of each individual satellite in detail.

Figure 5 shows Stage 1 fully blinded results, the same underlying data as in Figure 4, for each individual team. Team-specific parity lines tend to fall near the ideal 1:1 level, with Orbio Earth and NJU exhibiting modest low bias parity slopes of 0.74. Note that Maxar's parity slope of 2.3 matches almost exactly with the factor of 2.3 they believe was error introduced into their system through misinterpretation of a deprecated spectral library [50]. The bulk of false negatives were from the relatively low-resolution Sentinel-2 and LandSat 8/9 satellites. However, Orbio Earth successfully detected all Sentinel-2 releases above 0.010 t/h, highlighting algorithmic variation across teams analyzing the same spectral data.

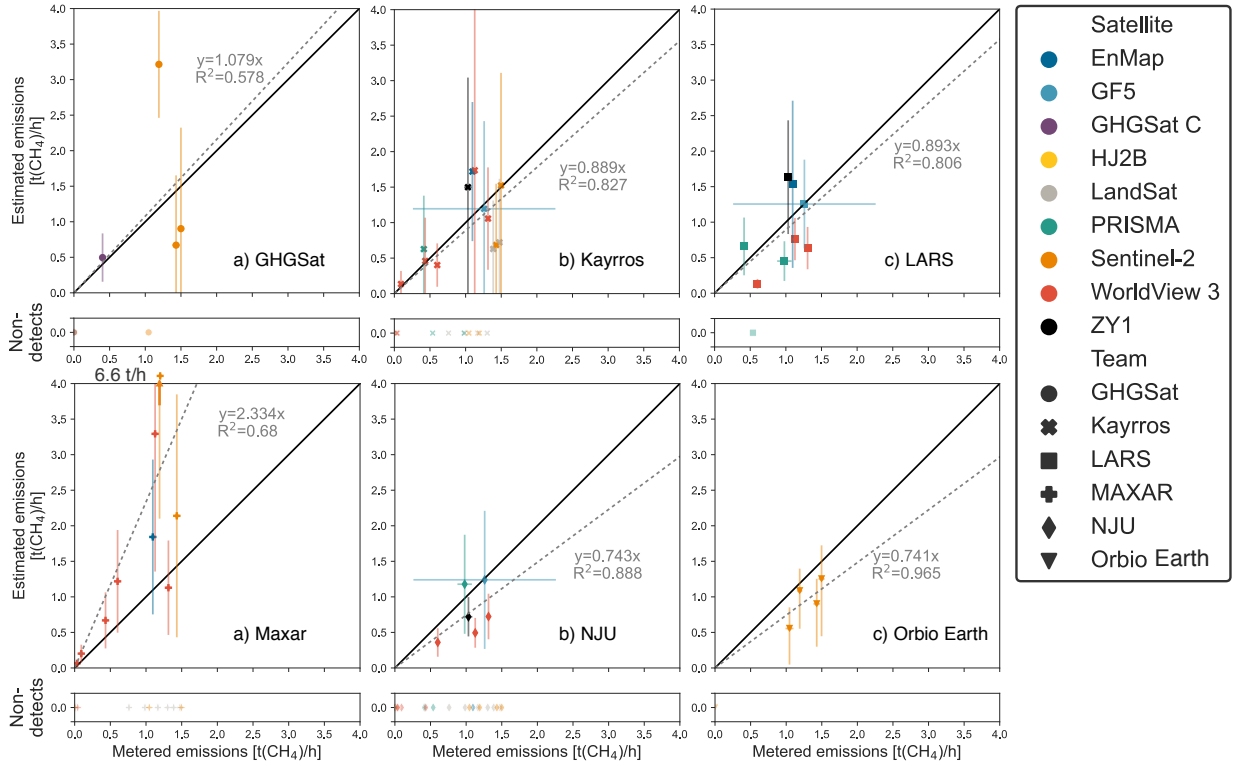


Figure 5. Parity charts by team, for fully blinded Stage 1 estimates only. Metered emissions compared with single-blind estimates for each overpass with successfully reported data, with 95% X and Y confidence intervals. Note one Maxar Sentinel-2 estimate exceeds the y-axis limit at 6.6 t(CH_4)/h. LARS stage 1 WorldView-3 quantification estimates are excluded from the main analysis, as they were submitted after wind data had been unblinded to a member of the LARS team not involved in analyzing WorldView-3 data. The grey dashed lines represent an ordinary least squares fit with the intercept fixed at zero, with slope and uncentered R^2 displayed. Maxar has since determined that its estimates were likely artificially high, potentially introducing upward bias into aggregate statistics [50]. The black solid lines denote exact 1:1 agreement. See the SI, Section S4 for Stage 1 and Stage 2 satellite- and team-specific results.

Qualitatively assessing detection performance in the field

The smallest emission detected by each team gives a sense of the minimum detection capabilities of each instrument, at least in a desert environment with a known release location. The smallest emission detected was 0.0332 [0.0328, 0.0336] t/h, identified by Maxar using WorldView-3, shown in Figure 6. Kayrros also detected an emission below 0.1 t/h using WorldView-3.

Orbio Earth, Maxar, and GHGSat all detected a 1.19 [1.15, 1.23] t/h emission using Sentinel-2, with errors ranging from -8% to +170%. Orbio Earth detected a 1.05 [0.99, 1.10] t/h emission to within ±47%. These emissions are 15-25% below than the smallest emission detected using Sentinel-2 in any previous satellite controlled methane release test [14].

The smallest detected emissions for the remaining satellites are 1.10 [1.06, 1.13] t/h for EnMAP, 1.26 [0.26, 2.26] t/h for GF5, 1.39 [1.34, 1.43] t/h for LandSat 8/9, 0.414 [0.410, 0.417] t/h for PRISMA, and 1.03 [0.98, 1.09] t/h for ZY1. GHGSat correctly detected and quantified the only

nonzero release for which GHGSat-C collected data and passed quality control, which was 0.401 [0.399, 0.404] t/h, roughly double the smallest release GHGSat quantified using the same satellite system in [14]. HJ2B was not tasked during any active releases, meaning that future testing is needed to assess its detection capabilities.

In practical applications for global remote sensing, teams have only limited information about the location of possible sources and their likelihood of emitting at visible levels. As a result, it is possible that the known-location experimental design applied here may have allowed teams to artificially boost detection sensitivity to levels that would be difficult to achieve in general practice.

To qualitatively assess this possibility, all teams were required to submit methane retrieval field images for all submitted estimates, including both detections and non-detections. In all cases, teams submitted full-scene retrieval fields in a 2x2 km box around the release location. For detected emissions, teams also submitted masked plume images, overlaying the estimated methane plume above an optical image of the background location. See the SI, Section S4 for all such images.

We highlight selected images in Figure 6 to showcase issues related to spectral artifacts, e.g. apparent methane enhancements due to water bodies, clouds, or roads, that we were not able to quantitatively address in this study. The GHGSat images, shown at a contrast-enhancing narrower color scale of 0-0.2 ppm instead of this study's standard 2 ppm, show that for the November 8th retrieval of the 0.401 [0.399, 0.404] t/h release, there are pixel clusters with enhancements of comparable magnitude outside of the release area. However, these enhancements are concentrated along ground features such as a water body southwest of the site and a highway north of the site, confirmed in Google Maps imagery and WorldView-3 optical images in the SI, Section S4. As a result, automated or manual intercomparison of the spatial overlap of apparent methane enhancements and ground features visible in optical imagery could plausibly help differentiate between such signal artifacts and true emissions. In some cases, it may be possible to use measurements in which there is no evidence of a methane emission, e.g. the November 16th measurement (in which GHGSat correctly determined the absence of methane in a single-blind manner), to gain additional information into ambiguous cases. Artifacts such as the water feature may consistently appear across retrievals, which could suggest that they are not true methane enhancements. Furthermore, GHGSat flagged the water body in both retrievals as a potential artifact, indicating that it would likely have been possible to correctly identify only the true methane emission in the November 8th scene even without a reference image with no methane.

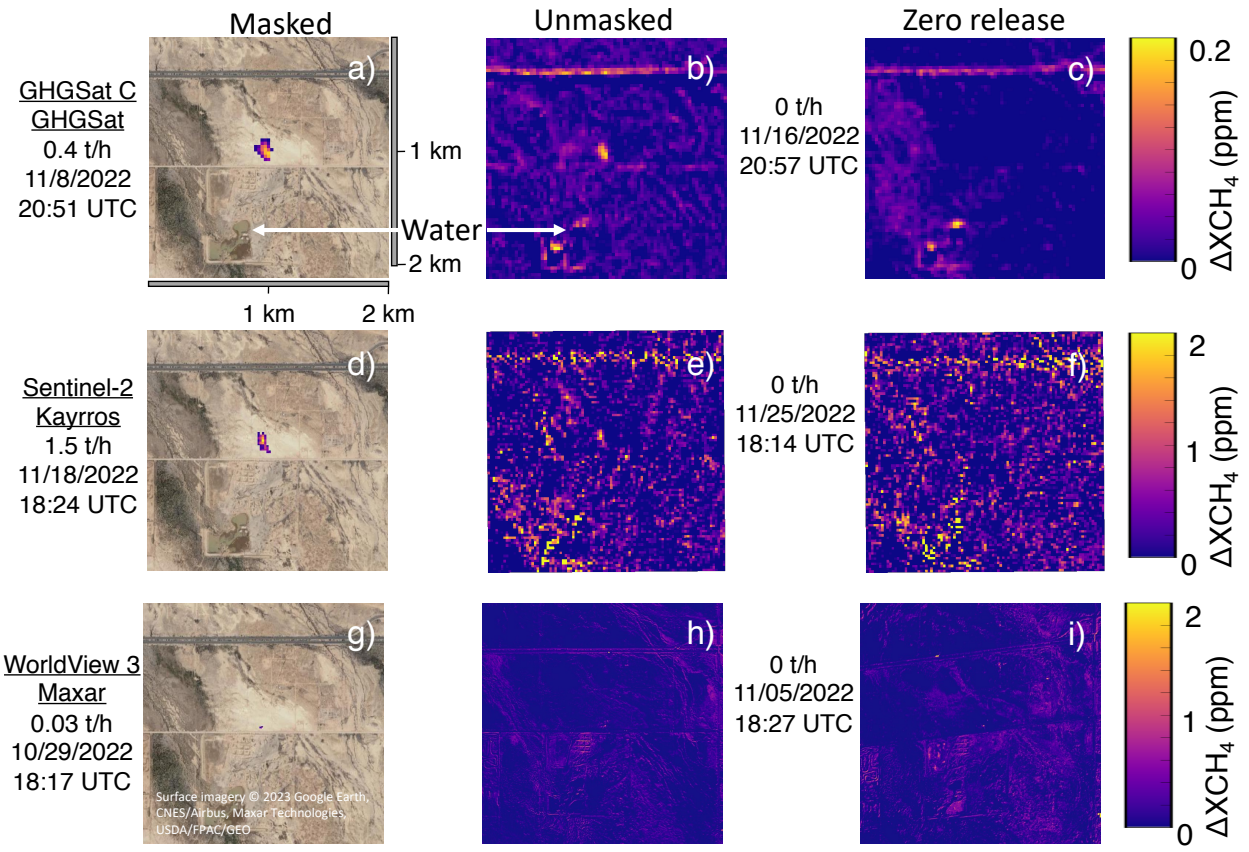


Figure 6. Masked and unmasked retrievals for selected emissions. In each case, the unmasked retrieval in the middle column appears to contain artifacts of similar intensity and shape to the masked emission. However, the emission may be more distinguishable from artifacts after intercomparison with ground features revealed through optical imagery, e.g. the water body southwest of the release site, and intercomparison with a reference day with zero emissions, as in the right column. Note that the GHGSat retrievals use a higher-contrast scale of 0-0.2 ppm. For See the SI, Section S4 for GHGSat images using the standard 0-2 ppm scale applied for most retrieval images in this study. Cloud-free surface imagery © 2023 Google Earth, CNES/Airbus, Maxar Technologies, USDA/FPAC/GEO.

Sentinel-2 imagery is significantly noisier than most other tested satellites. The November 18th Kayrros retrieval in Figure 6 shows noticeable enhancements, comparable in intensity to the true emission, along the water feature and the highway, as well as northwest of the release site. In such a noise environment, knowledge of the emission location and access to images known not to contain emissions, such as panel f) may assist in correct identification of the true emission. See the SI, Section S4 for all masked and unmasked retrieval images from all satellites.

Maxar correctly detected emissions as small as 0.0332 [0.0328, 0.0336] t/h using their WorldView-3 satellite on October 29th. Interestingly, their retrieval algorithm does not appear to introduce high-concentration artifacts over the water body (although that is not the case for all teams analyzing WorldView-3 data, as shown in the SI, Section S4). The full retrieval image for the October 29th retrieval shows concentration enhancement artifacts of comparable magnitude to the correctly-detected emission at several points in the image. However, these artifacts are largely conformal with surface features visible in optical imagery.

In addition to the known location, Maxar tasked its WorldView-3 satellite without notice to the Stanford team on November 24th, a holiday in the United States. These data were shared with all teams, but Maxar did not submit an unmasked image for the November 24th retrieval, although they did for the zero-emission November 5th retrieval, shown in panel i). As a result, Maxar and all other participating teams were able to compare satellite data from active testing days with data that they knew very likely did not contain methane enhancements. As a result, these teams had information in addition to the known release location that would not necessarily be available in the field. As a result, we cannot definitively conclude from this study whether Maxar or other teams would successfully identify emissions as small as 0.0332 [0.0328, 0.0336] t/h in the field. Future testing, likely with multiple potential source locations, is needed to more rigorously assess field-realistic detection limits of all satellites tested in this study.

The role of clouds

Because water vapor is highly absorptive in the methane-active infrared frequencies targeted by all nine methane-sensing satellites tested in this study, cloud cover can impede or prevent valid satellite-based methane measurements. Although our Arizona test site was selected in part due to its arid, relatively low-cloud climate, periodic cloud cover occurred to varying degrees throughout the testing period.

The treatment of clouds varied across teams, with some filtering images due to cloud cover more aggressively than others. LARS filtered the November 22nd WorldView-3 retrieval, shown in Figure 7a, noting “the image is cloudy but we see some enhancement.” Kayrros and Maxar correctly detected the 0.433 [0.430, 0.436] t/h emission for the same measurement, while NJU reported a non-detection.

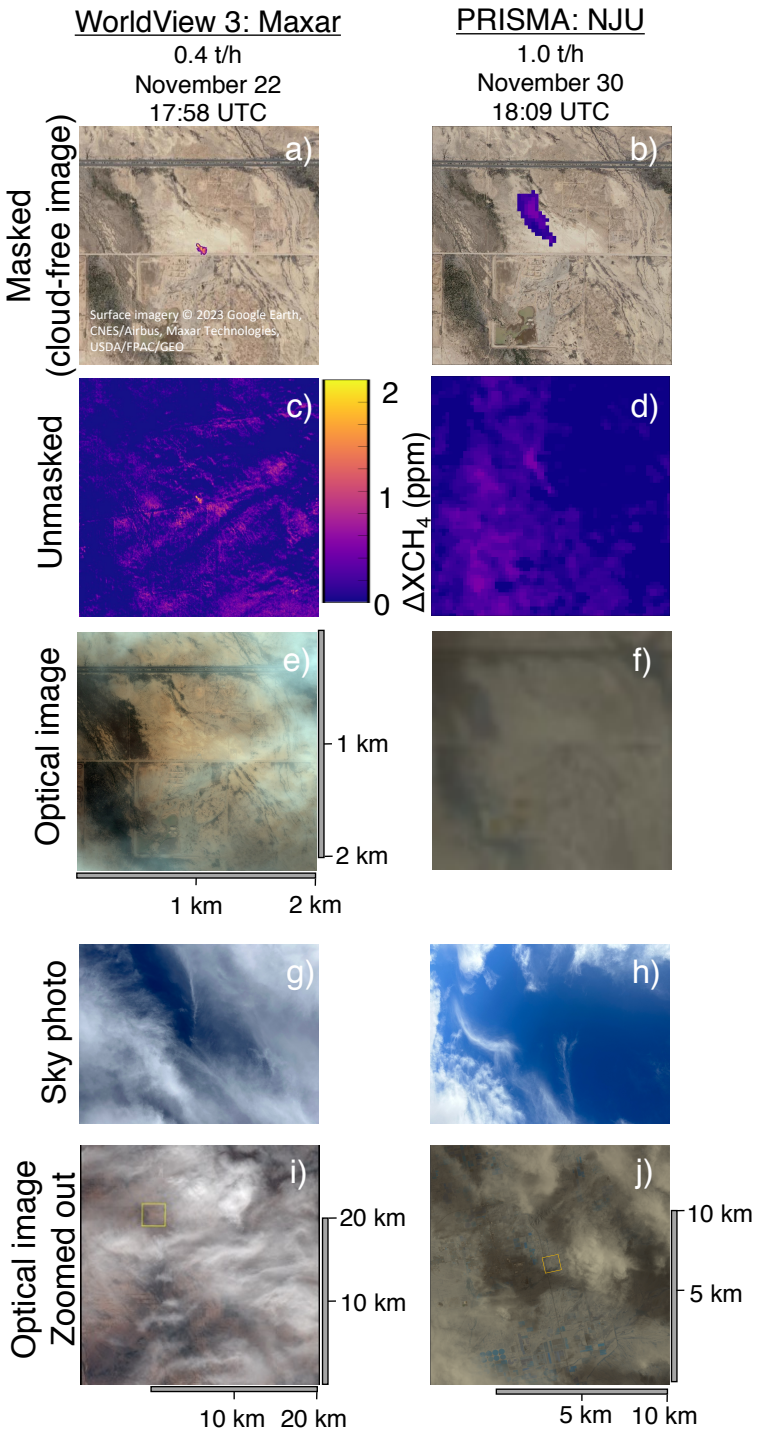


Figure 7. Cloudy days with successful methane detections. a) and b) show masked methane emissions from WorldView-3 and PRISMA above a cloud-free standard background © 2023 Google Earth, CNES/Airbus, Maxar Technologies, USDA/FPAC/GEO. c) and d) show corresponding unmasked images. e) and f) show optical images of the same 2x2 km scene collected by each satellite. g) and h) show photographs of the sky, taken by Stanford researchers on smartphones at the time of each overpass. i) and j) show zoomed-out versions of the optical images shown in e) and f), with different length scales than the other panels.

This highlights that accurately interpreting the results of field measurements from each of these teams requires an understanding of both detection performance and data filtering processes as a function of cloud cover.

Stanford researchers took photographs of the sky coincident with most satellite overpasses to document cloud cover, shown in full in the SI, Section S4. The photograph for the November 22nd WorldView-3 overpass, Figure 7g, appears to show significant thick cloud cover. However, analysis of optical WorldView-3 imagery from this measurement, Figure 7e, shows that the area immediately above the test site was relatively cloud-free even though the broader area was experiencing significant cloud cover, shown in Figure 7i.

Analysis of the November 30th PRISMA measurement, shown in the second column of Figure 7 adds further nuance to the question of cloud cover. The sky photograph in Figure 7h shows the presence of thin clouds. However, the optical image collected by PRISMA in Figure 7f shows no clouds within the 2x2 km square surrounding the release site. The photographed clouds are only visible in the larger, 14x14 km image in Figure 7j, which demonstrates that clouds are too far away from the release site to interfere with the 0.98 [0.88, 1.08] t/h methane plume, which was correctly detected by LARS, NJU, and Maxar.

These two cases demonstrate that only limited information regarding cloud cover can be determined from single-frame sky photographs taken from the ground. This is particularly true without clear orientation information, which is not available for the smartphone-based photographs used in this study.

Figure 8 shows sky photographs of all dates with valid or operator-filtered GHGSat measurements. Both days with valid measurements, one true positive and one true negative, were essentially cloudless, as shown in Figure 8d-e. In addition, GHGsat filtered three retrievals due to clouds. Of the three days filtered due to cloud cover, one was fully overcast (Figure 8c), while two had thin clouds, shown in Figure 8a-b, also noted in the GHGSat report for those days. As demonstrated above, it is difficult to determine from these sky photographs alone where these clouds were in relation to the release site.

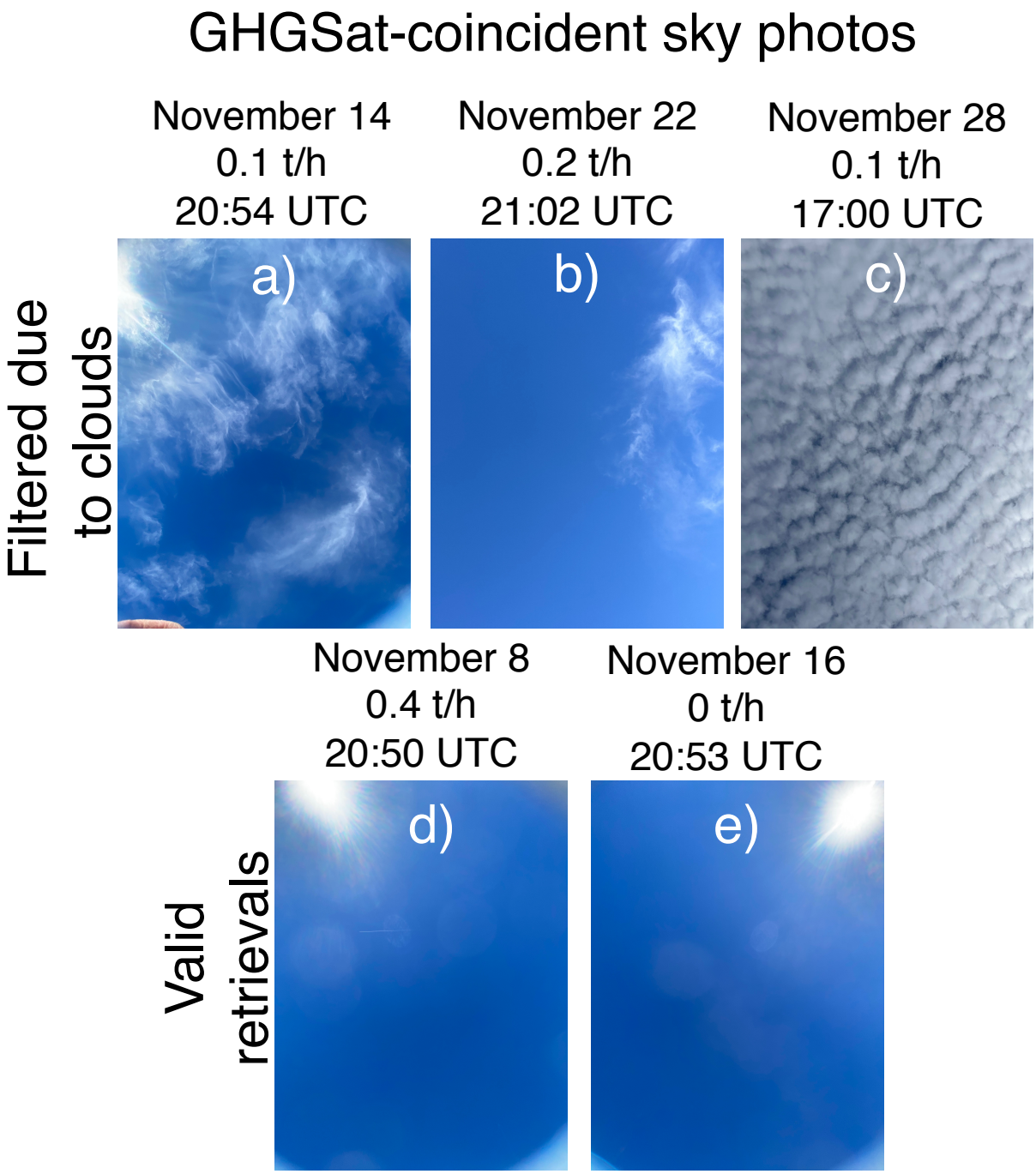


Figure 8. Ground-perspective sky photos for GHGSat-C measurements. a-c) correspond to measurements filtered due to cloud cover. d) and e) correspond to valid retrievals, including one true positive detection and one true negative non-detection. GHGSat-C satellites do not collect optical imagery, making it difficult to directly compare ground-perspective photographs with satellite-perspective optical imagery.

GHGSat did not submit unmasked retrieval images for operator-filtered measurements (these images were requested from all teams, but were not required as a condition of participation in this test). Furthermore, GHGSat does not collect optical imagery in visible frequencies, so none

could be submitted. As a result, we can draw only limited conclusions about the role of cloud cover in GHGSat's ability to conduct valid measurements with the GHGSat-C satellite model.

Future satellite-focused controlled methane release tests should further investigate the role of cloud cover. This should include conducting testing in cloudier locations. In addition, sky photographs should be replaced by or supplemented with passively-collected time series of panoramic, georeferenced sky time series, e.g. using a fisheye camera (e.g., as used in solar forecasting systems [52]). This, together with optical images collected by satellites (when available), will allow a more systematic evaluation of the capabilities of the tested systems as a function of cloud cover. Such analysis should include assessment of the effect of clouds on detection sensitivity and quantification performance, as well as their role in preventing collection of valid measurements. These cloud-informed performance findings will be indispensable in regional analysis of satellite-based methane remote sensing data, including its incorporation into emissions inventories.

Discussion

This work demonstrates that all tested satellites are capable of detecting and quantifying methane emissions. All eight satellites given the opportunity detected methane emissions, with overall quantification accuracy similar, in percent terms, to aircraft-based methane sensing systems. This highlights the large suite of satellite-based tools available to detect and quantify methane point sources across the globe.

Detection limits appear to improve with smaller swath width and pixel size. Global-coverage satellites such as LandSat 8/9 and Sentinel-2, with swaths of 185 and 290 km, respectively, have higher detection limits. Our results are consistent with Gorroño et al., whose simulation-based approach suggests that such instruments have a best-case minimum detection limit of roughly 1 t/h. Targeted satellites with swaths of 30-60 km, including EnMAP, GF5, PRISMA, and ZY1 [21,23,29,30], all reliably saw emissions of ~1 t/h. Of these, only PRISMA was given smaller emissions, with three of four teams correctly detecting 0.413 [0.410, 0.417] t/h, the smallest emission given to PRISMA. GHGSat correctly detected 0.401 [0.399, 0.403] t/h, with quantification accuracy within ±20%, using their GHGSat-C-series satellite, with a swath width of 12 km. Estimates for smaller emission sizes were filtered due to clouds, but in previous testing GHGSat successfully detected an 0.197 [0.187, 0.208] t/h emission and quantified it with similar accuracy, suggesting that the system may be capable of seeing emissions even smaller than 200 kg/h.

Maxar successfully detected emissions as low as 0.0332 [0.0328, 0.0336] t/h using the WorldView-3 satellite, with swath width 13.1 km. Two teams successfully detected emissions below 0.1 t/h using WorldView-3, while two teams applied more conservative criteria and detected only emissions above 0.5 t/h.

In the high-emission New Mexico Permian basin oil and natural gas system, using 2019 emission levels, a comprehensive measurement campaign with a constellation of satellites detecting all emissions above 1 t/h would find 20% of emissions from oil and gas well sites, rising to 62% for a satellite detecting emissions above 0.2 t/h, and 83% above 0.03 t/h [14]. These fractions are

upper-bound estimates both because near-real-time comprehensive coverage would be challenging for satellite systems and because the underlying emission size distribution estimate may be conservative for emissions below roughly 50 kg/hr [14]. In lower-emitting basins such as the Denver-Julesburg, each of these systems would see a much smaller fraction of total emissions, highlighting the need for a variety of technology approaches, tailored to regional system characteristics [14].

Note that the detection results presented in this paper reflect system performance with a known source location under favorable desert climate conditions. These results may not translate to field performance in different environments and with less foreknowledge about the location of possible sources.

Unmasked methane retrieval fields, submitted by all teams, suggest that achievable detection limits may be higher in practice for some satellites. In some cases, these images contain background artifacts with estimated methane enhancements comparable in magnitude and qualitatively similar in shape to the detected methane plumes. However, in many of these retrieval fields, particularly for larger emissions, the true methane plume is unambiguous. It is noteworthy that some teams correctly flagged likely background artifacts in blinded submissions, but such georeferenced quality flagging was not required of all participating teams, although doing so may be advisable in future tests.

The role of surface features, such as water bodies, in creating apparent methane enhancements should be explored further. For example, the retrieval field for the 0.401 [0.399, 0.403] t/h GHGSat measurement shows an apparent methane enhancement over a water body that is similar in magnitude to the detected plume. However, if this is a known characteristic of the algorithm, then such artifacts could be automatically or manually filtered out, leaving only the clear methane plume at the release site. The water body appears as a flagged region in all data reported by GHGSat, indicating that their system is capable of identifying potential confounding factors such as water bodies and differentiating any resulting artifacts from true methane emissions.

Clouds add several levels of complexity to satellite-based methane sensing. The water vapor in clouds interferes with the frequencies all tested satellites use to identify methane enhancements. Heavy cloud cover essentially prevents valid satellite-based methane sensing. This test demonstrates that it is possible in some circumstances to detect and quantify methane emissions even in the presence of nearby patchy or thin clouds. However, it is unclear in some cases whether these detected emissions would have been distinguishable from background noise, e.g. artifacts caused by clouds or highly reflective/absorptive surface features, in the absence of a known source location and reasonable anticipation of the presence of an emission due to an ongoing test.

Different teams employed different filtering criteria. GHGSat excluded all GHGSat-C measurements with cloud cover. Maxar and Kayrros used WorldView-3 to successfully detected a 0.433 [0.430, 0.436] t/h emission on a cloudy day on November 22, while LARS filtered the measurement due to clouds and NJU reported a non-detection.

Future testing should characterize the cloud conditions under which valid point-source methane measurements can and cannot be conducted with each satellite-based system. In addition, future work should characterize the effect of partial cloud cover on detection and quantification performance. Understanding these two factors will be critical when interpreting the results of large-scale satellite-based methane measurement campaigns, which will inevitably encounter interference from clouds. Cloud cover varies widely across oil and gas-producing regions, with limited clouds in arid areas such as the Permian basin in Texas and New Mexico, and significant cloud cover in more temperate producing regions such as the Appalachian basin in the eastern United States and the Williston basin in the midwestern United States [53].

Wind speed remains a major driver of uncertainty in satellite-based methane point source quantification. Moving from wind reanalysis data to in situ wind measurements substantially reduces scatter around the line of best fit, as was also the case in other work from the same group [14]. In addition, in situ wind measurements show considerable temporal variability in wind speed and direction over the multi-minute timescales most relevant to plume formation.

In the field, winds are generally only available from reanalysis data, which capture temporal, spatial, and directional variability with much lower fidelity than on-the-ground wind measurements. Advances in the spatial and temporal fidelity of wind reanalysis products, as well as their accuracy, could help improve methane remote sensing. In addition, it may be possible to entirely eliminate reliance on wind speed, e.g. by inferring emission rate information solely from plume shapes as in reference [54].

The findings presented here demonstrate that at least eight distinct satellite systems from three continents are capable of detecting methane point sources of 1.5 t/h or less. Furthermore, this study more systematically probes lower detection limits of these systems, two teams detecting emissions below 0.1 t/h, the first time to our knowledge that such performance has been demonstrated in a single-blind test of satellite-based methane sensing systems. The NASA Earth Surface Mineral Dust Source Investigation (EMIT), which launched shortly before our testing began [39], has already reported detecting methane emissions in the field and should be tested, along with the HJ2 system, in future single-blind controlled methane releases.

In coming years, the Carbon Mapper and MethaneSAT systems will launch, alongside additional satellites in some of the constellations tested here [13]. The airplane-mounted precursors to both the Carbon Mapper and MethaneSAT systems have conducted substantial single-blind testing of their point-source detection and quantification capabilities [47,51,55], but the satellites will require additional tests.

The tools exist for multi-lateral global methane monitoring efforts, with satellites from multiple countries and continents able to independently assess emissions from regions of interest. The single-blind test conducted here is a step toward ensuring that stakeholders across the world have confidence in the methane emissions these satellite systems find at oil and gas facilities, landfills, coal mines, and other emitting infrastructure. This will help satellites achieve their potential to not only detect and quantify large methane emissions, but to inspire meaningful action to reduce emissions of this powerful greenhouse gas.

Data and code availability

All data and code required to reproduce the figures and analysis in this paper will be made publicly available on GitHub. Underlying spectral imagery will not be made directly available through this study, but for many satellites tested in this study these spectral data can be acquired either for free or for purchase for via platforms discussed in the SI, Section S2.

1. Abbreviations

ADED	Advancing Development of Emissions Detection
ASI	Italian Space Agency
CNG	Compressed Natural Gas
EMIT	Earth Surface Mineral Dust Source Investigation
EnMAP	Environmental Mapping and Analysis Program
GF5	Gaofen 5
GSC	GHGSat-C (satellite)
HJ2	Huanjing 2
IME	Integrated Mass Enhancement
kg/h	Kilograms per hour
LARS	Land and Atmosphere Remote Sensing
LS	LandSat
METEC	Methane Emissions Technology Evaluation Center
NASA	National Aeronautics and Space Administration
NJU	Nanjing University
NOAA	National Oceanographic and Atmospheric Administration
OHB	Orbitale Hochtechnologie Bremen
PRISMA	PRecursore IperSpettrale della Missione Applicativa
UPV	Universitat Politècnica de València
USGS	United States Geological Survey
SRON	Stichting Ruimte Onderzoek Nederland
SWIR	Short-wave Infrared
TROPOMI	TROPOspheric Monitoring Instrument
t/h	Metric tons per hour
VNIR	Visible to Near Infrared
WAV-P	Wide-Angle Fabry-Perot
WV3	WorldView-3
ZY1	Ziyuan 1

2. Acknowledgments

We acknowledge C. de Franchis, C. Giron, and A. Groshenry of Kayrros; and Z. Mouton, W. Kingwill, and R. Huppertz from Orbio Earth for their participation in this test. A. Esparza, L. Clark-Squire, J.F. Gauthier, M. Girard, D. Jervis, R. Mattson, J. McKeever, A. Newhook, and M. Turenne of GHGSat; J. Gorroño Viñegla, J. Roger Juan, and L. Guanter Palomar of LARS; Chen H., Li F., and Zhang H. of NJU; A. Hayden, J. Jonik, and J. Christy of Maxar both for participating in the test and for coordinating tasking and data sharing from key satellites. We

acknowledge the German Aerospace Center and the Italian Space Agency for tasking the EnMAP and PRISMA satellites, respectively. Rawhide Leasing (Dana Walker) and Volta Fabrication (Mike Brandon, Walt Godsil, S.M., Merritt Norton) provided indispensable operational, logistical, and planning support for the experiment.

3. Author contributions

Conceptualization – EDS and ARB. Methods – EDS, SHE, YC, JSR, and ARB. Software – EDS, PMB, ZC, and SHE. Validation – EDS. Formal analysis – EDS, PMB, ZZ, and SHE. Investigation – EDS and SHE. Resources – ARB. Data curation – EDS, PMB, YC, ZZ, ZC, JSR, and SHE. Writing: original draft – EDS. Writing: review and editing – All authors. Supervision – EDS and ARB. Project administration – EDS, SEA, and ARB. Funding acquisition – EDS, SHE, ARB.

4. Supplementary information available

The online version contains supplementary material.

5. Funding sources

This study was funded by: The Environmental Defense Fund, the Global Methane Hub, the International Methane Emissions Observatory, and the Stanford Natural Gas Initiative, an industry consortium that supports independent research at Stanford University.

6. Competing interests

ARB serves on the Science and Measurement advisory committee of Carbon Mapper, which plans to launch a methane-sensing satellite. YC and ZZ previously worked as interns at Carbon Mapper. The remaining authors have no competing interests to declare.

7. References

1. Lauvaux, T. *et al.* Global Assessment of Oil and Gas Methane Ultra-Emitters. *Science* **375**, 557–561 (2022).

2. Irakulis-Loitxate, I., Gorroño, J., Zavala-Araiza, D. & Guanter, L. Satellites Detect a Methane Ultra-emission Event from an Offshore Platform in the Gulf of Mexico. *Environ. Sci. Technol. Lett.* **9**, 520–525 (2022).

3. Pandey, S. *et al.* Satellite observations reveal extreme methane leakage from a natural gas well blowout. *Proc. Natl. Acad. Sci. U.S.A.* **116**, 26376–26381 (2019).

4. Sánchez-García, E., Gorroño, J., Irakulis-Loitxate, I., Varon, D. J. & Guanter, L. *Mapping methane plumes at very high spatial resolution with the WorldView-3 satellite*.

https://amt.copernicus.org/preprints/amt-2021-238/amt-2021-238.pdf (2021) doi:10.5194/amt-2021-238.

5. Varon, D. J. *et al.* Quantifying methane point sources from fine-scale satellite observations of atmospheric methane plumes. *Atmos. Meas. Tech.* **11**, 5673–5686 (2018).
6. Irakulis-Loitxate, I., Guanter, L., Maasakkers, J. D., Zavala-Araiza, D. & Aben, I. Satellites Detect Abatable Super-Emissions in One of the World's Largest Methane Hotspot Regions. *Environ. Sci. Technol.* **56**, 2143–2152 (2022).
7. Varon, D. J. *et al.* High-frequency monitoring of anomalous methane point sources with multispectral Sentinel-2 satellite observations. *Atmos. Meas. Tech.* **14**, 2771–2785 (2021).
8. Varon, D. J. *et al.* Satellite Discovery of Anomalously Large Methane Point Sources From Oil/Gas Production. *Geophys. Res. Lett.* **46**, 13507–13516 (2019).
9. Cusworth, D. H. *et al.* Strong methane point sources contribute a disproportionate fraction of total emissions across multiple basins in the United States. *Proc. Natl. Acad. Sci. U.S.A.* **119**, e2202338119 (2022).
10. Duren, R. M. *et al.* California's methane super-emitters. *Nature* **575**, 180–184 (2019).
11. Chen, Y. *et al.* Quantifying Regional Methane Emissions in the New Mexico Permian Basin with a Comprehensive Aerial Survey. *Environ. Sci. Technol.* **56**, 4317–4323 (2022).
12. Sherwin, E. *et al. Quantifying oil and natural gas system emissions using one million aerial site measurements*. https://www.researchsquare.com/article/rs-2406848/v1 (2023) doi:10.21203/rs.3.rs-2406848/v1.
13. Jacob, D. J. *et al.* Quantifying methane emissions from the global scale down to point sources using satellite observations of atmospheric methane. *Atmos. Chem. Phys.* **22**, 9617–9646 (2022).

14. Sherwin, E. D. *et al.* Single-blind validation of space-based point-source detection and quantification of onshore methane emissions. *Sci Rep* **13**, 3836 (2023).
15. Rutherford, J. S. *et al.* Evaluating methane emission quantification performance and uncertainty via high-volume single-blind controlled releases. Preprint at (2023).
16. Bell, C., Ilonze, C., Duggan, A. & Zimmerle, D. Performance of continuous emission monitoring solutions under single-blind controlled testing protocol. 38.
17. Bell, C. *et al.* Single-blind determination of methane detection limits and quantification accuracy using aircraft-based LiDAR. *Elementa: Science of the Anthropocene* **10**, 00080 (2022).
18. Sherwin, E. D., Chen, Y., Ravikumar, A. P. & Brandt, A. R. Single-blind test of airplane-based hyperspectral methane detection via controlled releases. *Elementa: Science of the Anthropocene* **9**, 00063 (2021).
19. Bell, C. S., Vaughn, T. & Zimmerle, D. Evaluation of next generation emission measurement technologies under repeatable test protocols. *Elementa: Science of the Anthropocene* **8**, 32 (2020).
20. Ravikumar, A. P. *et al.* Single-blind Inter-comparison of Methane Detection Technologies - Results from the Stanford/EDF Mobile Monitoring Challenge. *Elementa: Science of the Anthropocene* **7**, 29 (2019).
21. EnMAP. *EnMAP: Mission*. https://www.enmap.org/mission/ (2023).
22. Xinhua. China launches new remote sensing satellite. *XinhuaNet* (2022).
23. Song, Q., Ma, C., Liu, J. & Wei, H. Quantifying ocean surface green tides using high-spatial resolution thermal images. *Opt. Express* **30**, 36592 (2022).

24. Irakulis-Loitxate, I. *et al.* Satellite-based survey of extreme methane emissions in the Permian basin. *Sci. Adv.* **7**, eabf4507 (2021).
25. Zimmerle, D. *METEC Controlled Test Protocol: Survey Emission Detection And Quantification*. https://mountainscholar.org/handle/10217/235363 (2022).
26. ESA. *About GHGSat*. https://earth.esa.int/eogateway/missions/ghgsat (2022).
27. Jervis, D. *et al.* The GHGSat-D imaging spectrometer. *Atmos. Meas. Tech.* **14**, 2127–2140 (2021).
28. ESA. *Earth Online: Worldview-3*. https://earth.esa.int/eogateway/missions/worldview-3 (2022).
29. OHBI. *Satellites & Missions: PRISMA*. https://www.ohb-italia.it/satellites-missions/ (2022).
30. Liu, Y.-N. *et al.* The Advanced Hyperspectral Imager: Aboard China's GaoFen-5 Satellite. *IEEE Geosci. Remote Sens. Mag.* **7**, 23–32 (2019).
31. USGS. *Landsat 8*. https://www.usgs.gov/landsat-missions/landsat-8 (2022).
32. ESA. *Sentinel Online: Sentinel-2*. https://sentinel.esa.int/web/sentinel/missions/sentinel-2 (2022).
33. Zhong, B. *et al.* Analysis Ready Data of the Chinese GaoFen Satellite Data. *Remote Sensing* **13**, 1709 (2021).
34. Gorroño, J., Varon, D. J., Irakulis-Loitxate, I. & Guanter, L. Understanding the potential of Sentinel-2 for monitoring methane point emissions. *Atmos. Meas. Tech.* **16**, 89–107 (2023).
35. ESA. *Sentinel-2*. https://sentinel.esa.int/web/sentinel/missions/sentinel-2 (2021).
36. Zhang, B. *et al.* Retrieving soil heavy metals concentrations based on GaoFen-5 hyperspectral satellite image at an opencast coal mine, Inner Mongolia, China. *Environmental Pollution* **300**, 118981 (2022).

37. Luo, H. *et al.* Greenhouse Gases Monitoring Instrument on GaoFen-5 Satellite-II: Optical Design and Evaluation. *Remote Sensing* **15**, 1105 (2023).
38. ESA. *Sentinel-5P*. https://sentinel.esa.int/web/sentinel/missions/sentinel-5p (2021).
39. Wang, A. & Lee, J. J. *Methane 'Super-Emitters' Mapped by NASA's New Earth Space Mission*. https://www.nasa.gov/feature/jpl/methane-super-emitters-mapped-by-nasa-s-new-earth-space-mission (2022).
40. GHGSat. *Global leader in remote sensing of greenhouse gas*. https://www.ghgsat.com/en/who-we-are/ (2022).
41. Kayrros. *A partner for today and the future, agile with technology and with a smarter approach to data*. https://www.kayrros.com/who-are-we/ (2022).
42. Scott, W. *Mapping Methane Emissions Using Maxar's WorldView-3 Satellite*. https://blog.maxar.com/earth-intelligence/2022/mapping-methane-emissions-using-maxars-worldview-3-satellite (2022).
43. Orbio. *Actionable Methane Intelligence: Filling the global methane gap with asset-level emissions data*. https://www.orbio.earth/ (2023).
44. Irakulis-Loitxate, I., Gorroño, J., Zavala-Araiza, D. & Guanter, L. *Satellites detect a methane ultra-emission event from an offshore platform in the Gulf of Mexico*. http://eartharxiv.org/repository/view/3222/ (2022) doi:10.31223/X5504G.
45. Guanter, L. *et al. Mapping methane point emissions with the PRISMA spaceborne imaging spectrometer*. http://eartharxiv.org/repository/view/2344/ (2021) doi:10.31223/X5VC9C.
46. Jia, M. *et al.* The Nord Stream pipeline gas leaks released approximately 220,000 tonnes of methane into the atmosphere. *Environmental Science and Ecotechnology* **12**, 100210 (2022).

47. El Abbadi, S. *et al. Comprehensive evaluation of aircraft-based methane sensing for greenhouse gas mitigation*. https://eartharxiv.org/repository/view/5569/ (2023) doi:10.31223/X51D4C.

48. Bell, C. S. *et al.* Comparison of methane emission estimates from multiple measurement techniques at natural gas production pads. *Elementa: Science of the Anthropocene* **5**, 79 (2017).

49. Cusworth, D. H. *et al.* Intermittency of Large Methane Emitters in the Permian Basin. *Environ. Sci. Technol. Lett.* **8**, 567–573 (2021).

50. Hayden, A. & Christy, J. Maxar's WorldView-3 Enables Low-Concentration Methane Detection from Space. Preprint at https://doi.org/10.31223/X51T1C (2023).

51. Rutherford, J., Sherwin, E., Chen, Y., Aminfard, S. & Brandt, A. R. Evaluating methane emission quantification performance and uncertainty of aerial technologies via high-volume single-blind controlled releases. Preprint at https://doi.org/10.31223/X5KQ0X (2023).

52. Sun, Y., Szücs, G. & Brandt, A. R. Solar PV output prediction from video streams using convolutional neural networks. *Energy Environ. Sci.* 8 (2018).

53. NASA. *NASA Earth Observations Cloud Fraction (1 Month TERRA/MODIS)*. https://neo.gsfc.nasa.gov/view.php?datasetId=MODAL2_M_CLD_FR&date=2022-06-01 (2023).

54. Jongaramrungruang, S., Thorpe, A. K., Matheou, G. & Frankenberg, C. MethaNet – An AI-driven approach to quantifying methane point-source emission from high-resolution 2-D plume imagery. *Remote Sensing of Environment* **269**, 112809 (2022).

55. Chulakadabba, A. *et al.* Methane Point Source Quantification Using MethaneAIR: A New Airborne Imaging Spectrometer. (2023).

56. ESA. *Sentinel-5P: Global Air Monitoring for Copernicus*. https://esamultimedia.esa.int/docs/EarthObservation/Sentinel-5p_factsheet_171211.pdf (2022).
57. EnMAP. *EnMAP Instrument Planning*. https://planning.enmap.org/ (2022).
58. GHGSat. *Greenhouse Gas Monitoring from Space: GHGSat Launches Three New Satellites with SpaceX*. https://www.ghgsat.com/en/newsroom/greenhouse-gas-monitoring-from-space-ghgsat-launches-three-new-satellites-with-spacex/ (2022).
59. GHGSat. *3 New Methane Monitoring Satellites Make Contact in Record-Time*. https://www.ghgsat.com/en/newsroom/three-new-methane-monitoring-satellites-make-contact-in-record-time/ (2023).
60. ESA. *GHGSat data now available through ESA's Earthnet programme*. https://earth.esa.int/eogateway/news/ghgsat-data-now-available-through-esa-s-earthnet-programme (2021).
61. NASA. *Landsat 9*. https://landsat.gsfc.nasa.gov/satellites/landsat-9/ (2023).
62. USGS. *Landsat Data Access*. https://www.usgs.gov/landsat-missions/landsat-data-access (2022).
63. ESA. *Sentinel-2: About the launch*. https://www.esa.int/Applications/Observing_the_Earth/Copernicus/Sentinel-2/About_the_launch.
64. ESA. *Sentinel-2 User Handbook*. 64 https://sentinel.esa.int/documents/247904/685211/Sentinel-2_User_Handbook (2015).
65. ESA. *Access to Sentinel data via download*. https://sentinel.esa.int/web/sentinel/sentinel-data-access (2021).

66. ESA. *WorldView-3 full archive and tasking*. https://earth.esa.int/eogateway/catalog/worldview-3-full-archive-and-tasking (2022).
67. NASA. *GEOS Near-Real Time Data Products*. https://gmao.gsfc.nasa.gov/GMAO_products/NRT_products.php (2021).
68. ECMWF. *ERA5*. https://www.ecmwf.int/en/forecasts/datasets/reanalysis-datasets/era5 (2022).
69. NOAA. *The High-Resolution Rapid Refresh (HRRR)*. https://rapidrefresh.noaa.gov/hrrr/ (2022).
70. CEOS. *A Constellation Architecture for Monitoring Carbon Dioxide and Methane from Space*. https://ceos.org/document_management/Virtual_Constellations/ACC/Documents/CEOS_AC-VC_GHG_White_Paper_Publication_Draft2_20181111.pdf (2018).
71. Frankenberg, C. *et al.* Airborne methane remote measurements reveal heavy-tail flux distribution in Four Corners region. *Proc Natl Acad Sci USA* **113**, 9734–9739 (2016).
72. Satelytics. *Satelytics solves the most pressing industrial challenges*. https://www.satelytics.com/ (2023).

This manuscript is a non-peer reviewed preprint submitted to EarthArXiv

Supplementary information for "Single-blind test of nine methane-sensing satellite systems from three continents"

Authors: Evan D. Sherwin[1,*], Sahar H. El Abbadi[1], Philippine M. Burdeau[1], Zhan Zhang[1], Zhenlin Chen[1], Jeffrey S. Rutherford[1,a], Yuanlei Chen[1], Adam R. Brandt[1]

Author Affiliations:

[1] Department of Energy Science & Engineering, Stanford University, Stanford, California 94305, United States

[a] Present affiliation: Highwood Emissions Management, Calgary, Alberta T2P 2V1, Canada

[*] Correspondence: evands@stanford.edu

Table of contents

S1. Participating satellites
S2. Participating teams
S3. Supplementary methods
S4. Supplementary results

S1. Supplementary methods

S.1.1. Advancing Development of Emissions Detection Protocol

The single-blind controlled methane release testing in this study followed the Advancing Development of Emissions Detection (ADED) protocol, developed at the Methane Emissions Technology Evaluation Center (METEC) in Colorado [25].

We followed protocols from Section 10, "Aerial Survey Emission Detection And Quantification," which was designed to apply to remote sensing technologies in general, including satellites [25].

Documentation of the system under test is included both within this paper as well as in the "Performer Info" tab of the data spreadsheets submitted by each team, which are available in the GitHup repository associated with this paper. Submitted emissions estimates used the standard template spreadsheet for the Aerial Survey Emission Detection And Quantification version of the ADED protocol [25].

Following Section 10.1.1 of the ADED protocol, all teams were required to notify the Stanford team in advance of the flight pattens they intended to fly, including orientation. Teams were required to explain any deviations from this flight plan, e.g. due to inclement weather conditions [25].

Following Section 10.4.1 of the ADED protocol, the test location was at least 1 km away from all potential confounding methane sources, e.g. the local landfill, and from all nearby water features [25].

S.1.2. Flow rate estimation

Unless otherwise specified, all methane flow rate estimates are the average flow rate over the five minutes preceding a timestamp. Meters produce a whole-gas mass flow rate, which we convert to a methane flow rate using the methane fraction provided in natural gas composition measurements conducted at the two metering stations upstream of the vendor from which we purchased compressed natural gas. For each truck refill, we estimate the methane mole fraction as the average of the daily measurements from the five previous days leading up to and including the refill, averaging over both metering stations, as discussed in El Abbadi et al. [47].

S.1.3. Exclusion criteria

Stanford excluded emissions for the following reasons:

1. If there was a system malfunction resulting in an emission without reliable metering.
2. If the team was notified in advance that Stanford would not be releasing on a given day.
3. If a satellite was tasked without notice to a date outside of the testing period or on a United States national holiday.
4. Stanford release planners were unaware of 14 Sentinel-2 overpasses during the testing period and excluded them from analysis. These include overpasses on October 11th, 14th, 16th, 19th, 21st, 24th, 29th, and 31st, and November 3rd, 10th, 13th, 20th, 23rd, and 30th.

5. Before analyzing results, we had planned to exclude all emissions with metered flow standard deviation, accounting for all sources of variability and uncertainty, greater than 10%. In practice, the only emission that met this threshold was the sole valid GF5 overpass, which was rescheduled without notice to one minute after the emission was shut down. As a result, we include this emission in the main paper, with the appropriate caveats.

Teams were allowed to exclude measurements for any reason. In practice, the most common reason given was cloud cover.

S.1.4. Excluded nonzero ZY1 release

We exclude the October 20th ZY1 release from analysis in the main manuscript due to a system malfunction in the release and metering apparatus. As a result of the malfunction, there was no log of the precise meter readings. Because of the system malfunction, the Stanford field team cut gas approximately one minute before the ZY1 overpass. However, all three teams analyzing ZY1 data detected methane in the acquired spectral data.

In supplementary analysis, we use the targeted rate of 0.998 t(gas)/h as our central estimate, and add a symmetric 95% confidence interval based on the maximum measured release value of 1.607 t(gas)/h, resulting in a lower-end errorbar estimated at 0.389 t(gas)/h. This translates to an estimated methane emission rate of 0.944 [0.367, 1.520] t(CH_4)/h.

S2. Participating satellites

This section is adapted in part, with permission, from Sherwin et al. 2023 [14].

Nine satellite constellations were available to collect measurements during the study period of October 10th-November 30th, 2022. This included targeted satellites systems EnMAP, Gaofen 5 (GF5), GHGSat-C, PRISMA, WorldView-3, and Ziyuan 1 (ZY1) which must be tasked to focus on a particular area, as well as global-coverage satellites Huanjing 2 (HJ2), Landsat 8/9, and Sentinel-2, which passively collect data from nearly all inhabited areas of the world [26,28,29,31,35,56].

Table 1 summarizes the spectral resolution, spatial coverage, constellation size, swath width, revisit time, and data availability.

Note that only the GHGSat instruments were originally designed for the primary purpose of detecting and quantifying methane emissions. With the remaining satellites, researchers have developed methane retrieval techniques based on existing data, e.g. citations [1,6,7,24].

S.2.1. EnMAP

The Environmental Mapping and Analysis Program (EnMAP) satellite is a collaborative effort led by the German Space Agency and the German Research Center for Geosciences. The satellite launched on April 1, 2022. This targeted hyperspectral instrument uses spectral bands ranging from 420-2,450 nm with a 30 km swath, operating with a 4-day maximum revisit frequency and 27-day nadir revisit frequency . Data from EnMAP are publicly available, and the satellite can be tasked upon request [57].

S.2.2. Gaofen 5 (GF5)

Gaofen 5-02 (GF5) Advanced Hyperspectral Imager satellite is the latest in a series of GF5 satellites launched by the Chinese government on September 7, 2021 [37]. This targeted hyperspectral instrument uses spectral bands ranging from 759-2,058 nm with a 60 km swath [36,37]. Based on the satellite overpass dates submitted by NJU for the testing period, October 15th, November 15th, November 23rd, and November 30th, it appears that GF5-02 is capable of revisiting a location within at least 7 days. Data from GF5 can be made available upon request from the relevant government agencies.

S.2.3. GHGSat-C

At the time of testing, the GHGSat-C satellite series consisted of a constellation of eight instruments launched by the Canada-based private company GHGSat. GHGSat-C1 launched on September 2, 2020, followed by GHGSat-C2 on January 24, 2021 and GHGSat-C3-C5 launched May 25, 2022 [58]. GHGSat-C6-C8 were launched on April 15th, 2023 [59]. The precursor GHGSat-D satellite was launched on June 22, 2016. Several additional satellites are scheduled to launch in the coming years, with a goal of achieving a 10-satellite constellation by 2023 [26].

GHGSat-C satellites each complete 15 orbits per day, with an average repeat cycle of approximately 14-days. Each satellite is equipped with a multispectral Wide-Angle Fabry-Perot (WAF-P) Imaging Spectrometer, focusing on a proprietary combination of unpolarized short-wave infrared frequencies from 1630-1675 nm at 25m spatial resolution, as well as a secondary VIS-1 Visible Sensor in the optical frequency range at <20m spatial resolution. The sensor has a 12 km-wide field-of-view, which can be targeted toward a desired location. GHGSat claims a detection threshold of 0.1 t(CH_4)/h at 3 m/s winds, with methane column density precision at 1% of background [26].

GHGSat operates commercially, but offers access to data archives as well as tasking to scientific researchers for select proposals [60].

S.2.4. Huanjing 2 (HJ2)

Huanjing 2 (HJ2) is a constellation of two satellites, HJ2A and HJ2B, launched by the Chinese government in 2020 [33]. This system has an 800 km swath [33]. The spectral bands from data files shared with all teams include 100 visible to near infrared (VNIR) bands from 450-920 nm, with 115 short-wave infrared (SWIR) bands from 900-2500 nm. Based on the satellite overpass dates submitted by NJU for the testing period, November 2nd and November 6th, it appears that HJ2B is capable of revisiting a location within at least 4 days. Data from HJ2 can be made available upon request from the relevant government agencies.

S.2.5. Landsat 8/9

Launched on February 11, 2013 and September 27, 2021, respectively, the Landsat 8 and 9 satellites are is the product of a collaboration between the National Aeronautics and Space Administration (NASA) and the United States Geological Survey (USGS), both agencies of the United States government [31,61]. Both instruments have global coverage, collecting data for all inhabited areas of the world every 16 days (with the two instruments 8 days out of phase) with a 185 km swath. Both satellites hosts a 9-band operational land imager, including two SWIR bands at 1570-1650 nm and 2110-2290 nm, as well as four visible bands, all at 30 m resolution. An

onboard thermal infrared sensor also collects two bands at 10,600-11,190 nm and 11,500-12,510 nm, both at 100 m resolution [31,61]. All data from Landsat 8 and 9 are publicly available on the USGS website [62].

S.2.6. PRISMA

Launched March 19, 2019, the PRISMA (PRecursore IperSpettrale della Missione Applicativa) satellite is a product of the Italian Space Agency (ASI), contracting through Orbitale Hochtechnologie Bremen (OHB) Italia S.p.A. This targeted hyperspectral instrument uses spectral bands ranging from 400-2,500 nm with a 30 km swath, operating with a 7-day maximum revisit frequency. Data from PRISMA are publicly available, and the satellite can be tasked upon request [29].

S.2.7. Sentinel-2

The two-satellite Sentinel-2 constellation consists of Sentinel 2A, launched June 23, 2015, and Sentinel 2B, launched March 7, 2017 as part of the European Union's Copernicus program [63]. The satellites operate in the same 10-day polar orbit offset by 180°, resulting in 5-day revisit times at the equator, falling to 2-3 days at mid-latitudes. Each satellite collects data for all inhabited areas of the world each orbit with a 290 km swath with thirteen spectral bands in the SWIR and VNIR ranges. This includes four bands at 10 m resolution, six bands at 20m resolution (including Band 12 at 2190 nm in the SWIR range), and three bands at 60m resolution [64]. All data from Sentinel-2 are publicly available at [65].

Due to a miscommunication, Stanford did not conduct releases for 17 of the 23 Sentinel-2 overpasses during the study period. These data points are excluded from all analysis. Teams had access to the imagery collected during those overpasses, but would not necessarily know whether we were conducting releases at those times.

S.2.8. WorldView-3

Launched August 13, 2014, the WorldView-3 satellite is owned and operated by United States-based company Maxar. This multispectral instrument measures in one panchromatic band, eight multispectral bands in the visible near infrared range, eight SWIR bands (1195-2365 nm), and twelve bands covering clouds, aerosols, vapors, ice, and snow. This targeted instrument has an 13.1 km swath and a revisit frequency of 4.5 days at 20° off-nadir for maximum resolution [28].

WorldView-3 operates commercially. Researchers may submit proposals to access data archives and request satellite tasking [66].

S.2.9. Ziyuan 1

Ziyuan 1E (ZY1) Advanced Hyperspectral Imager satellite is the latest in a series of ZY1 satellites launched by the Chinese government on December 26, 2021 [23]. This targeted hyperspectral instrument uses 76 visible and near infrared bands at 10 nm spectral resolution, with 90 short-wave infrared bands at 20 nm spectral resolution, both with a 60 km swath and 30 m pixels [23]. Based on the satellite overpass dates submitted by NJU for the testing period, October 20th, 21st, 23rd, 26th, and 27th, it appears that ZY1 is capable of revisiting a location as frequently as every day. Data from ZY1 can be made available upon request from the relevant government agencies.

S.2.10. Data submission timeline

Table 2. Data submission timeline by stage for each team. Includes the dates at which 1) teams submitted fully blind Stage 1 results, 2) teams received unblinded in situ wind data from the on-site 10 m ultrasonic anemometer, and 3) teams submitted Stage 2 results using in situ wind measurements. All teams were provided with satellite data as the Stanford team received it. In some instances, providing data to the Stanford team, with the final spectral data arriving February 15th, 2023. This data availability delay introduced additional latency into Stage 1 submission that was beyond teams' control.

Operator	Submitted Stage 1	Received Wind Data	Submitted Stage 2
GHGSat	5-Feb-23	23-Feb-23	2-Mar-23
Kayrros	2-Mar-23	3-Mar-23	7-Mar-23
LARS	2-Mar-23	2-Mar-23	3-Mar-23
Maxar	1-Mar-23	3-Mar-23	6-Mar-23
NJU	2-Mar-23	2-Mar-23	7-Mar-23
Orbio Earth	16-Feb-23	23-Feb-23	6-Mar-23

S3. Participating teams

This section is adapted in part, with permission, from Sherwin et al. 2023 [14].

Six teams participated in this single-blind study, each using data from a subset of the nine participating satellites.

We invited all teams of which we were aware that estimate methane emissions from any of the nine participating satellites. Teams that declined to participate are listed at the end.

Each team was given the option to produce methane retrievals for up to five participating satellites. GHGSat was the only company with access to data from GHGSat-C satellites and was thus the only team able to produce an estimate from that satellite, as shown in Table S1.

Table S1. Satellites (columns) analyzed by each team (rows). The final column is the reported source for 10 m wind data for fully blind estimates.

Team	GHGSat	Kayrros	LARS	Maxar	NJU	Orbio Earth
EnMAP		X	X	X	X	
GF5		X	X		X	
GHGSat-C	X					
HJ2			X		X	
Landsat		X		X	X	
PRISMA		X	X	X	X	
Sentinel-2	X	X		X	X	X
WorldView-3		X	X	X	X	
ZY1		X	X		X	
Wind source	GEOS-FP	ECMWF ERA5, HRRR	ECMWF ERA5, GEOS-FP	Wunderground.com, Windy.com	GEOS-FP	GEOS-FP

In fully blind stage 1 estimates, most teams used wind reanalysis data from NASA Goddard Earth Observing System-Fast Processing (NASA GEOS-FP) at 10 m, Fifth generation European Centre for Medium-Range Weather Forecasts Atmospheric Reanalysis of the global climate (ECMWF ERA5), or both [67,68]. Kayrros supplemented ECMWF ERA5 data with the National Oceanographic and Atmospheric Administration (NOAA) High Resolution Rapid Refresh (HRRR) reanalysis product, which focuses on the United States [69]. Maxar used data from Wunderground.com for the Phoenix Sky Harbor airport for most estimates, with WorldView-3 estimates averaging wind speed data from Windy.com for the three weather stations nearest the test site, Casa Grande Municipal Airport, FW1331 Casa Grande, and FW9639 Casa Grande.

See Performer Information spreadsheets in the GitHub repository for additional detail on the wind speed used by each team.

S.3.1. GHGSat

GHGSat is a private company, based in Canada, specializing in remote sensing of greenhouse gas emissions. GHGSat owns a constellation of satellites, currently including GHGSat D as well as the more recent GHGSat-C1-C5 instruments, with further satellites scheduled for launch in coming years [70]. GHGSat also submitted estimates for Sentinel-2.

Firmware installed on the instruments was as follows:
GHGSat-C2 Firmware version: 10.9.3-gb41c76f
GHGSat-C2 Observation script: N251A98E.GSB
GHGSat-C3+ Firmware version: 10.29.0
GHGSat-C3+ Observation script for : NE36DDC3.GSB

Methane retrievals were then conducted using toolchain version 9.8.0, via the ghg-ops-srr v0.11.1 source rate retrieval algorithm. See the “Performer Info” tab of the GHGSat reported data spreadsheet, included in the GitHub repository, for further detail.

S.3.2. Kayrros

Kayrros is a private company specializing in reanalysis of public and private satellite data, with a major area of focus in remote sensing of methane. Kayrros produced estimates for all satellites except GHGSat-C and HJ2.

See the "Performer Info" tab of the Kayrros reported data spreadsheets (available in the GitHub repository) for further detail on the approach used in this test.

S.3.3. Land and Atmosphere Remote Sensing group (Universitat Politècnica de València)

Researchers Prof. Luís Guanter, Javier Roger Juan, Dr. Javier Gorroño Viñegla of Universitat Politècnica de València in the Land and Atmosphere Remote Sensing (LARS) group in Spain produced estimates for all satellites except GHGSat C, LandSat, and Sentinel-2.

LARS researchers did not report the details of their retrieval algorithms in this study but did so in other studies. In Irakulis-Loitxate et al., the LARS group used a matched filter-based method for PRISMA, ZY1 retrievals in [24], and for Sentinel-2 and Landsat 8 retrievals in [6]. In Sánchez-García et al. [4], the LARS group applies a retrieval method derived from Frankenberg et al. 2016 and Varon et al. 2018 [5,71] to estimate methane emission rates using WorldView-3.

Dr. Gorroño Viñegla submitted fully blinded WorldView-3 quantification estimates after winds had been unblinded to J. Roger Juan. Although Stanford researchers are confident Dr. Gorroño Viñegla did not receive in situ wind measurements before submitting these results, we do not include them in the main analysis for consistency across all teams and to maintain a strict standard for integrity of the blind. We include these results, as well as results using in situ wind submitted after the conclusion of the blind, in the SI, Section S4 with appropriate caveats. The fact that results submitted using in situ wind differ substantially from initial blinded results further points to the integrity of fully blinded results.

S.3.4. Maxar

Maxar is a private company based in the United States, both operating and analyzing data from satellites [50]. In particular, Maxar owns and operates the WorldView-3 satellite, using it and other satellites to, among other things, detect and quantify methane emissions. Maxar submitted estimates for EnMAP, Landsat, PRISMA, Sentinel-2, and WorldView-3. Maxar submitted PRISMA quantification estimates for stage 2 only.

See Hayden and Christy 2023 for additional discussion of their approach to methane sensing [50].

S.3.5. Nanjing University

Researchers Fei Li, Prof. Huilin Chen, and Prof. Yongguang Zhang of Nanjing University in China produced estimates for all satellites except GHGSat-C.

NJU used an integrated mass enhancement (IME) model to estimate emission rates, multiplying pixel-wise IME by wind speed and dividing that product by the length of the masked plume. See the "Performer Info" tab of the NJU reported data spreadsheets (available in the GitHub repository) for further detail on the approach used in this test.

S.3.6. Orbio Earth

Orbio Earth Earth is a Germany-based company focusing on detecting and quantifying methane emissions using satellite data [43]. Orbio Earth submitted estimates for Sentinel-2 only.

According to the "Performer info" sheet of their submitted results, they employ "5 stage multi-spectral reflectance process using adaptations and combinations of peer-reviewed modelling approaches, including but not limited to Varon et al. 2021, Varon et al 2018, Ehret et al 2022, Gorroño et al 2023. Based on creating a prediction of the background reflectance of the site and comparing it to the real reflectance." All submissions used "Model version 16_2" of the Orbio Earth software system.

S.3.7. Harvard University [declined to participate]

Dr. Daniel Varon of Harvard University developed the first method for estimating methane emissions from Sentinel-2 data [7]. Dr. Varon participated in a previous single-blind test, producing estimates for Sentinel-2 [14], and declined to participate in this round of testing due to limited availability.

S.3.8. Satelytics [declined to participate]

Satelytics is a multifaceted business intelligence company based in the United States, focused on synthesizing satellite data into actionable insights [72]. Satelytics offers a methane detection and quantification service based on satellite data and was invited to participate in this test, but declined to do so.

S.3.9. Stichting Ruimte Onderzoek Nederland (SRON) [declined to participate]

SRON is the Dutch government space agency, which has a significant focus on remote sensing of methane emissions. In a previous single-blind test, Dr. Sudhanshu Pandey produced estimates for Sentinel-2 and Landsat 8 on behalf of SRON [14]. SRON declined to participate in this round of testing due to personnel limitations.

S4. Supplementary results

S.4.1. Supplementary regression results

Parts of this section are adapted with permission from Sherwin et al. 2023 [1].

To estimate the overall quantification accuracy, goodness of fit, and error distribution of all quantified methane emission estimates, we apply a linear regression. For reasons described in Sherwin et al. 2023 [1], we fix the y-intercept at zero in the regression, shown in Eq. (1).

$$y = \beta x \quad (1)$$

Where x is the mean metered emission rate, and y is the central emissions estimate provided by participating teams. These x and y values correspond to the markers in Figure 4.

The regression only includes quantified emissions, and does not include emissions that were not detected. We do this to assess the error distribution of detected emissions.

Table 1. Regression results for stages 1 and 2 based on the fixed-intercept ordinary least squares regression in Eq. (1). Maxar submitted quantification estimates for PRISMA in stage 2 only, adding two true positive data points to the stage 2 regression results.

	Stage 1	Stage 2
B	1.139 [0.832, 1.446]	1.248 [1.037, 1.459]
Standard error	0.152	0.105
t-statistic	7.502	11.937
No. Observations	41	43
Degrees of freedom (Residuals)	40	42
Degrees of freedom (Model)	1	1
Uncentered R^2	0.585	0.772
Centered R^2	0.574	0.767
F-statistic	56.3	142.5

R^2 values are presented in uncentered format, which is standard for regression specifications without a y-intercept term. As a result, these R^2 values are not directly comparable with the centered R^2 values produced in regressions with a y-intercept. Centered R^2 values, directly comparable with R^2 values from regressions with a nonzero y-intercept term, are also shown in Table 1.

Note that these regressions treat each estimate from each team and satellite as independent and identically distributed observations. This aggregation is necessary to produce a meaningful regression due to the small sample size for each satellite and team, but the results of this analysis should be treated as a rough illustration of the general capabilities of the participating satellites and teams as a whole. Detailed characterization of the quantification accuracy from individual satellites and teams will require more datapoints.

S.4.2. Error statistics by satellite and team

Recall in interpreting these results that Maxar concluded after results were unblinded that their results were high by a factor of roughly 2.3 due to use of a deprecated spectral library [2].

Table 2. Stage 1 (fully blind) summary statistics of quantified (non-zero) emissions by satellite, across all teams. Excludes LARS WorldView-3 quantification estimates, consistent with the main analysis, because their results were Stage 1 results were submitted after winds had been unblinded to a member of the LARS team analyzing other satellites. We report min, mean, max, and standard deviation.

Stage 1					
	Count	Min	Mean	Max	σ
EnMAP	3	40%	55%	68%	14%
Gaofen 5	3	-5%	-2%	0%	2%
GHGSat C	1	24%	24%	24%	NA
Huanjin 2B	0	NA	NA	NA	NA
LandSat 8/9	2	-55%	-53%	-51%	3%
PRISMA	4	-54%	19%	59%	52%
Sentinel-2	11	-53%	38%	456%	153%
WorldView-3	14	-56%	33%	192%	74%
Ziyuan 1	6	-30%	39%	131%	58%

Table 3. Stage 2 (with 10 m in situ wind measurements) summary statistics of quantified (non-zero) emissions by satellite, across all teams. Excludes LARS WorldView-3 quantification estimates, consistent with the main analysis. Maxar submitted PRISMA quantification estimates in stage 2 only.

Stage 2					
	Count	Min	Mean	Max	σ
EnMAP	3	65%	75%	93%	16%
Gaofen 5	3	13%	24%	31%	9%
GHGSat C	1	-42%	-42%	-42%	NA
Huanjin 2B	0	NA	NA	NA	NA
LandSat 8/9	2	-53%	-39%	-25%	20%
PRISMA	6	-24%	46%	181%	79%
Sentinel-2	11	-56%	4%	193%	76%
WorldView-3	14	-52%	40%	140%	67%
Ziyuan 1	6	-51%	35%	119%	70%

Table 4. Stage 1 (fully blind) summary statistics of quantified (non-zero) emissions by team, across all satellites.

Stage 1					
	Count	Min	Mean	Max	σ
GHGSat	4	-53%	25%	170%	102%
Kayrros	14	-55%	13%	131%	54%
LARS	6	-54%	24%	59%	44%
MAXAR	11	-14%	125%	456%	136%
NJU	7	-56%	-24%	20%	27%
Orbio Earth	4	-47%	-27%	-9%	18%

Table 5. Stage 2 (with 10 m in situ wind measurements) summary statistics of quantified (non-zero) emissions by team, across all satellites.

Stage 2					
	Count	Min	Mean	Max	σ
GHGSat	4	-56%	-33%	-13%	20%
Kayrros	14	-53%	16%	106%	44%
LARS	6	8%	42%	119%	43%
MAXAR	11	-24%	101%	193%	69%
NJU	7	-52%	-7%	99%	52%
Orbio Earth	4	-54%	-34%	-8%	20%

S.4.3. Aggregate error statistics

Table 6. Summary statistics of the percent error of estimated emission rates, as well as stage 1 wind speed error. Compares central estimates with 5-minute mean measured emissions. Note that although the standard deviation of the percent error distribution falls slightly after wind unblinding in stage 2, the inter-quartile range between the 25th and 75th percentiles (P25 and P75, respectively) of the error distribution is larger in stage 2. Includes results excluding Maxar submissions both because Maxar concluded after results were unblinded that their results were high by a factor of two due to use of a deprecated spectral library [2] and because Maxar submitted only stage 2 estimates for PRISMA.

Metric	**Stage 1 (fully blind)**	**Stage 2 (measured wind)**	**Stage 1 (exclude Maxar)**	**Stage 2 (exclude Maxar)**	**Wind speed**
Mean	29%	27%	4%	4%	18%
Standard deviation	90%	67%	54%	47%	156%
Min	-56%	-56%	-56%	-56%	-87%
P25	-34%	-24%	-40%	-29%	-49%
P50 (median)	4%	12%	-5%	-6%	-36%
P75	55%	66%	44%	29%	-10%
Max	456%	193%	170%	119%	645%
Inter-quartile range (P75-P25)	89%	90%	84%	58%	39%

S.4.4. Detection summary

Table S8. Detection results by satellite and team. A tabular representation of Figure 2. Note that measurements for which Stanford filtered for all teams were excluded from Figure 2 but are included here in the # Stan. Filtered column.

Satellite/ Team	# True positive	# False negative	# True negative	# False positive	# Op. filtered	# Stan. Filtered	# Not tasked	Total
EnMap/ Kayrros	1	0	4	0	0	0	0	5
EnMap/ LARS	1	0	1	0	0	3	0	5
EnMap/ MAXAR	1	0	1	0	0	3	0	5
EnMap/ NJU	0	1	1	0	0	3	0	5
GF5/ Kayrros	1	0	0	0	0	1*	0	2
GF5/ LARS	1	0	0	0	0	1*	0	2
GF5/ NJU	1	0	0	0	0	1*	0	2
GHGSat CX/ GHGSat	1	0	1	0	3	2*	5	12
HJ2B/ LARS	0	0	1	0	0	0	0	1
HJ2B/ NJU	0	0	1	0	0	0	0	1
LandSat/ Kayrros	2	4	2	0	0	4*	0	12
LandSat/ MAXAR	0	6	2	0	0	4*	0	12
LandSat/ NJU	0	6	2	0	0	4*	0	12
PRISMA/ Kayrros	1	2	2	0	0	3*	2	10
PRISMA/ LARS	2	1	2	0	0	3*	2	10
PRISMA/ MAXAR	2	1	2	0	0	3*	2	10
PRISMA/ NJU	1	2	2	0	0	3*	2	10
Sentinel-2/ GHGSat	3	1	2	0	0	17*	0	8
Sentinel-2/	2	2	2	0	0	17*	0	8

Kayrros								
Sentinel-2/ MAXAR	2	2	2	0	0	17*	0	8
Sentinel-2/ NJU	0	4	2	0	0	17*	0	8
Sentinel-2/ Orbio Earth	4	0	2	0	0	17*	0	8
WorldView-3/Kayrros	5	2	0	0	0	3*	0	10
WorldView-3/LARS	3	2	0	0	2	3*	0	10
WorldView-3/MAXAR	6	1	0	0	0	3*	0	10
WorldView-3/NJU	3	4	0	0	0	3*	0	10
ZY1/ Kayrros	1	0	0	0	0	3*	0	4
ZY1/ LARS	1	0	0	0	0	3*	0	4
ZY1/ NJU	1	0	0	0	0	3*	0	4
Total	46	41	34	0	5	144	13	283

* These measurements were filtered for all teams and not included in Figure 2.

Table S9. Ground truth for detection by satellite. Includes the count of non-zero emissions as well as zero-emission controls given to each satellite for all measurements (all instances in which the satellite passed overhead), not including data points excluded by Stanford for all teams, including overpasses in which the satellite was not tasked.

Satellite	# Non-zero	# Zero
EnMAP	4	1
Gaofen 5	1	0
GHGSat C	9	1
Huanjin 2B	0	1
LandSat 8/9	7	3
PRISMA	4	3
Sentinel-2	4	2
WorldView-3	7	0
Ziyuan 1	1	0
Total	37	11

S.4.5. Supplementary figures

Underlying data and code to reproduce these figures are available in the data and code repository for this paper, particularly in "Satellite_results_consolidated_clean_20230526b.csv".

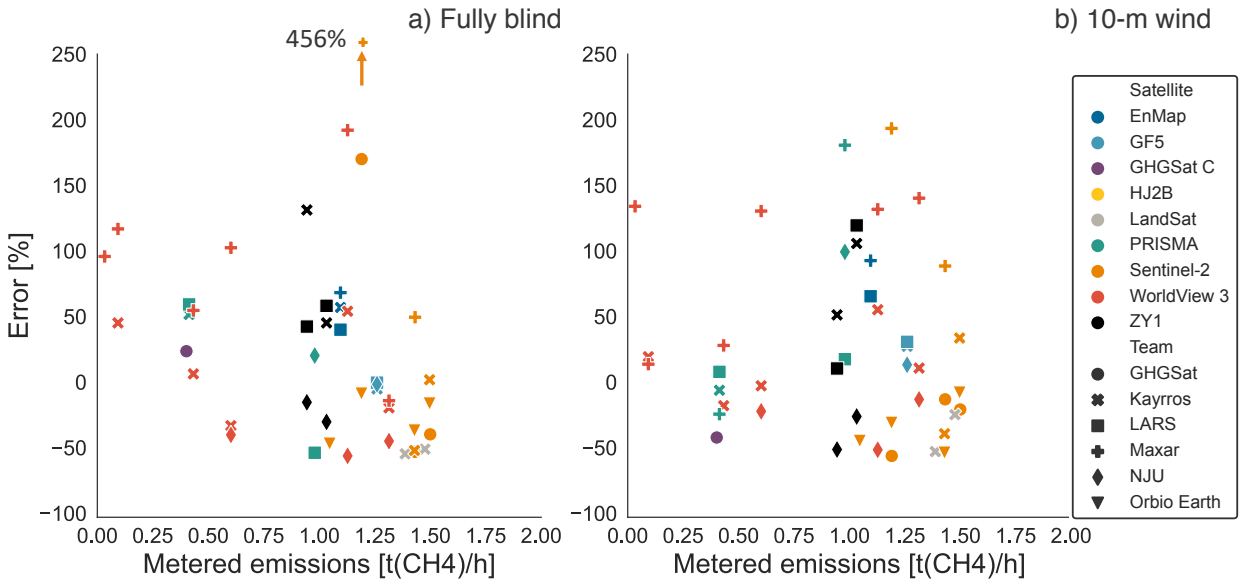


Figure 1. Percent error for Stage 1 (fully blind) and Stage 2 (with measured 10 m wind speed and direction).

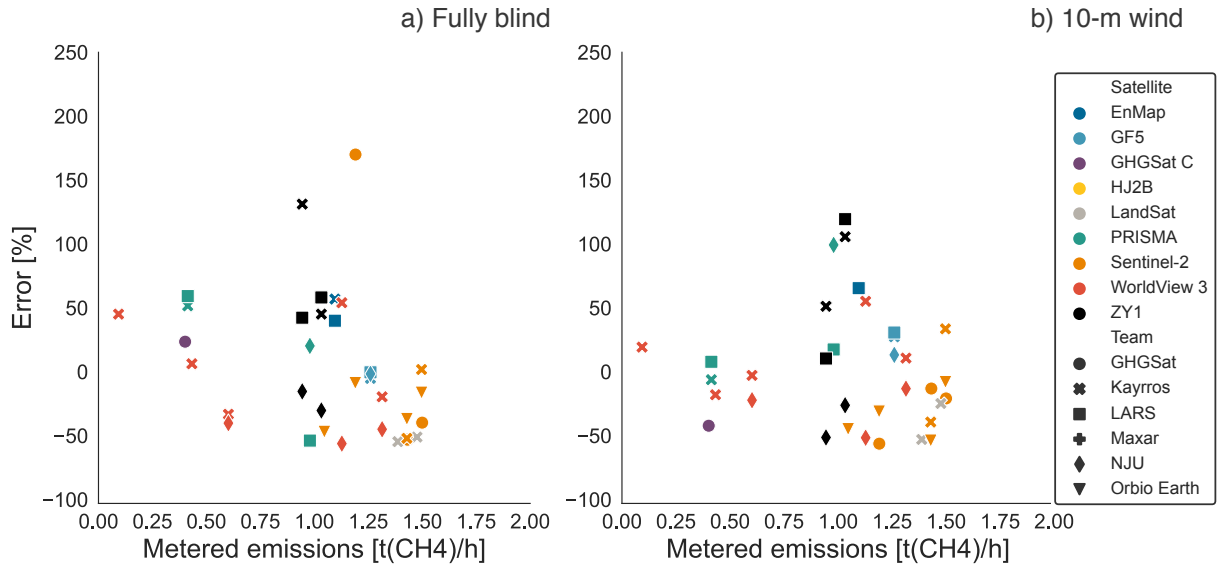


Figure 2. Percent error excluding Maxar estimates, which Maxar now believes were artificially high by a factor of two [2]. Stage 1 (fully blind) and Stage 2 (with measured 10 m wind speed and direction).

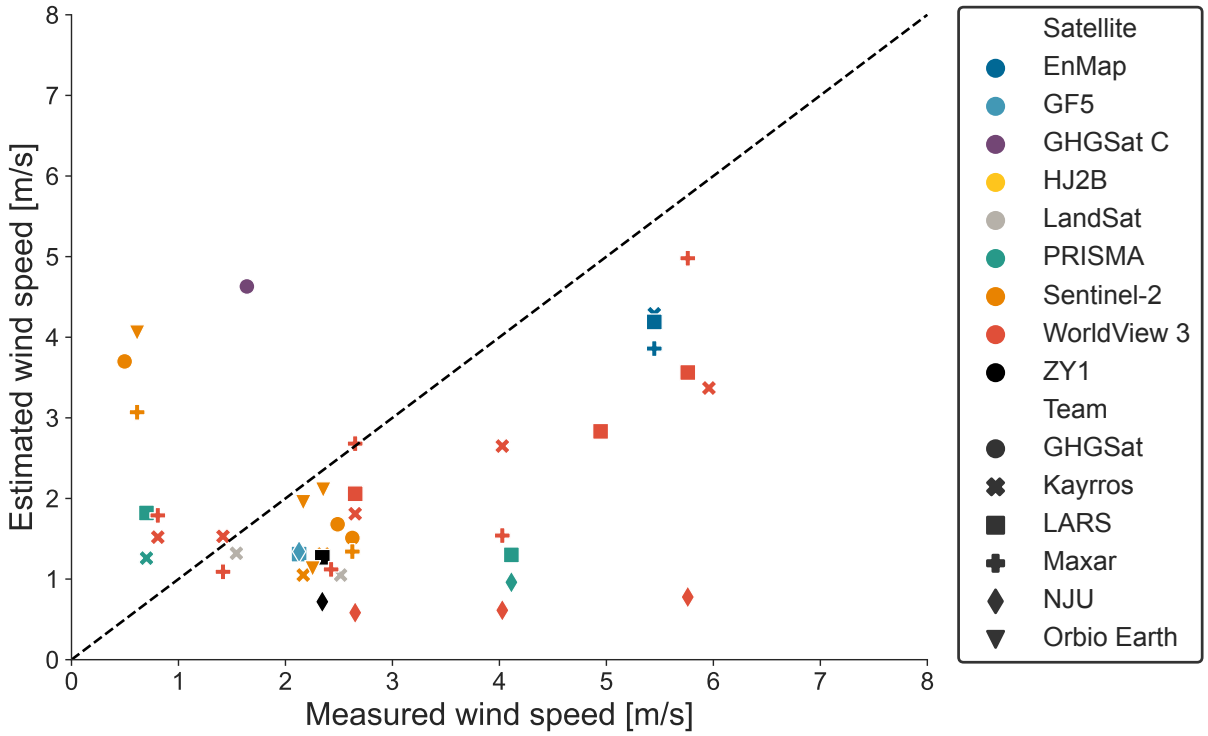


Figure 3. Parity chart of wind speed estimates used by teams in Stage 1 compared with 5-minute averages from the 10 m ultrasonic anemometer. Only includes wind speeds for nonzero quantified emissions that passed Stanford and operator quality control. The black dashed line denotes exact 1:1 agreement.

S.4.5.1. Team-specific results

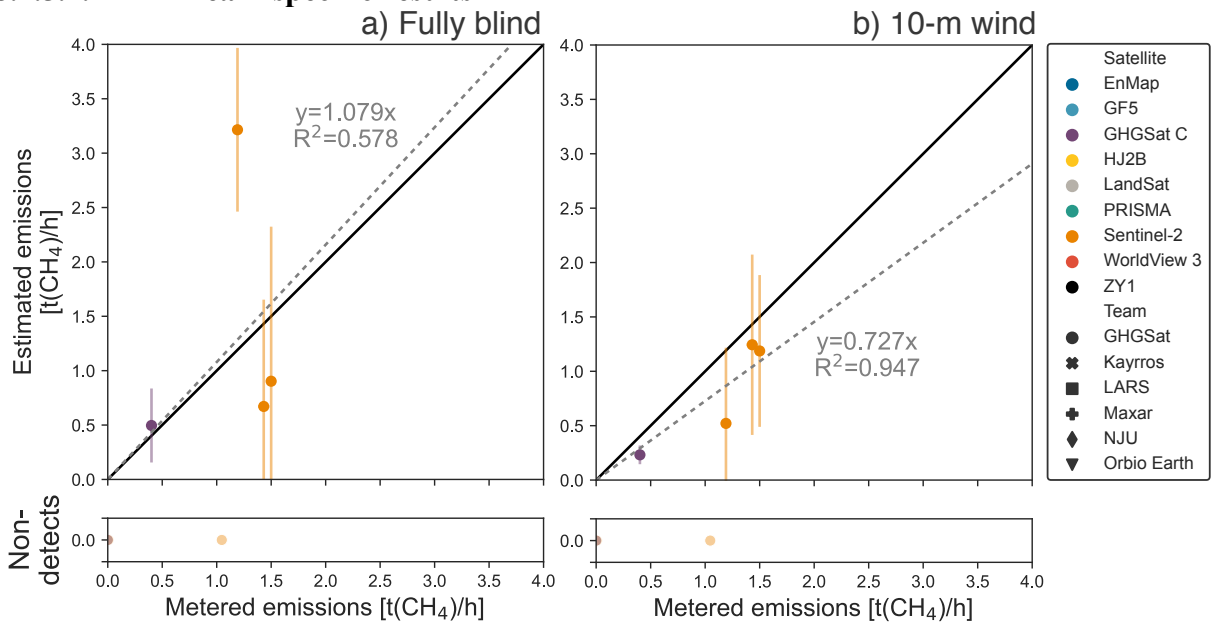


Figure 4. Quantification performance for GHGSat across all satellites, with 95% X and Y confidence intervals. a) presents fully blinded results, while in b) were produced using 10 m in situ wind measurements. The black solid line denotes exact 1:1 agreement. Fitted slope and uncentered R^2 shown for an ordinary least squares fit with the intercept fixed at zero (gray dashed line).

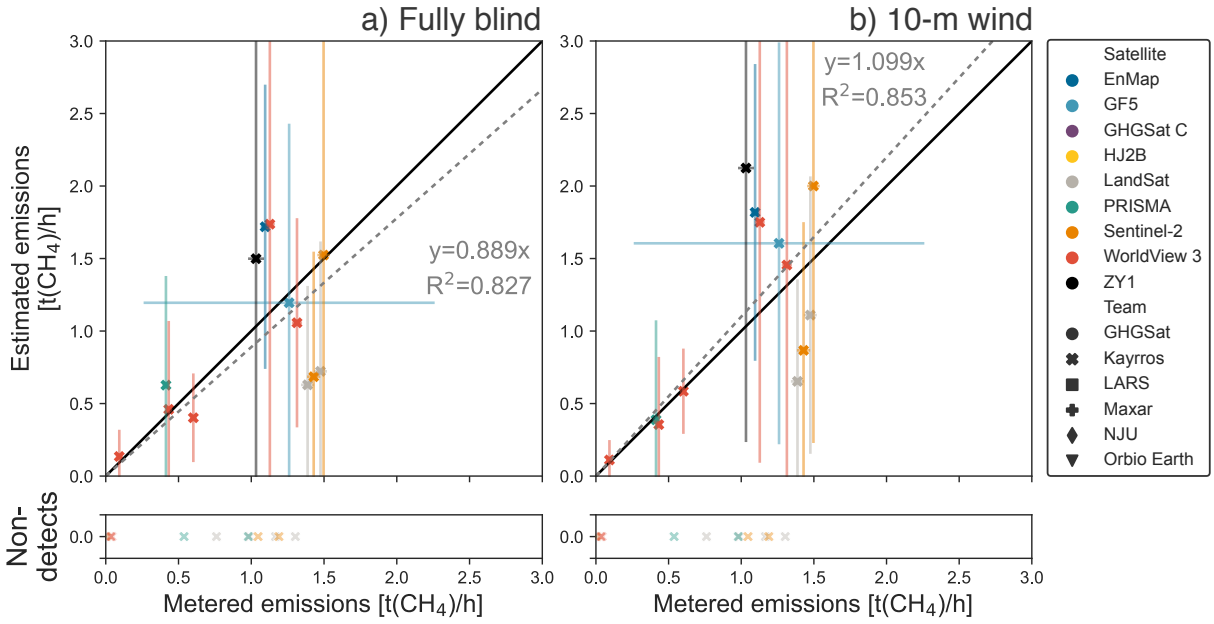


Figure 5. Quantification performance for Kayrros across all satellites, with 95% X and Y confidence intervals. a) presents fully blinded results, while in b) were produced using 10 m in situ wind measurements. The black solid line denotes exact 1:1 agreement. Fitted slope and uncentered R^2 shown for an ordinary least squares fit with the intercept fixed at zero (gray dashed line).

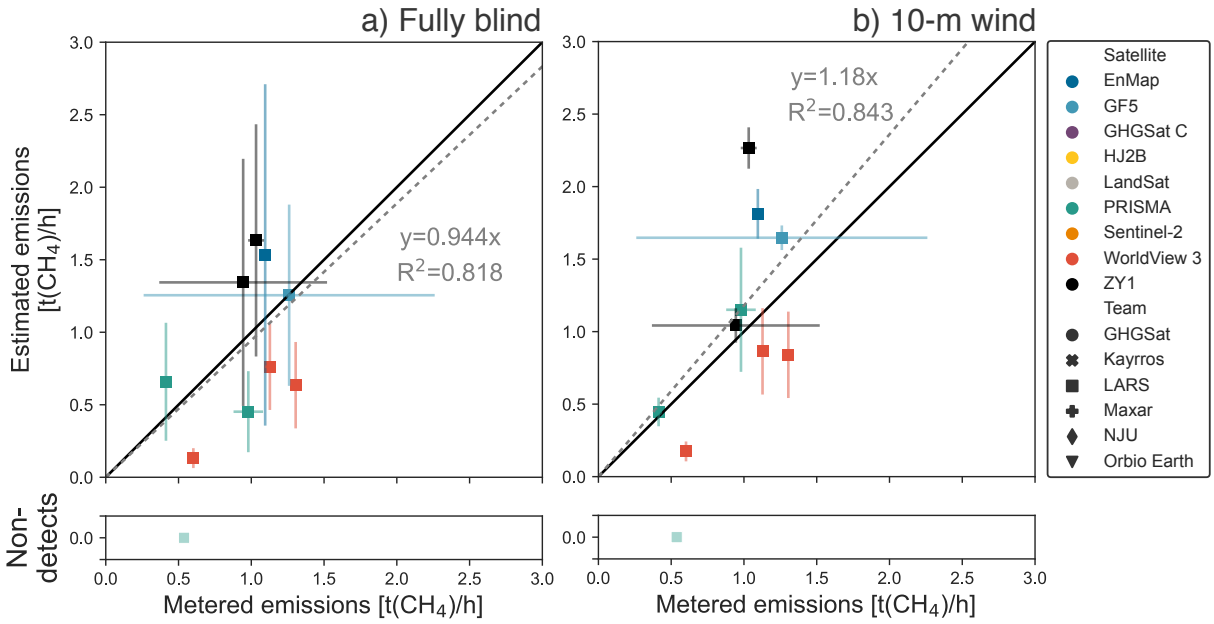


Figure 6. Quantification performance for LARS across all satellites, with 95% X and Y confidence intervals. a) presents fully blinded results, while in b) were produced using 10 m in situ wind measurements. The black solid line denotes exact 1:1 agreement. Fitted slope and uncentered R^2 shown for an ordinary least squares fit with the intercept fixed at zero (gray dashed line). Note that LARS researcher Javier Gorroño submitted Stage 1 WorldView 3 estimates after LARS researcher Javier Roger Juan had received unblinded in situ wind data. Javier Gorroño then submitted Stage 2 WorldView 3 estimates, not included in the main manuscript, after release volumes were unblinded. Although Stanford researchers believe LARS WorldView 3 estimates did not use the ground truth wind data for their Stage 1 estimates or the metered volumes for their Stage 2 estimates, we include them only in the SI to maintain strict adherence to our experimental design.

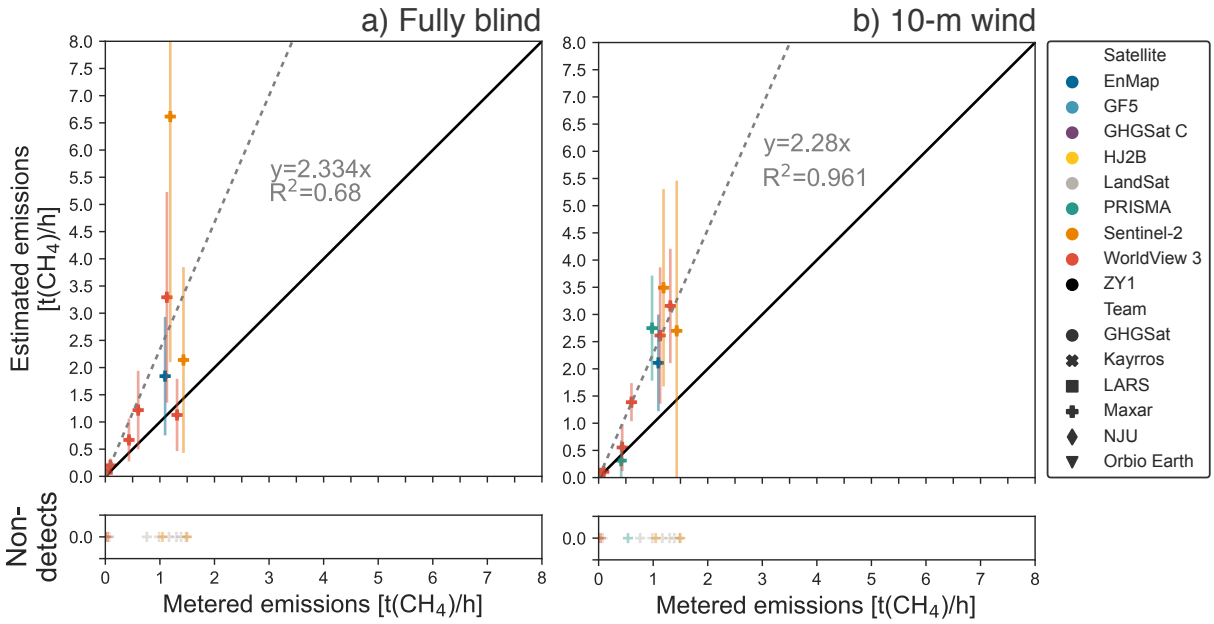


Figure 7. Quantification performance for Maxar across all satellites, with 95% X and Y confidence intervals. a) presents fully blinded results, while in b) were produced using 10 m in situ wind measurements. The black solid line denotes exact 1:1 agreement. Fitted slope and uncentered R^2 shown for an ordinary least squares fit with the intercept fixed at zero (gray dashed line). Note that Maxar concluded after results were unblinded that their results were high by a factor of two due to use of a deprecated spectral library [2].

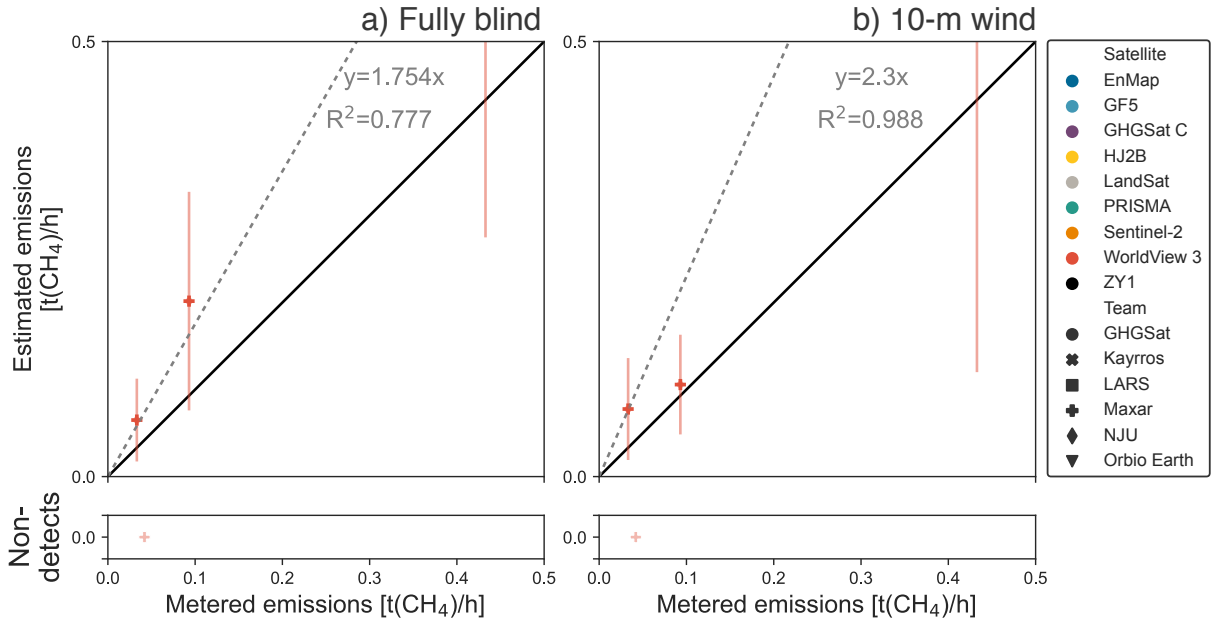


Figure 8 Quantification performance for Maxar for WorldView-3 showing only 0.5 t/h or less. Error bars represent 95% X and Y confidence intervals. a) presents fully blinded results, while in b) were produced using 10 m in situ wind measurements. The black solid line denotes exact 1:1 agreement. Fitted slope and uncentered R^2 shown for an ordinary least squares fit with the intercept fixed at zero (gray dashed line).

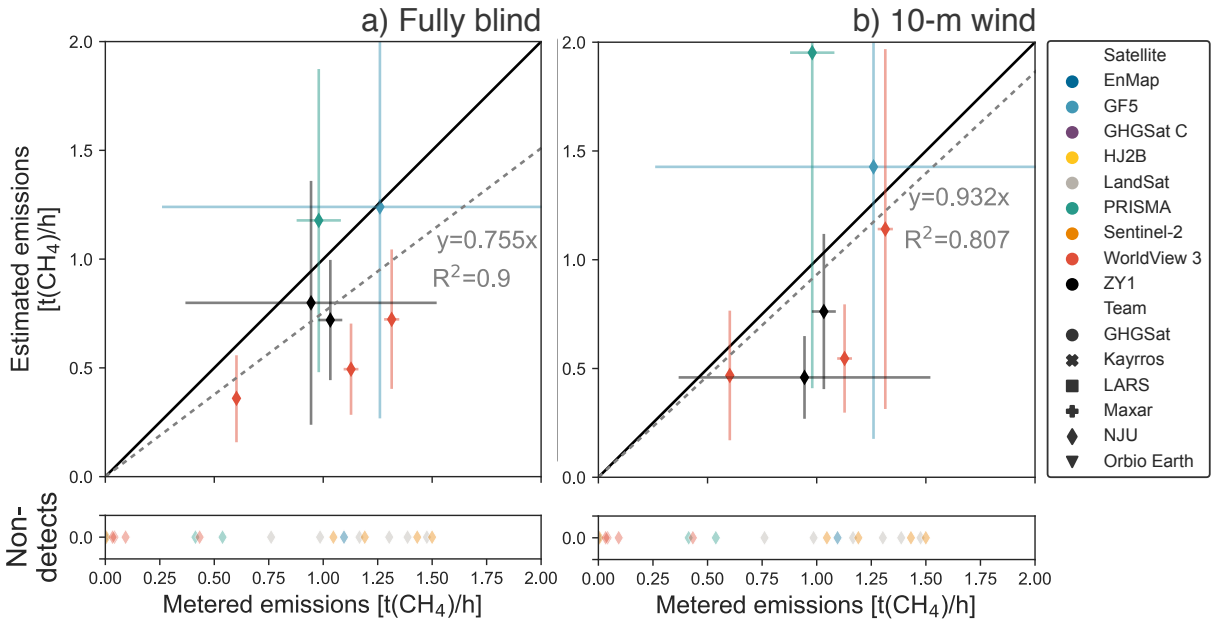


Figure 9. Quantification performance for NJU across all satellites, with 95% X and Y confidence intervals. a) presents fully blinded results, while in b) were produced using 10 m in situ wind measurements. The black solid line denotes exact 1:1 agreement. Fitted slope and uncentered R^2 shown for an ordinary least squares fit with the intercept fixed at zero (gray dashed line).

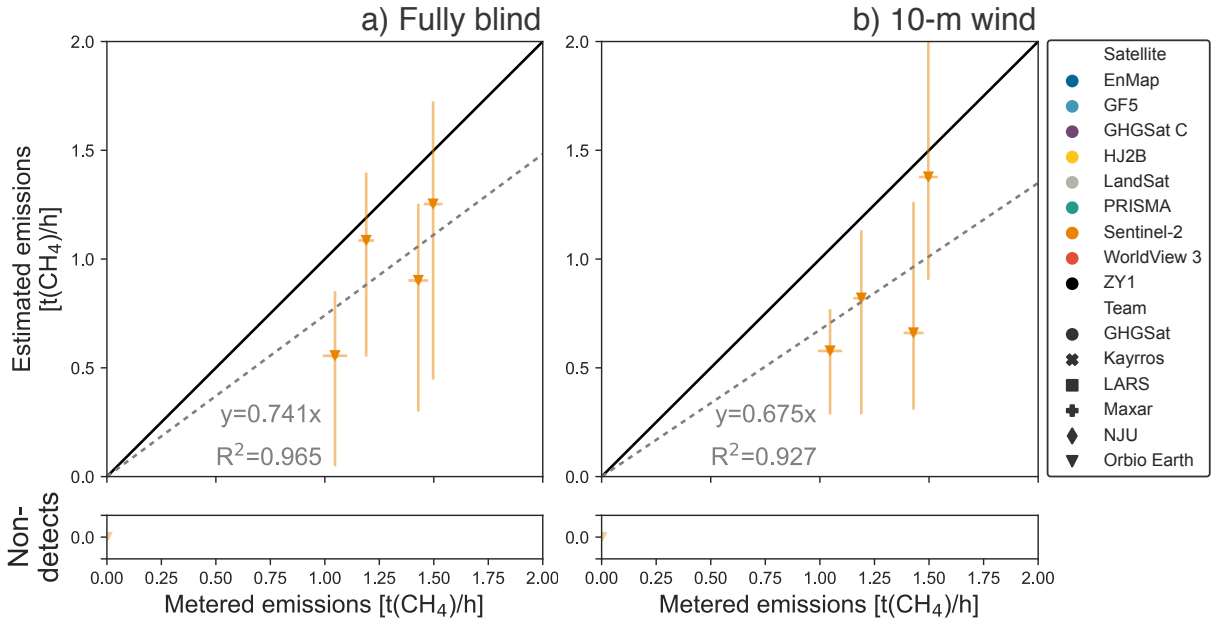


Figure 10. Quantification performance for Orbio Earth across all satellites, with 95% X and Y confidence intervals. a) presents fully blinded results, while in b) were produced using 10 m in situ wind measurements. The black solid line denotes exact 1:1 agreement. Fitted slope and uncentered R^2 shown for an ordinary least squares fit with the intercept fixed at zero (gray dashed line).

S.4.5.2. Satellite-specific parity charts

Recall that Maxar concluded after results were unblinded that their results were high by a factor of two due to use of a deprecated spectral library [2]. This would add upward average bias to all below linear fits that include Maxar estimates.

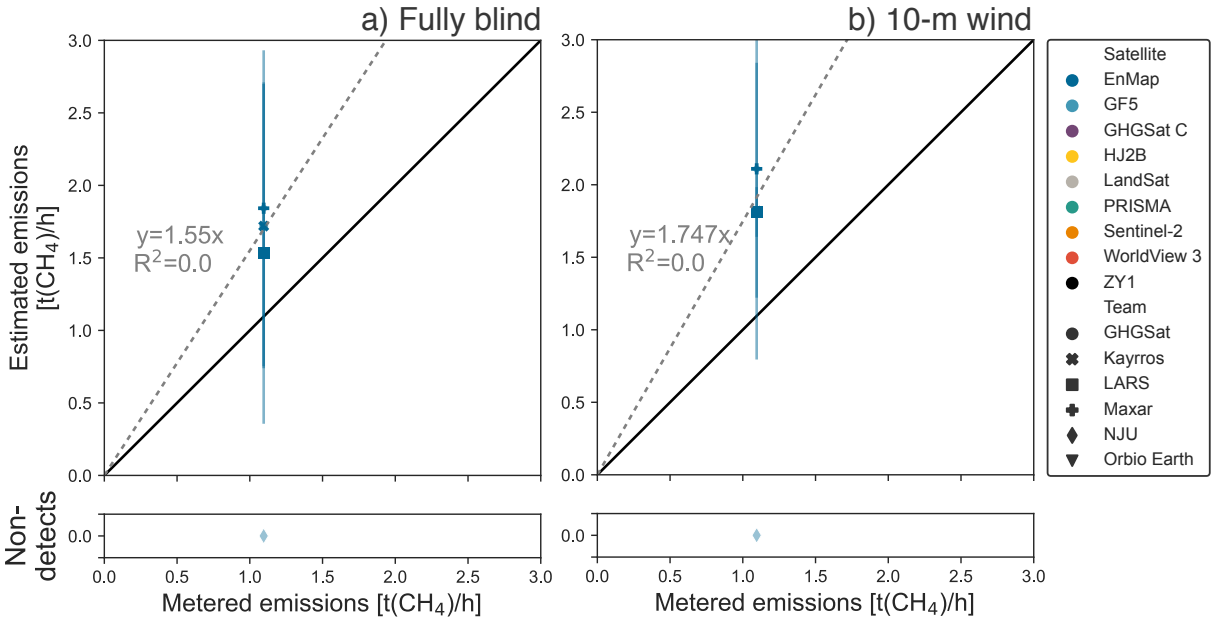


Figure 11. Quantification performance for EnMAP across all teams, with 95% X and Y confidence intervals. The black solid line denotes exact 1:1 agreement. Fitted slope and uncentered R^2 shown for an ordinary least squares fit with the intercept fixed at zero (gray dashed line).

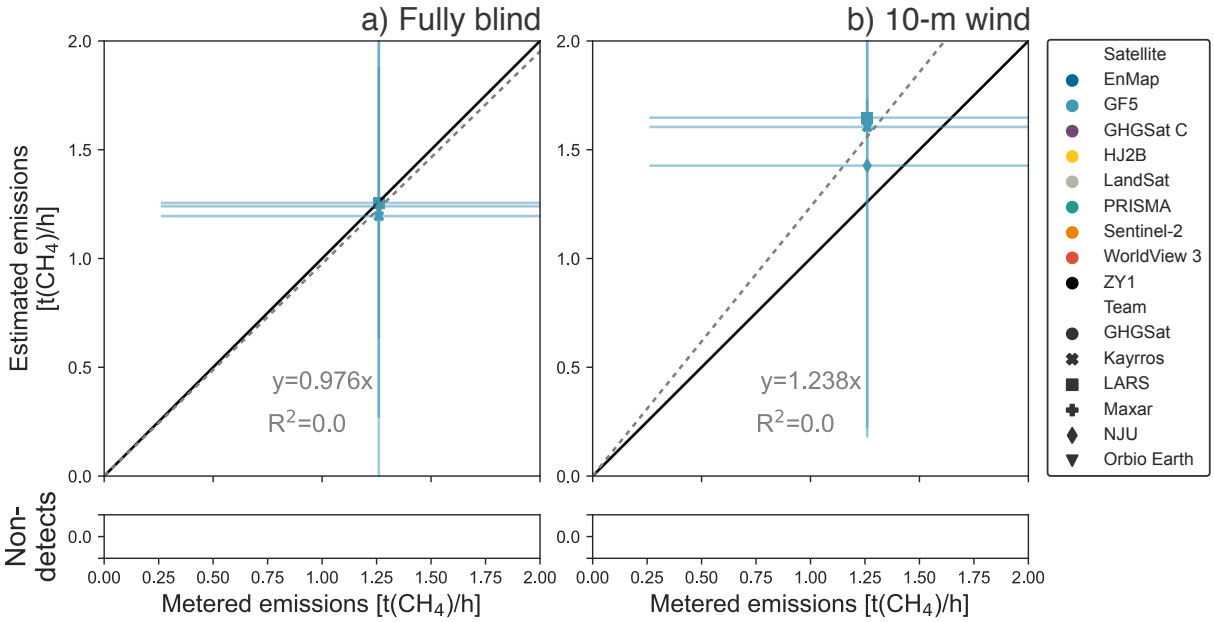


Figure 12. Quantification performance for GF5 across all teams, with 95% X and Y confidence intervals. The black solid line denotes exact 1:1 agreement. Fitted slope and uncentered R^2 shown for an ordinary least squares fit with the intercept fixed at zero (gray dashed line). R^2 is zero here because all points have an identical x-coordinate.

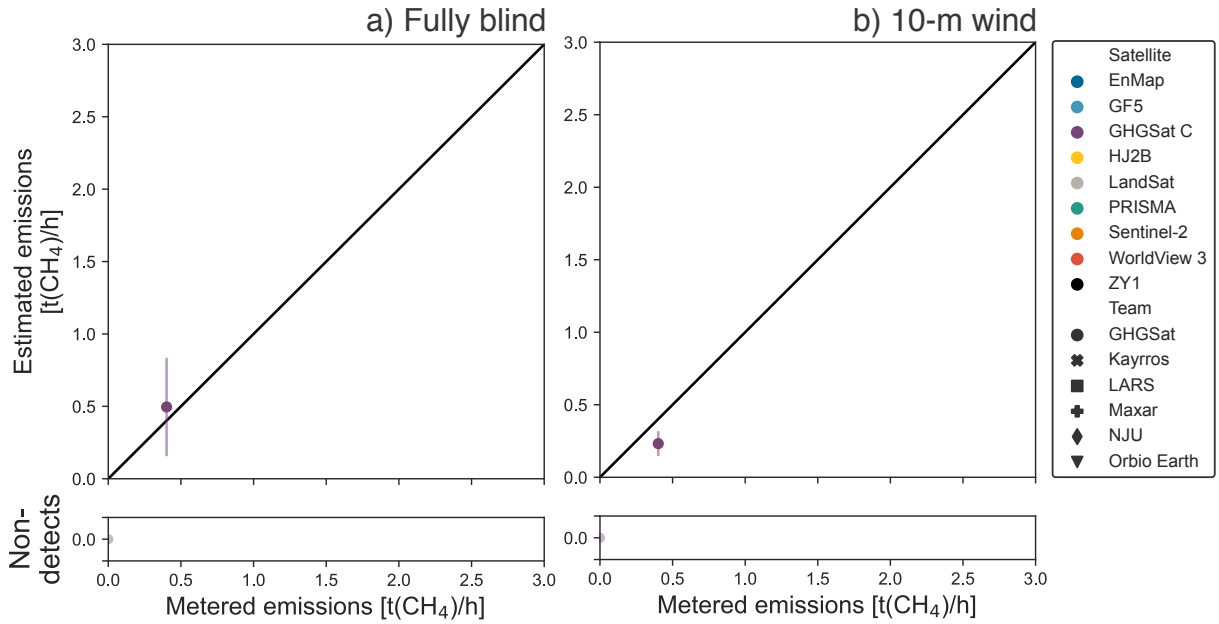


Figure 13. Quantification performance for GHGSat C across all teams, with 95% X and Y confidence intervals. The black solid line denotes exact 1:1 agreement.

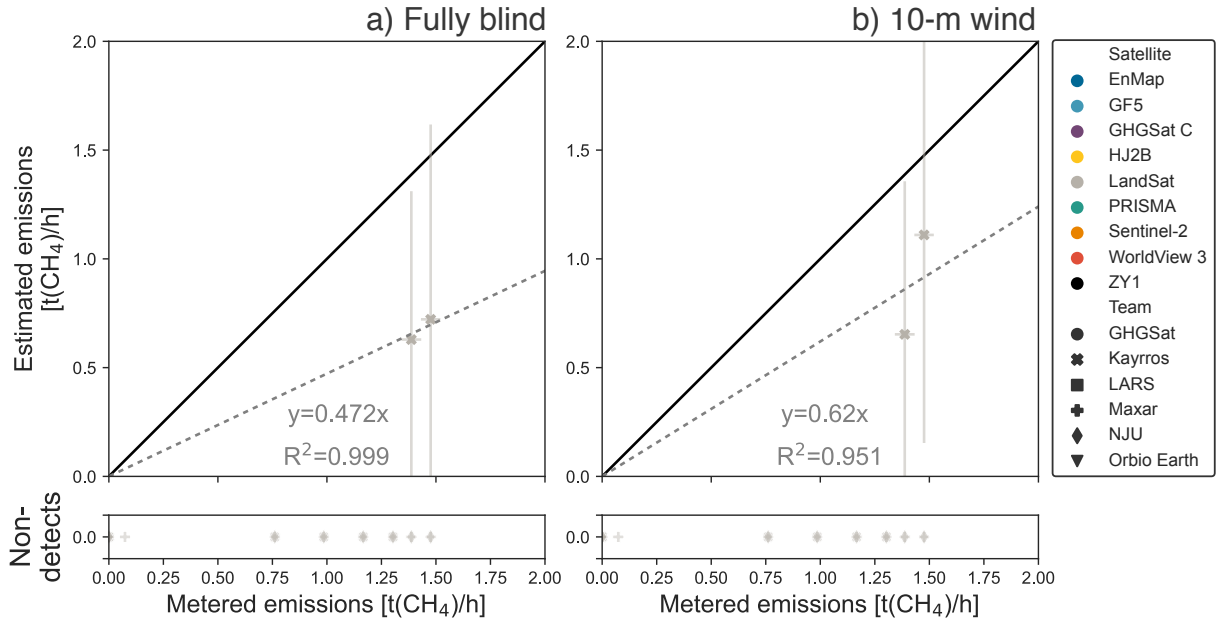


Figure 14. Quantification performance for LandSat 8/9 across all teams, with 95% X and Y confidence intervals. The black solid line denotes exact 1:1 agreement. Fitted slope and uncentered R^2 shown for an ordinary least squares fit with the intercept fixed at zero (gray dashed line).

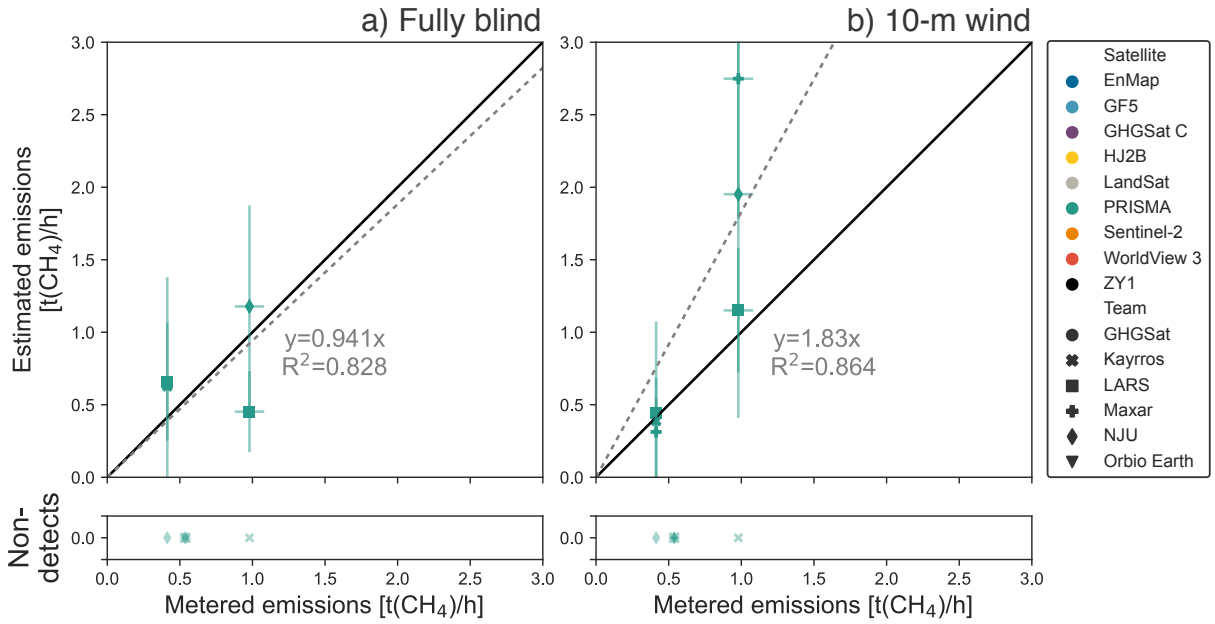


Figure 15. Quantification performance for PRISMA across all teams, with 95% X and Y confidence intervals. The black solid line denotes exact 1:1 agreement. Fitted slope and uncentered R^2 shown for an ordinary least squares fit with the intercept fixed at zero (gray dashed line).

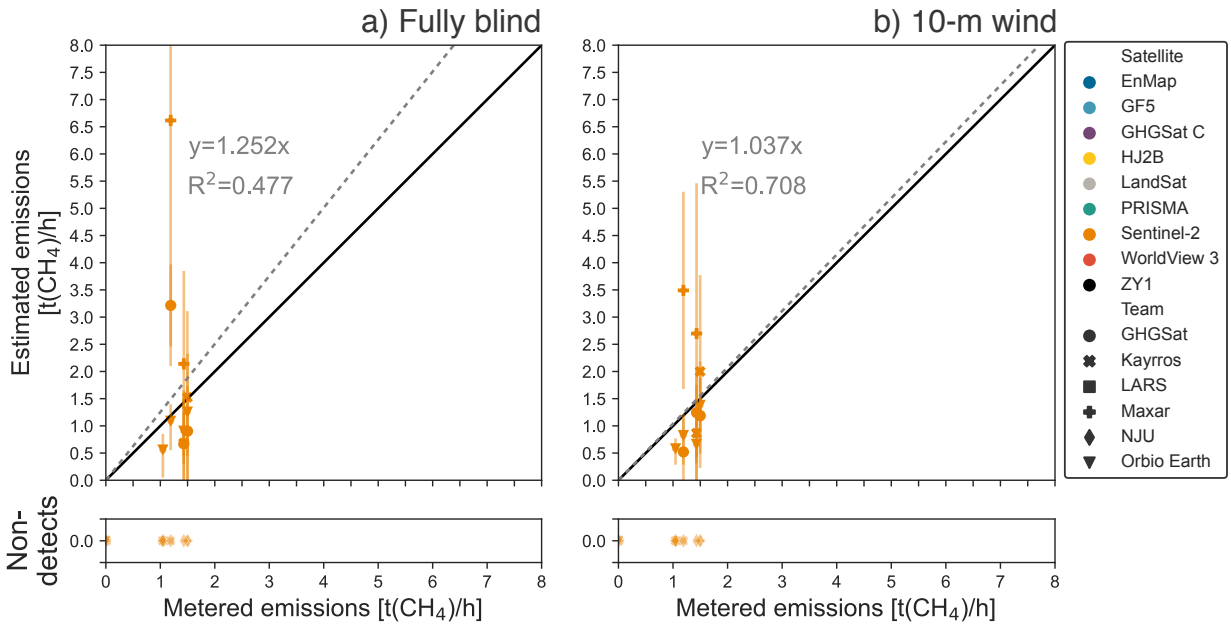


Figure 16. Quantification performance for Sentinel-2 across all teams, with 95% X and Y confidence intervals. The black dashed line denotes exact 1:1 agreement. Fitted slope and uncentered R^2 shown for an ordinary least squares fit with the intercept fixed at zero.

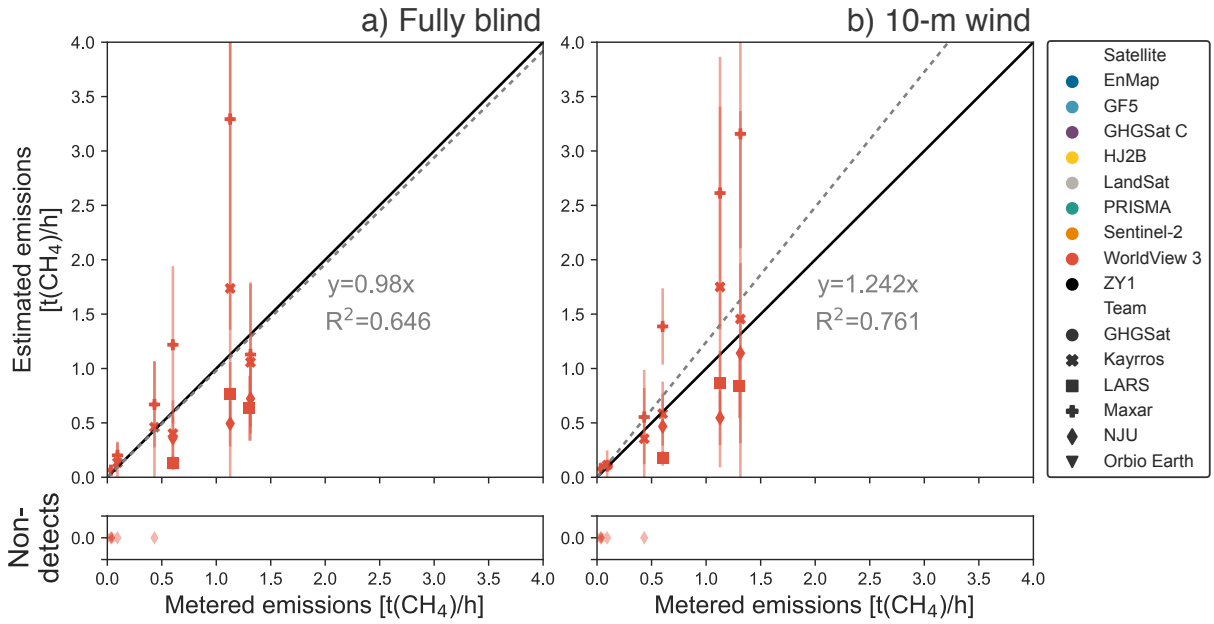


Figure 17. Quantification performance for WorldView-3 across all teams, with 95% X and Y confidence intervals. The black solid line denotes exact 1:1 agreement. Fitted slope and uncentered R^2 shown for an ordinary least squares fit with the intercept fixed at zero (gray dashed line). Note that LARS researcher Javier Gorroño submitted Stage 1 WorldView 3 estimates after LARS researcher Javier Roger Juan had received unblinded in situ wind data. Javier Gorroño then submitted Stage 2 WorldView 3 estimates, not included in the main manuscript, after release volumes were unblinded. Although Stanford researchers believe LARS WorldView 3 estimates did not use the ground truth wind data for their Stage 1 estimates or the metered volumes for their Stage 2 estimates, we include them only in the SI to maintain strict adherence to our experimental design.

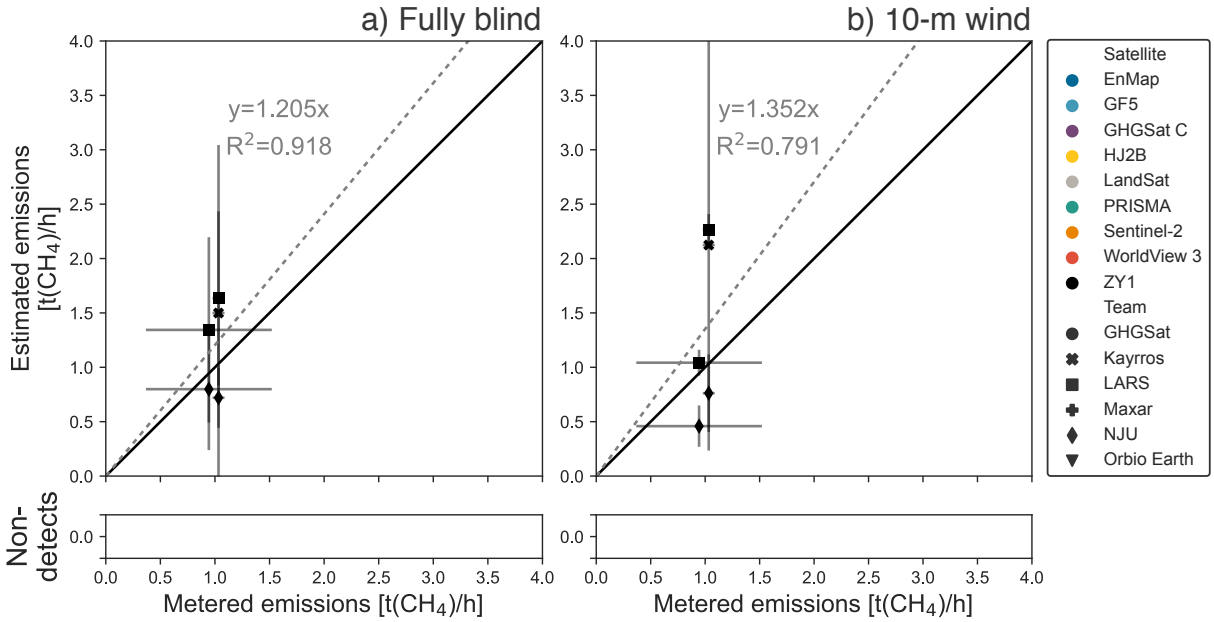


Figure 18. Quantification performance for ZY1 across all teams, with 95% X and Y confidence intervals. The black solid line denotes exact 1:1 agreement. Fitted slope and uncentered R^2 shown for an ordinary least squares fit with the intercept fixed at zero (gray dashed line). Includes estimates submitted for the October 20th release, which was filtered in the main analysis due to a system malfunction. See the SI, Section S3.3 for further discussion of this data point.

S.4.6. Retrieval images

The following are masked and unmasked methane retrieval images from each of the participating teams. Masking refers to the process of identifying a methane plume and differentiating its outline from its surroundings. Submitting these images was optional, and not all teams submitted all images for retrievals they conducted. Note the level of variability in unmasked scenes across teams operating with precisely the same spectral data.

S.4.6.1. EnMAP

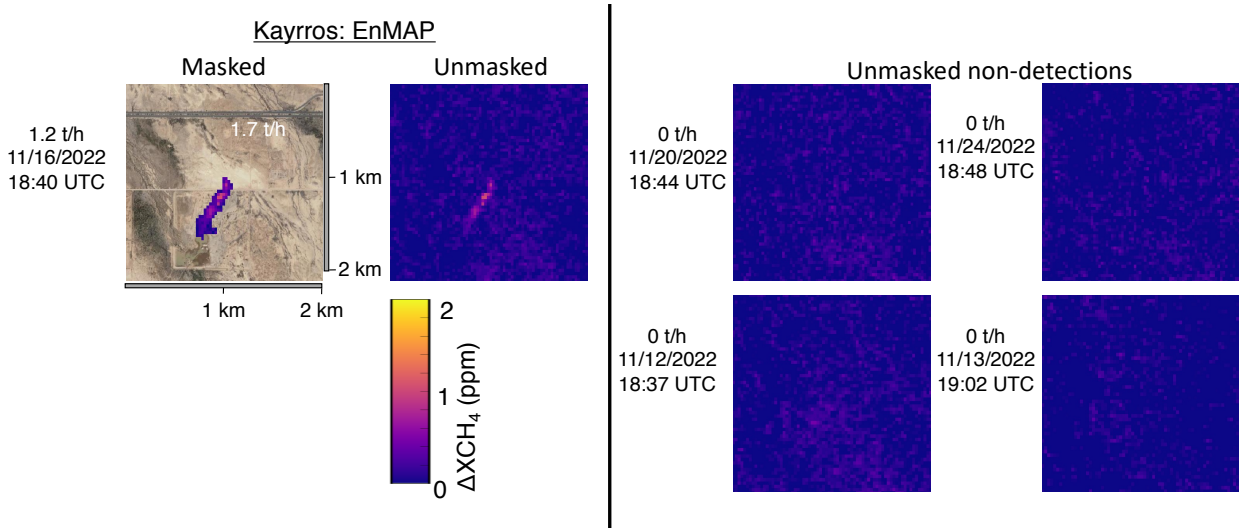


Figure 19. Provided masked and unmasked methane enhancement estimates from Kayrros for EnMAP retrievals. Surface imagery © 2023 Google Earth, CNES/Airbus, Maxar Technologies, USDA/FPAC/GEO.

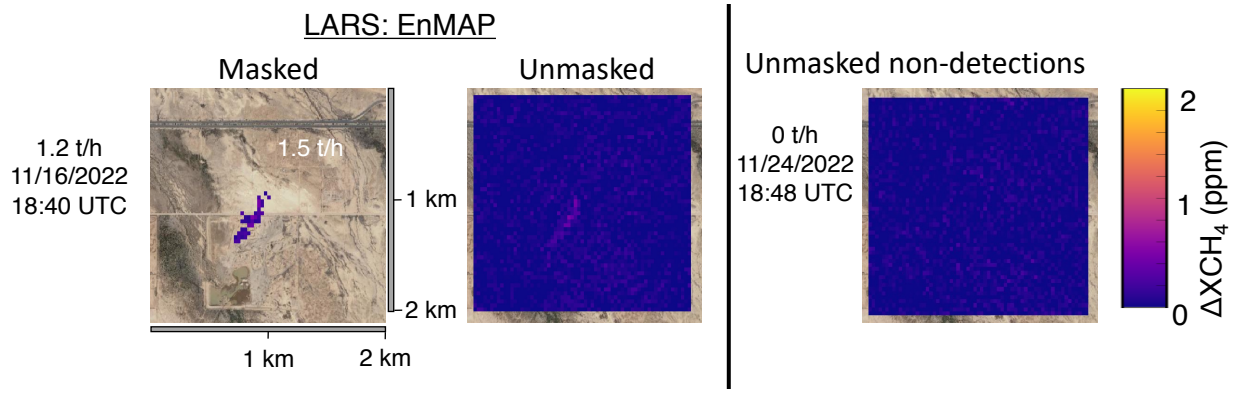


Figure 20. Provided masked and unmasked methane enhancement estimates from LARS for EnMAP retrievals. Surface imagery © 2023 Google Earth, CNES/Airbus, Maxar Technologies, USDA/FPAC/GEO.

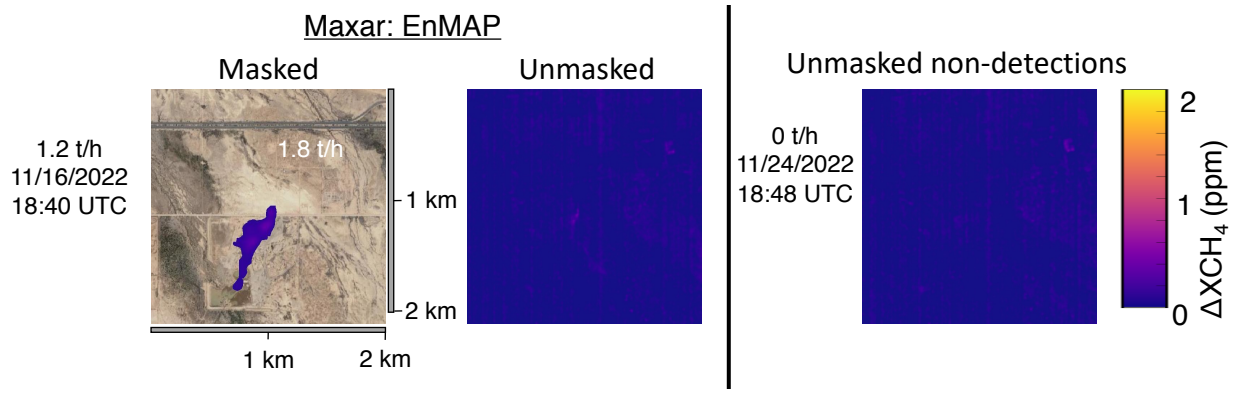


Figure 21. Provided masked and unmasked methane enhancement estimates from Maxar for EnMAP retrievals. Surface imagery © 2023 Google Earth, CNES/Airbus, Maxar Technologies, USDA/FPAC/GEO.

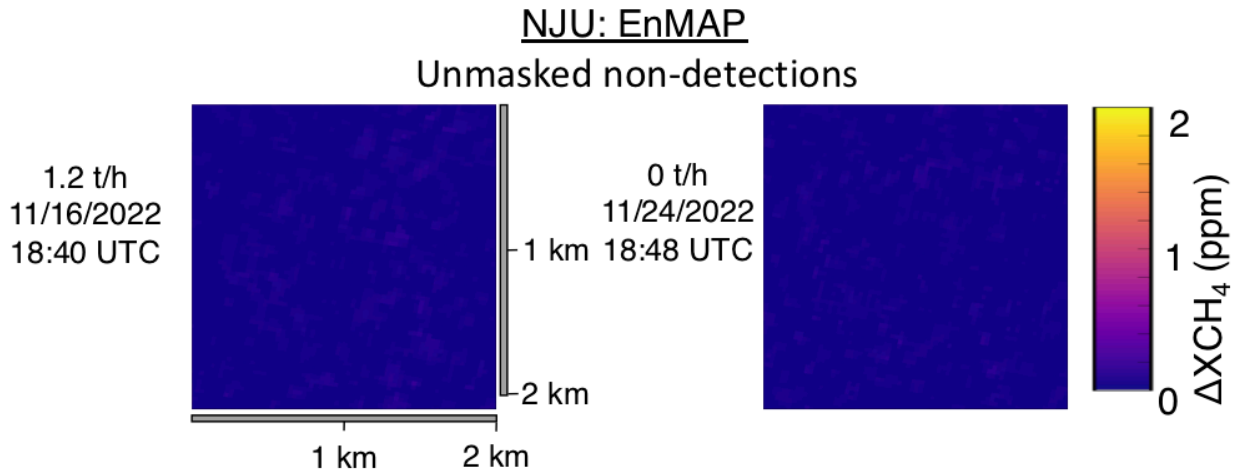


Figure 22. Provided masked and unmasked methane enhancement estimates from NJU for EnMAP retrievals. Surface imagery © 2023 Google Earth, CNES/Airbus, Maxar Technologies, USDA/FPAC/GEO.

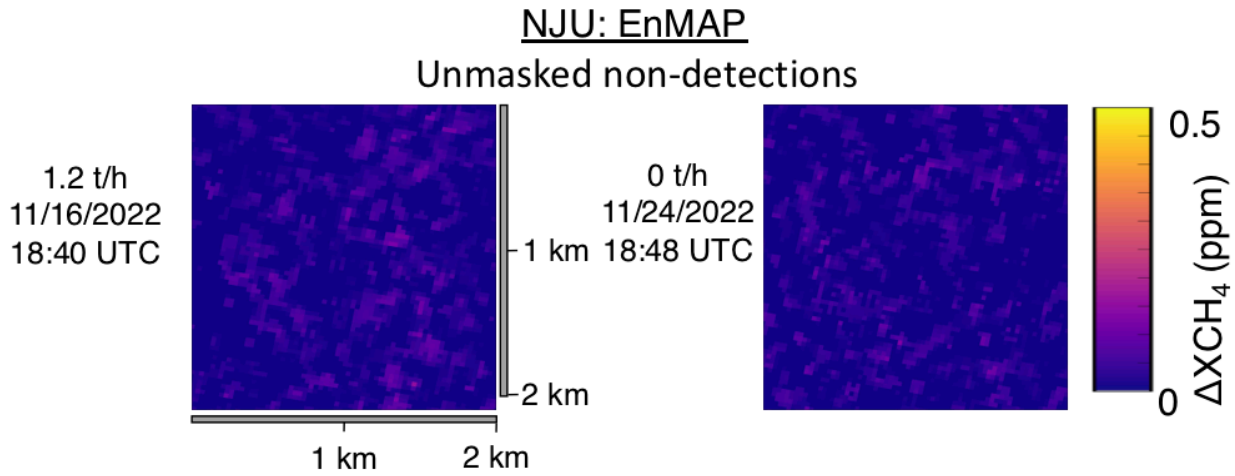


Figure 23. Custom-PPM scale, provided masked and unmasked methane enhancement estimates from NJU for EnMAP retrievals. Surface imagery © 2023 Google Earth, CNES/Airbus, Maxar Technologies, USDA/FPAC/GEO.

S.4.6.2. Gaofen 5 (GF5)

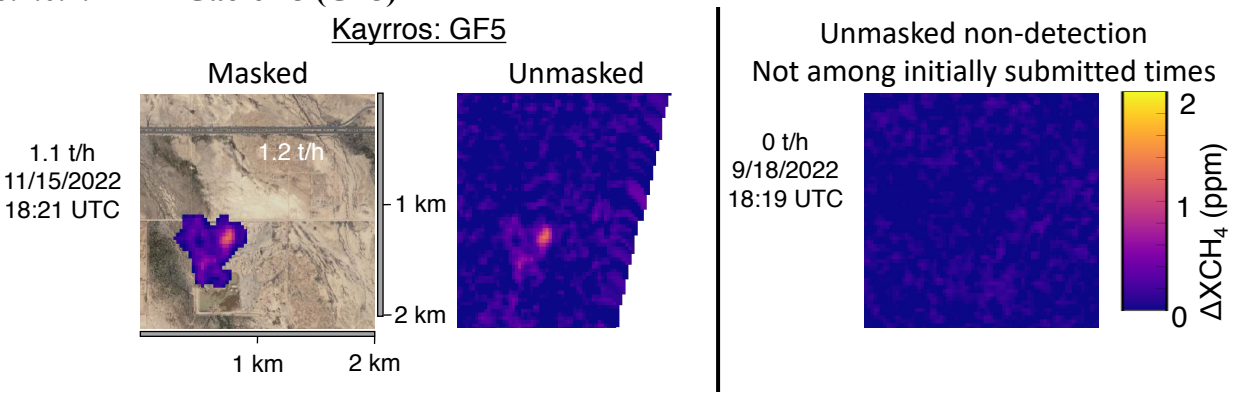


Figure 24. Provided masked and unmasked methane enhancement estimates from Kayrros for GF5 retrievals. Surface imagery © 2023 Google Earth, CNES/Airbus, Maxar Technologies, USDA/FPAC/GEO.

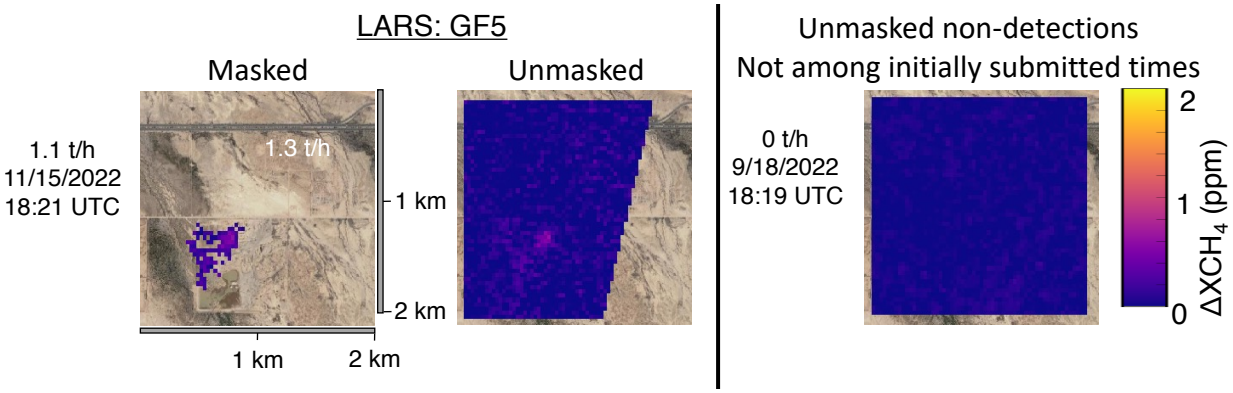


Figure 25. Provided masked and unmasked methane enhancement estimates from LARS for GF5 retrievals. Surface imagery © 2023 Google Earth, CNES/Airbus, Maxar Technologies, USDA/FPAC/GEO.

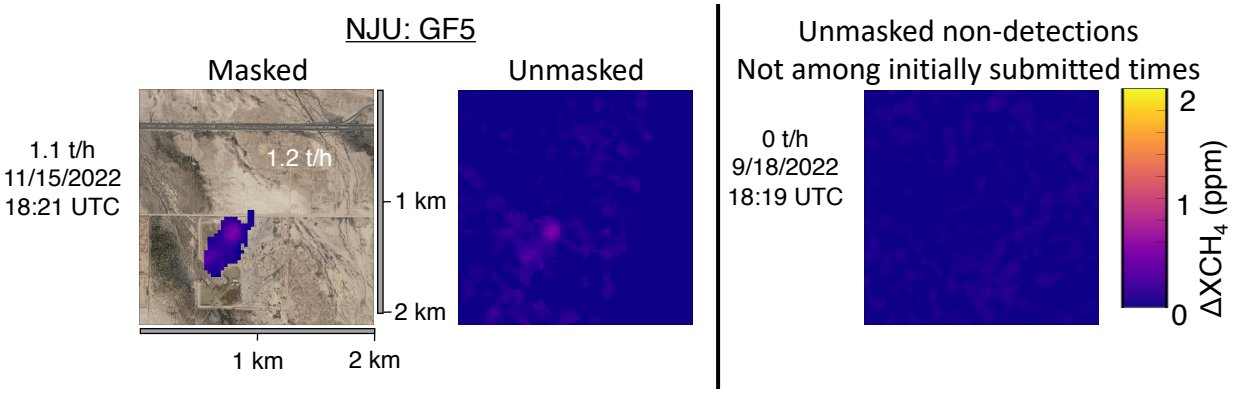


Figure 26. Provided masked and unmasked methane enhancement estimates from NJU for GF5 retrievals. Surface imagery © 2023 Google Earth, CNES/Airbus, Maxar Technologies, USDA/FPAC/GEO.

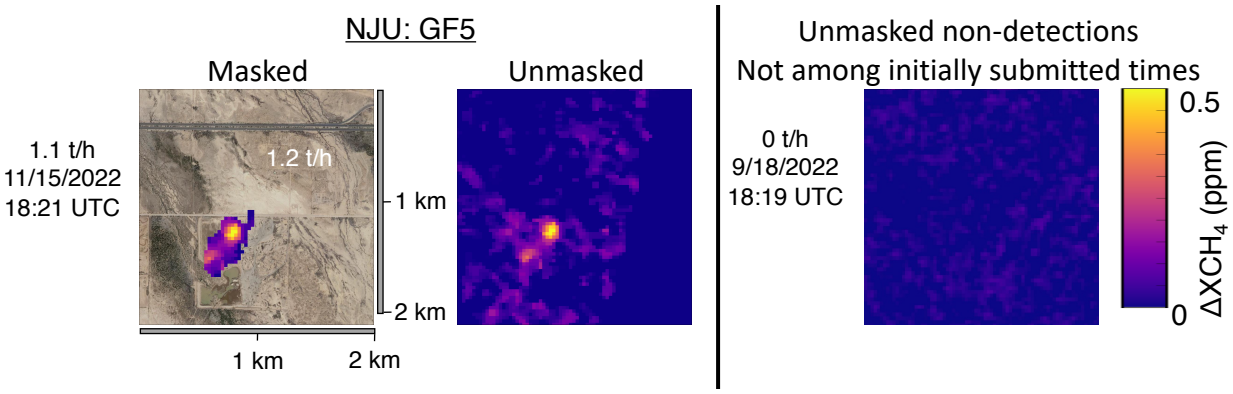


Figure 27. Custom-PPM scale, provided masked and unmasked methane enhancement estimates from NJU for GF5 retrievals. Surface imagery © 2023 Google Earth, CNES/Airbus, Maxar Technologies, USDA/FPAC/GEO.

S.4.6.3. GHGSat C

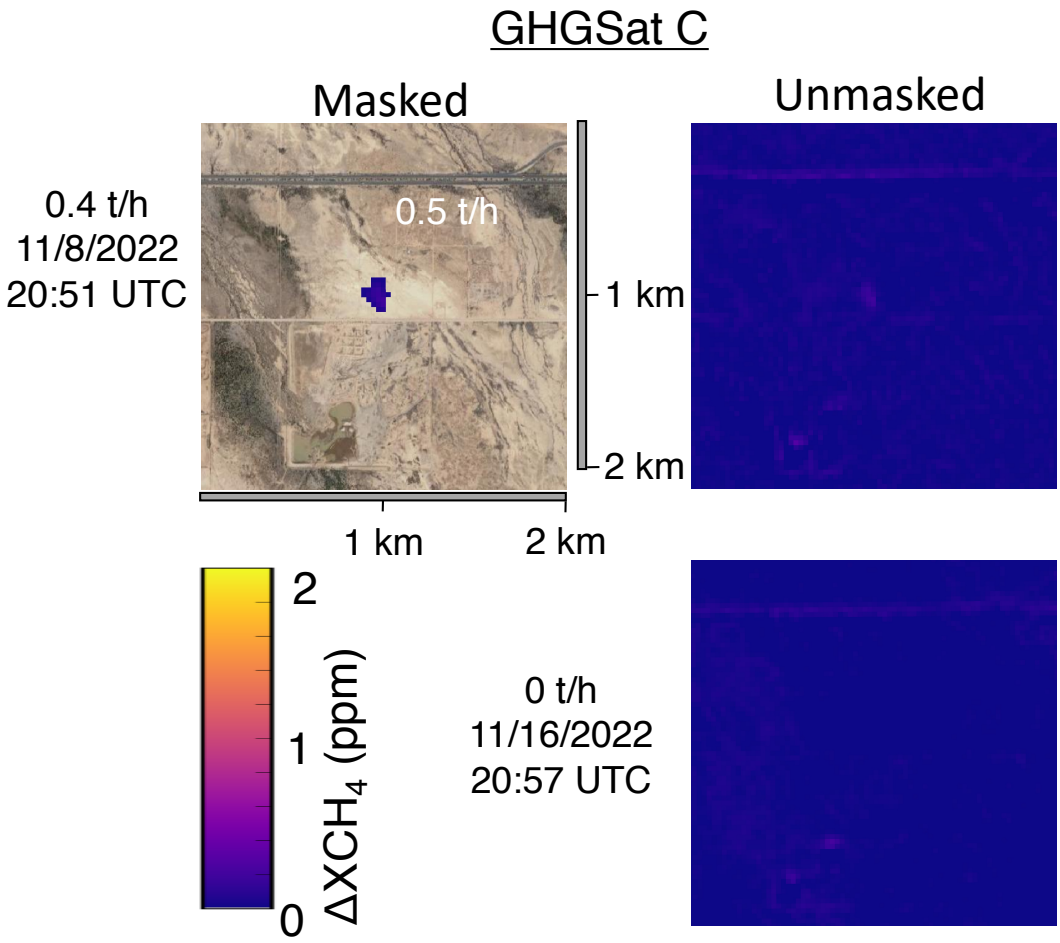


Figure 28. Provided masked and unmasked methane enhancement estimates from GHGSat for GHGSat-C retrievals. Surface imagery © 2023 Google Earth, CNES/Airbus, Maxar Technologies, USDA/FPAC/GEO.

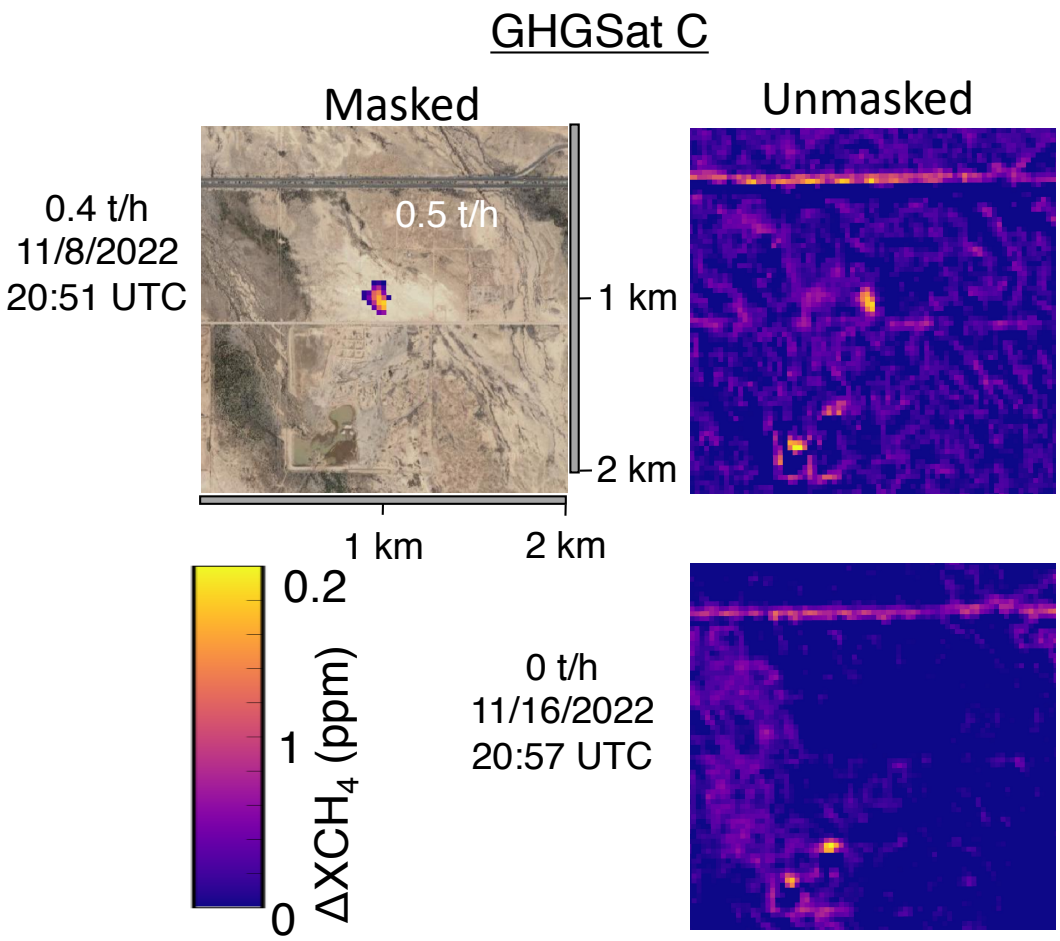


Figure 29. Provided masked and unmasked methane enhancement estimates from GHGSat for GHGSat-C retrievals. Uses a maximum ppm scale value of 0.2 ppm instead of the 2 ppm used for intercomparison across technologies. Surface imagery © 2023 Google Earth, CNES/Airbus, Maxar Technologies, USDA/FPAC/GEO.

S.4.6.4. Huanjing 2B (HJ2B)

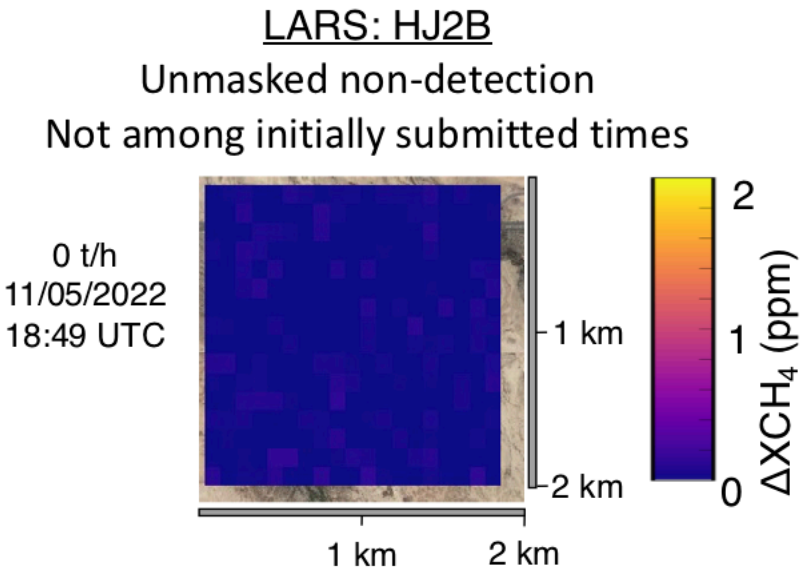


Figure 30. Provided masked and unmasked methane enhancement estimates from LARS for the HJ2B retrieval. Surface imagery © 2023 Google Earth, CNES/Airbus, Maxar Technologies, USDA/FPAC/GEO.

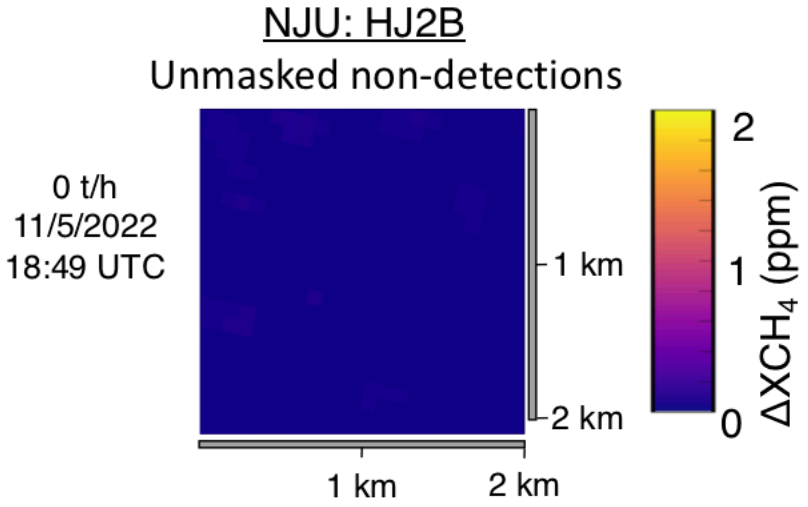


Figure 31. Provided masked and unmasked methane enhancement estimates from LARS for the HJ2B retrieval. Surface imagery © 2023 Google Earth, CNES/Airbus, Maxar Technologies, USDA/FPAC/GEO.

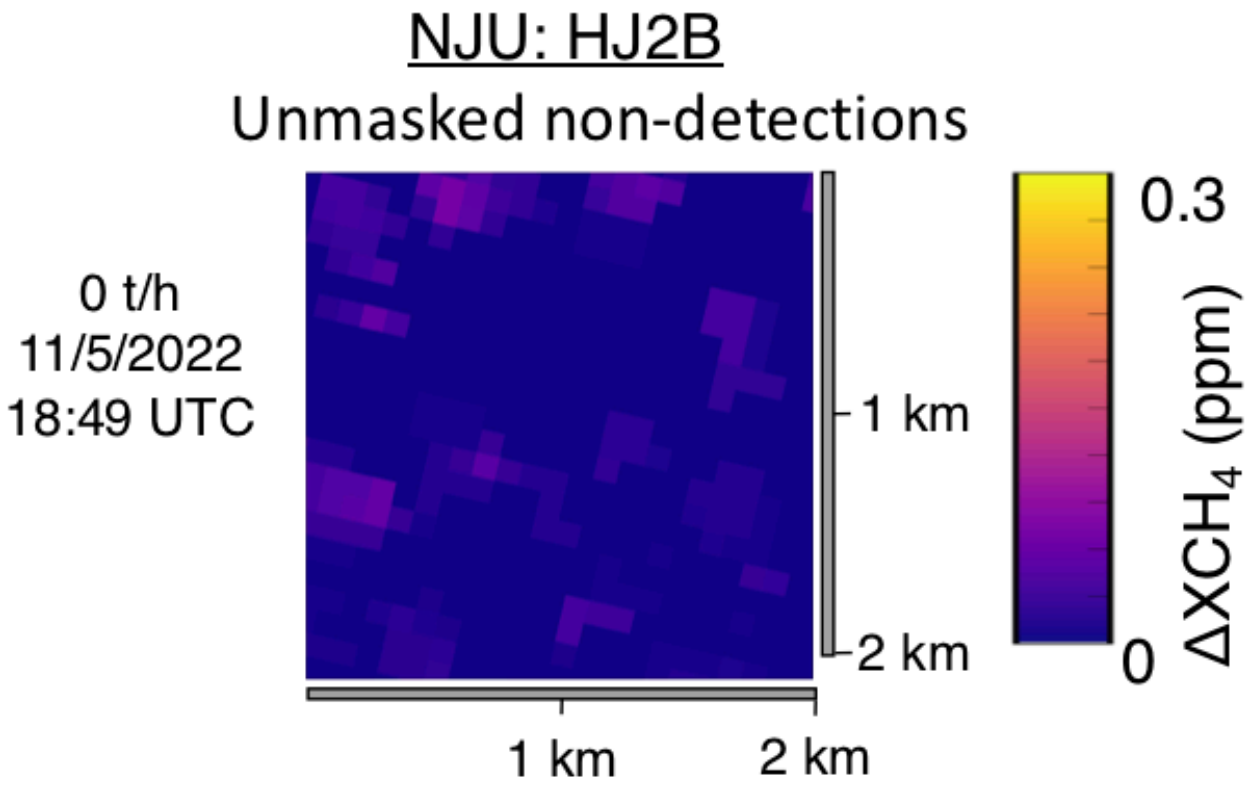


Figure 32. Custom-ppm scale, provided masked and unmasked methane enhancement estimates from LARS for the HJ2B retrieval. Surface imagery © 2023 Google Earth, CNES/Airbus, Maxar Technologies, USDA/FPAC/GEO.

S.4.6.5. LandSat

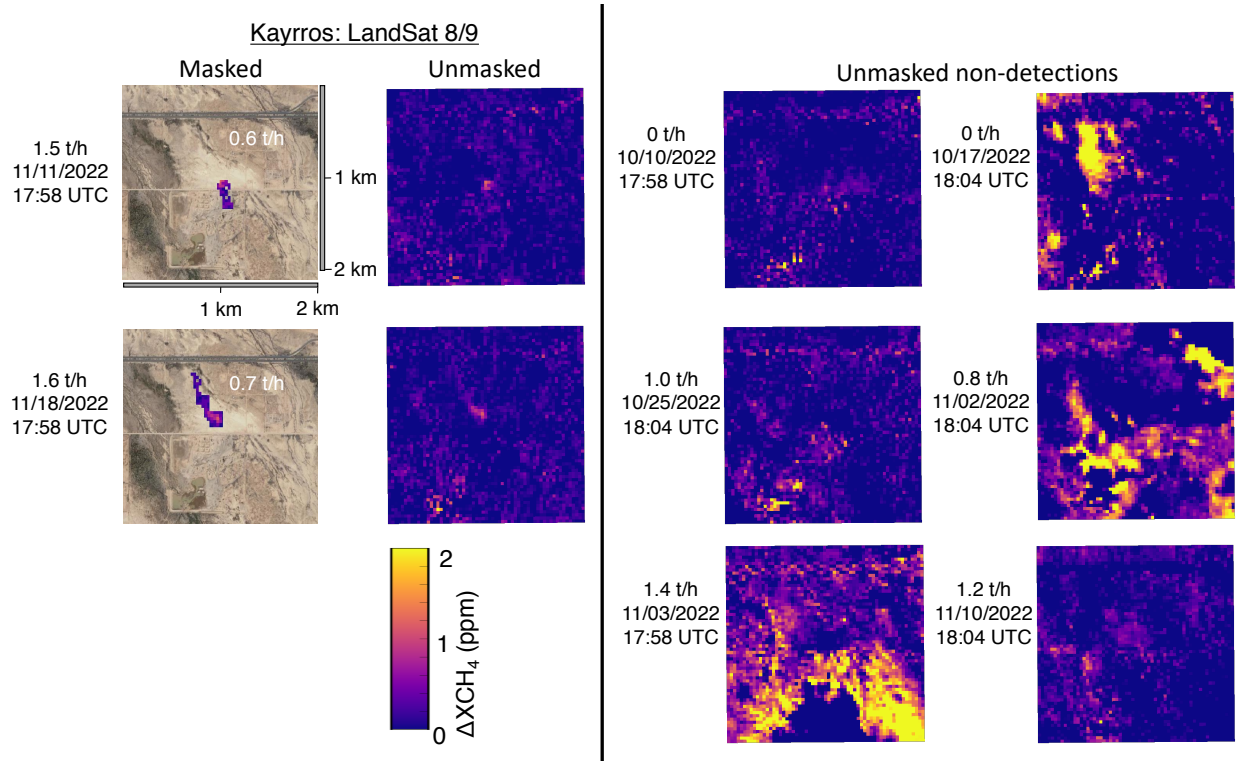


Figure 33. Provided masked and unmasked methane enhancement estimates from Kayrros for LandSat 8/9 retrievals. Surface imagery © 2023 Google Earth, CNES/Airbus, Maxar Technologies, USDA/FPAC/GEO.

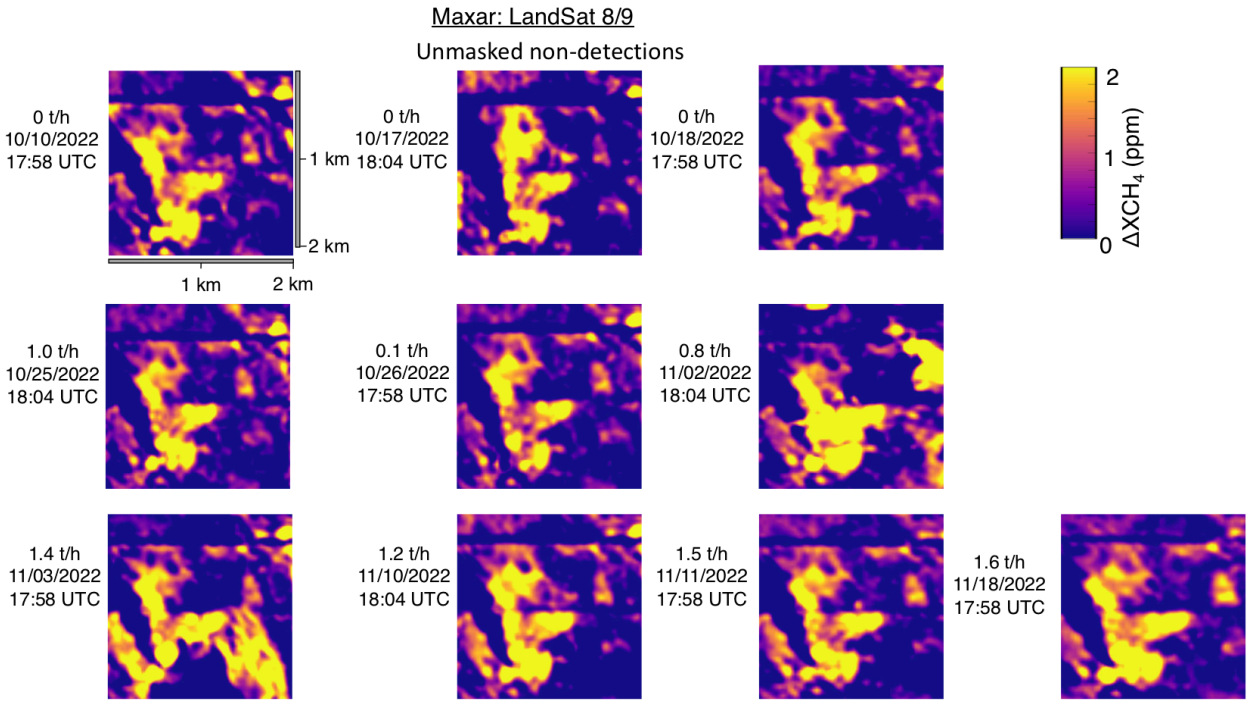


Figure 34. Provided masked and unmasked methane enhancement estimates from Maxar for LandSat 8/9 retrievals. All retrievals were reported as non-detections. Surface imagery © 2023 Google Earth, CNES/Airbus, Maxar Technologies, USDA/FPAC/GEO.

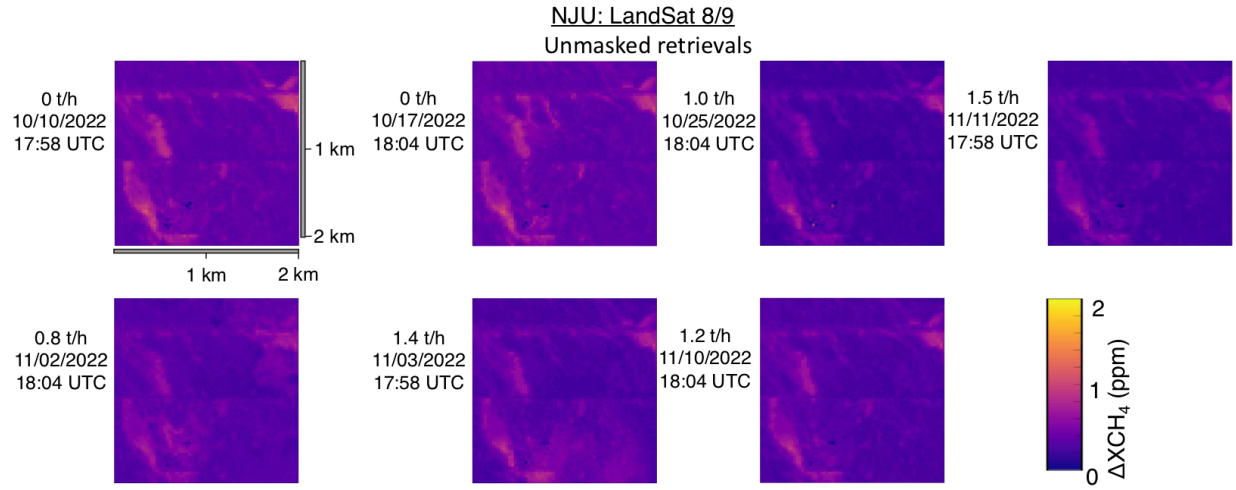


Figure 35. Provided masked and unmasked methane enhancement estimates from NJU for LandSat 8/9 retrievals. All retrievals were reported as non-detections. Surface imagery © 2023 Google Earth, CNES/Airbus, Maxar Technologies, USDA/FPAC/GEO.

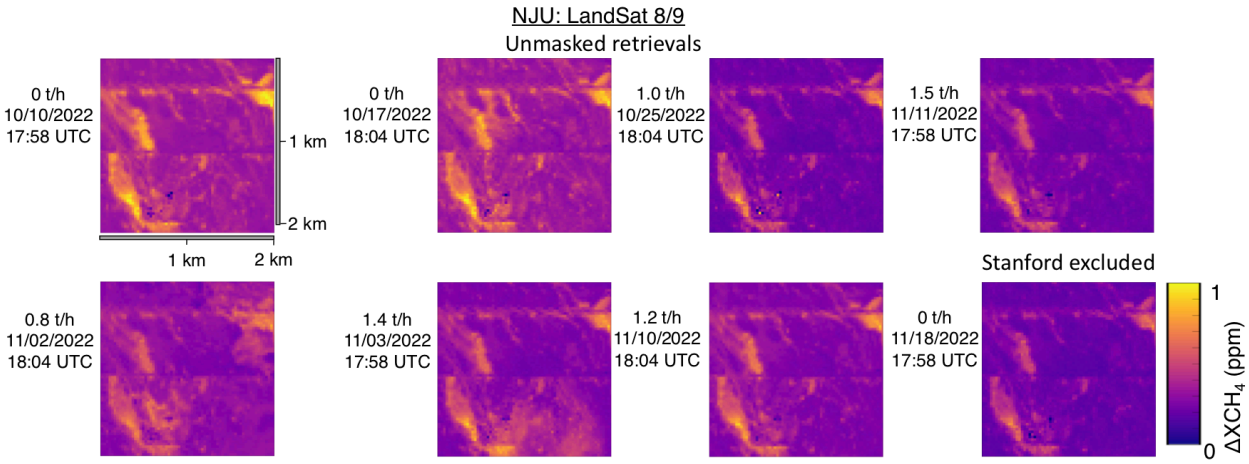


Figure 36. Custom-PPM scale, provided masked and unmasked methane enhancement estimates from NJU for LandSat 8/9 retrievals. All retrievals were reported as non-detections. Surface imagery © 2023 Google Earth, CNES/Airbus, Maxar Technologies, USDA/FPAC/GEO.

S.4.6.6. PRISMA

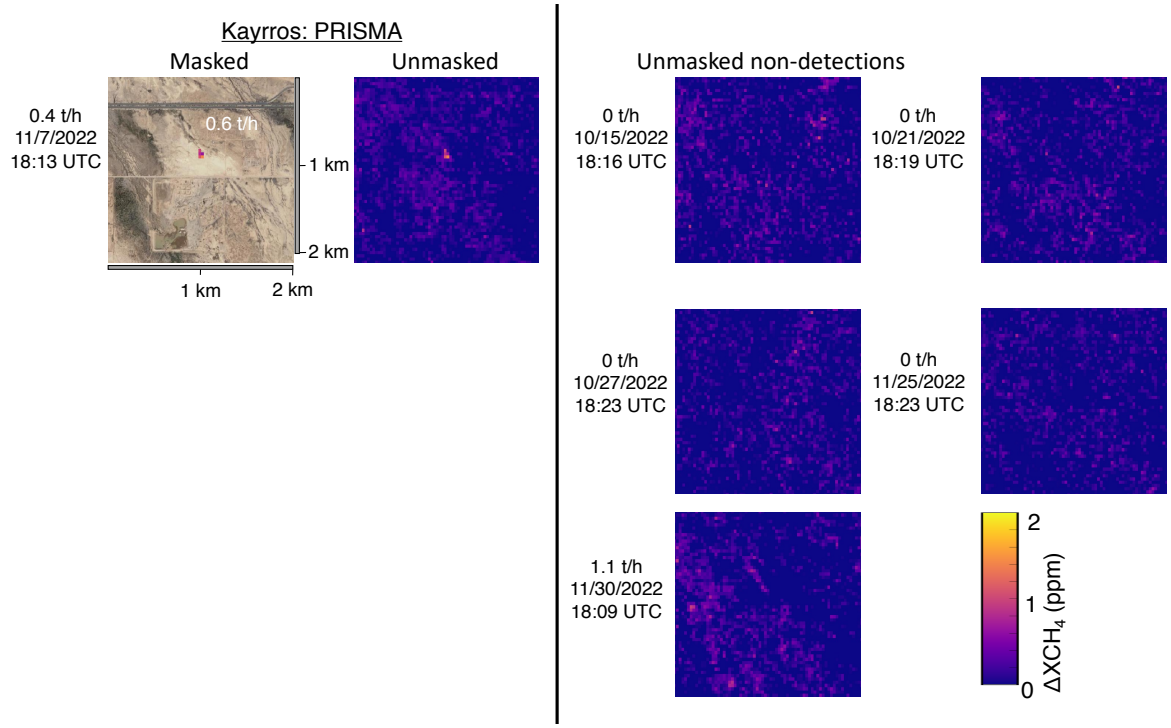


Figure 37. Provided masked and unmasked methane enhancement estimates from Kayrros for PRISMA retrievals. Surface imagery © 2023 Google Earth, CNES/Airbus, Maxar Technologies, USDA/FPAC/GEO.

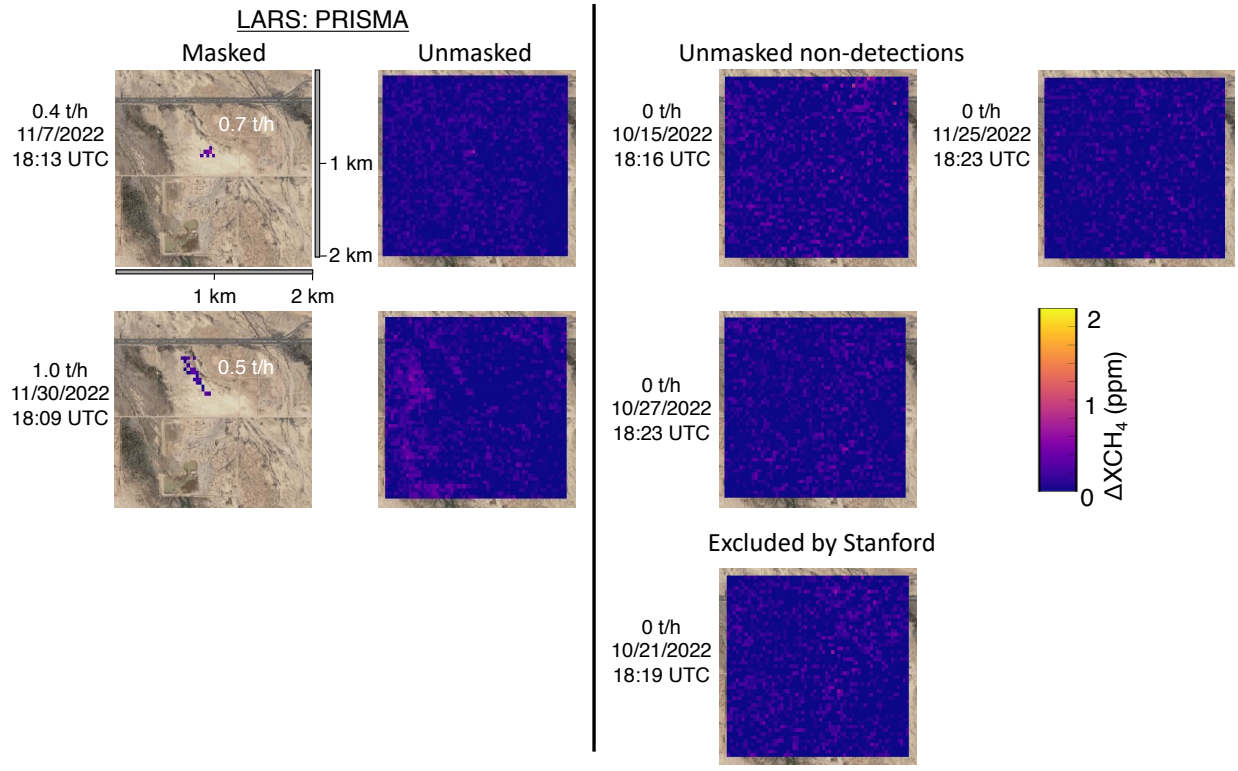


Figure 38. Provided masked and unmasked methane enhancement estimates from LARS for PRISMA retrievals. Surface imagery © 2023 Google Earth, CNES/Airbus, Maxar Technologies, USDA/FPAC/GEO.

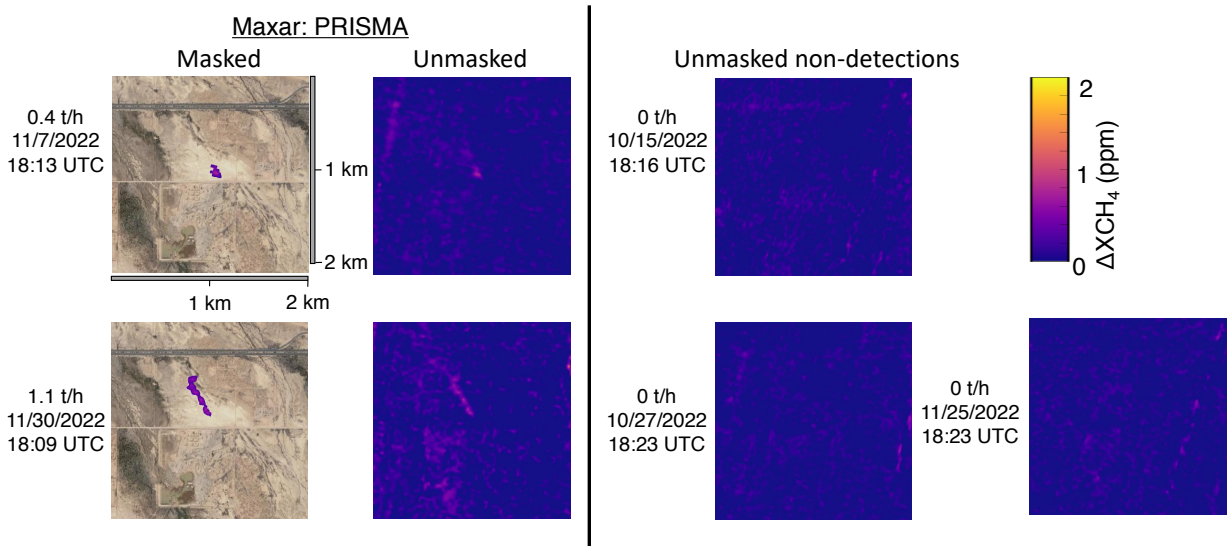


Figure 39. Provided masked and unmasked methane enhancement estimates from Maxar for PRISMA retrievals. Surface imagery © 2023 Google Earth, CNES/Airbus, Maxar Technologies, USDA/FPAC/GEO.

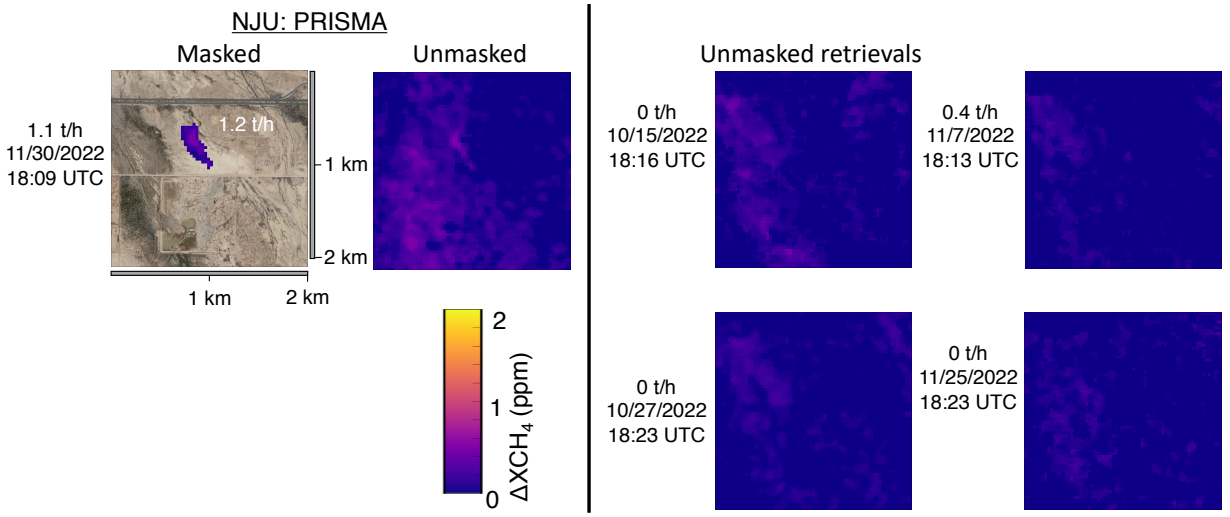


Figure 40. Provided masked and unmasked methane enhancement estimates from NJU for PRISMA retrievals. Surface imagery © 2023 Google Earth, CNES/Airbus, Maxar Technologies, USDA/FPAC/GEO.

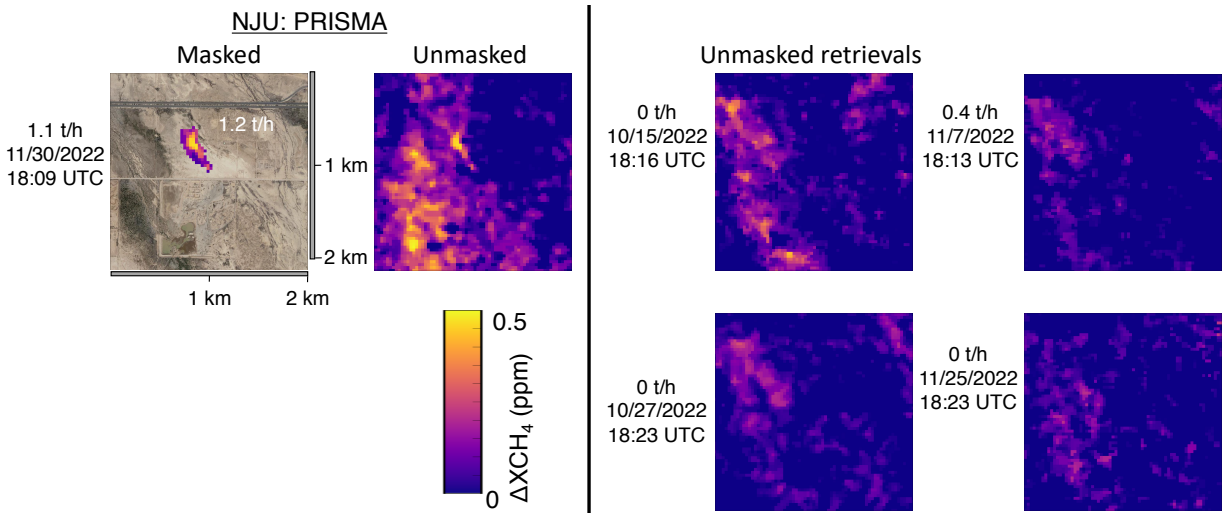


Figure 41. Custom-PPM scale provided masked and unmasked methane enhancement estimates from NJU for PRISMA retrievals. Surface imagery © 2023 Google Earth, CNES/Airbus, Maxar Technologies, USDA/FPAC/GEO.

S.4.6.7. Sentinel-2

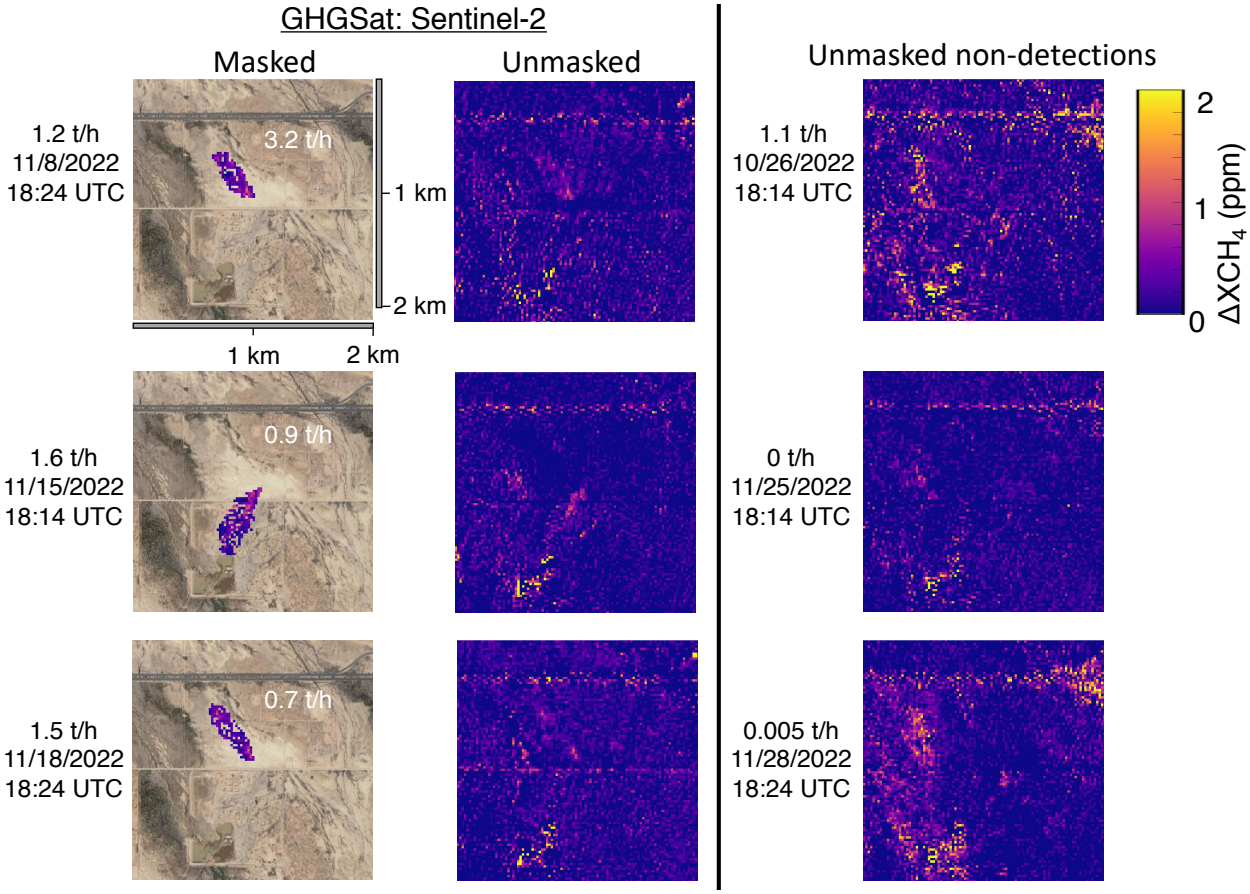


Figure 42. Provided masked and unmasked methane enhancement estimates from GHGSat for Sentinel-2 retrievals. Surface imagery © 2023 Google Earth, CNES/Airbus, Maxar Technologies, USDA/FPAC/GEO.

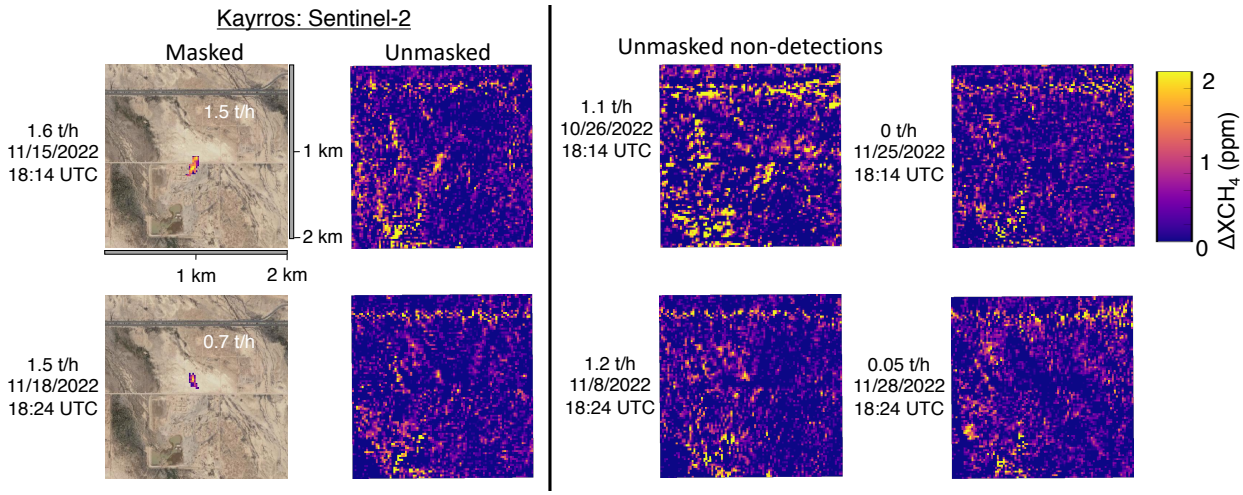


Figure 43. Provided masked and unmasked methane enhancement estimates from Kayrros for Sentinel-2 retrievals. Surface imagery © 2023 Google Earth, CNES/Airbus, Maxar Technologies, USDA/FPAC/GEO.

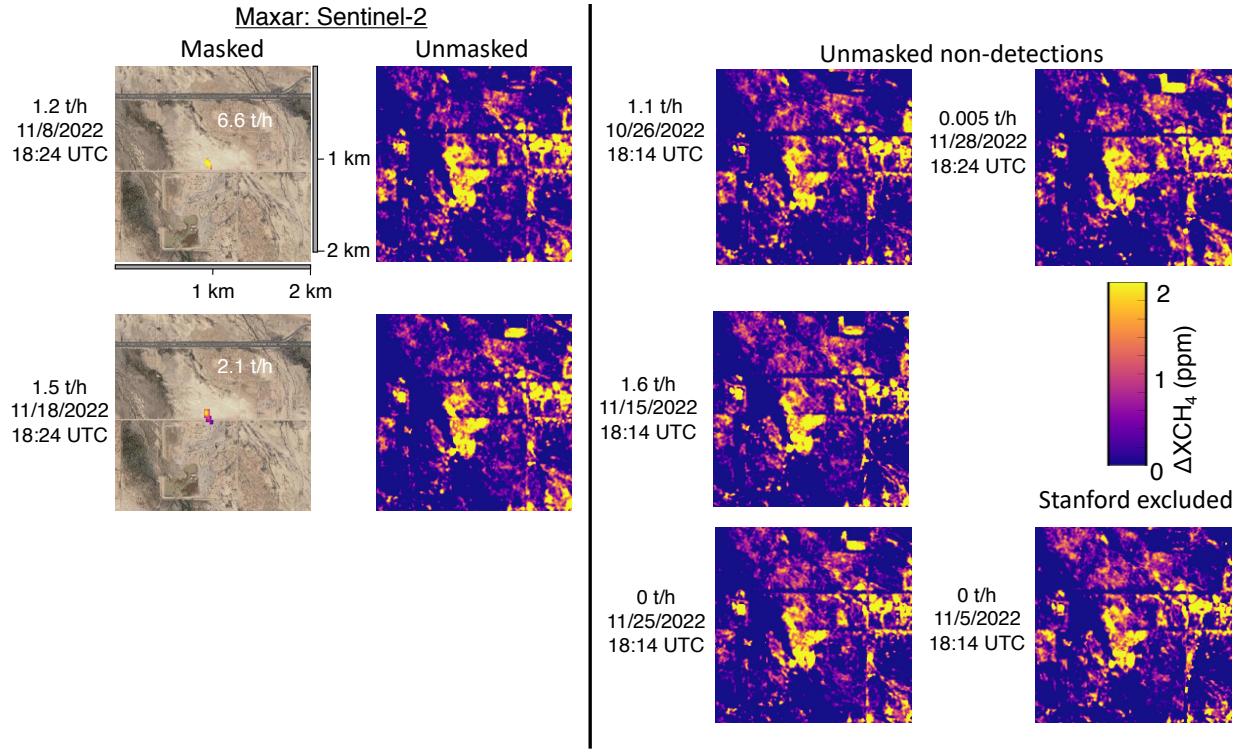


Figure 44. Provided masked and unmasked methane enhancement estimates from Maxar for Sentinel-2 retrievals. Surface imagery © 2023 Google Earth, CNES/Airbus, Maxar Technologies, USDA/FPAC/GEO.

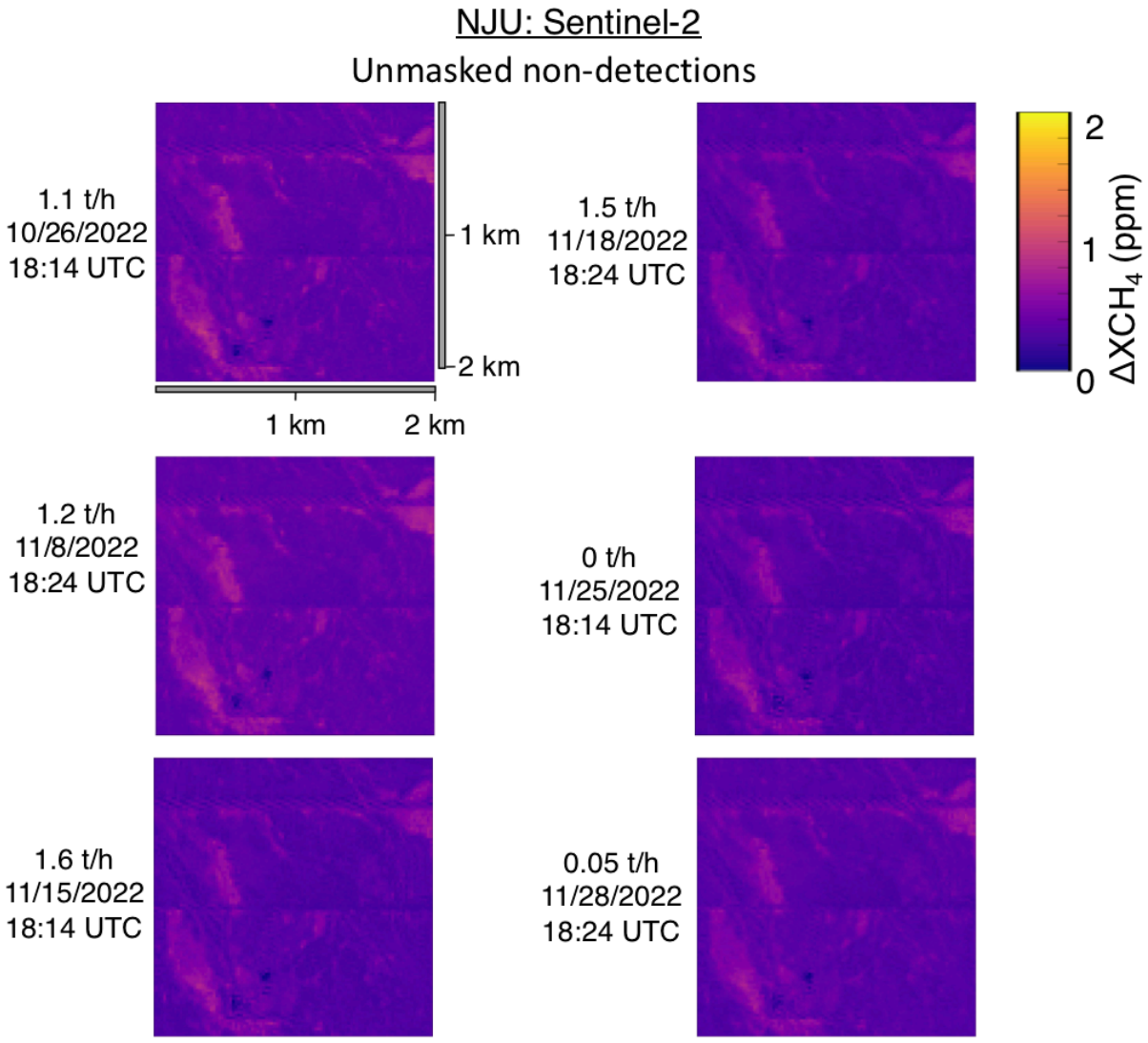


Figure 45. Provided masked and unmasked methane enhancement estimates from NJU for Sentinel-2 retrievals. Surface imagery © 2023 Google Earth, CNES/Airbus, Maxar Technologies, USDA/FPAC/GEO.

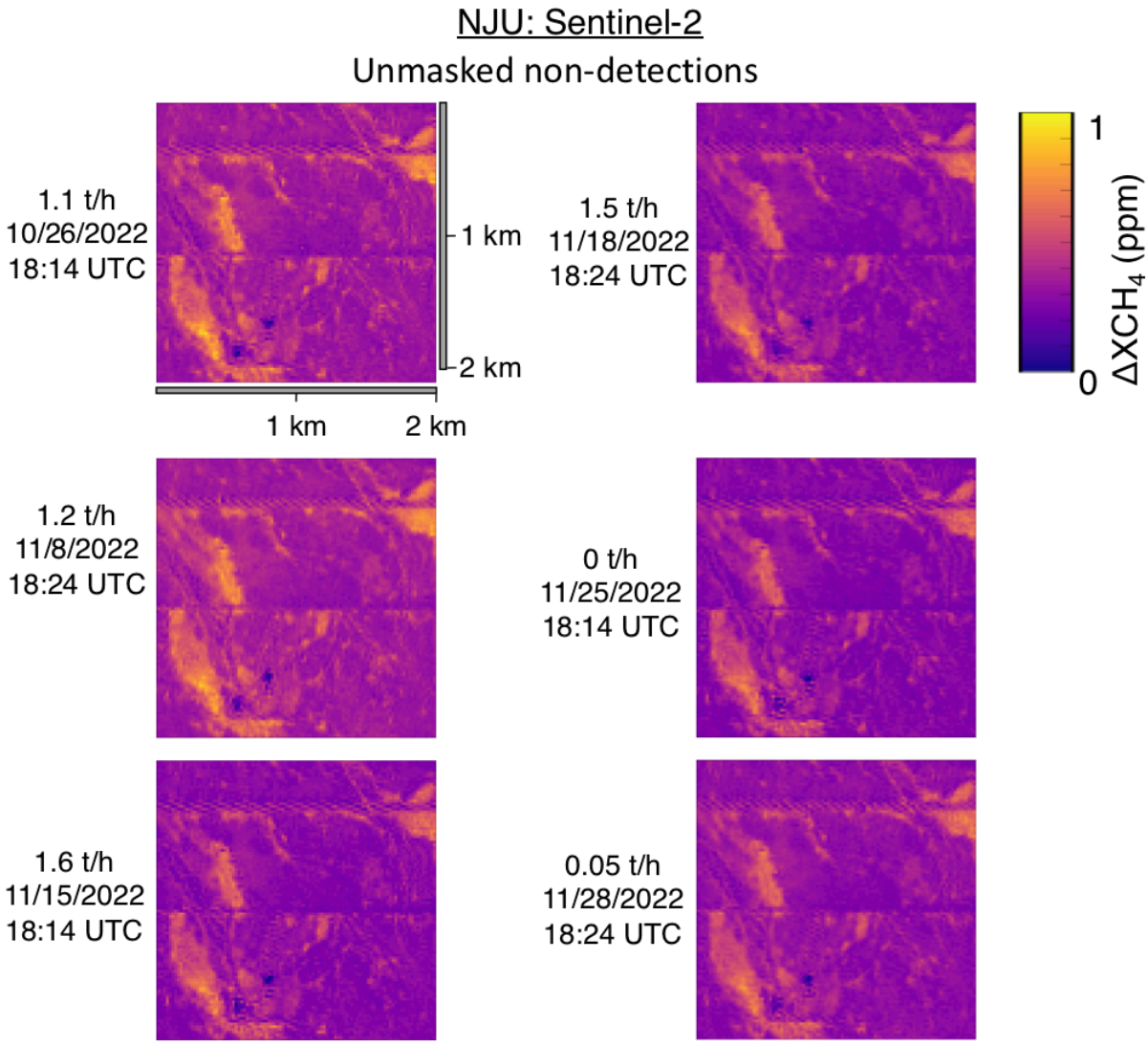


Figure 46. Custom-PPM scale, provided masked and unmasked methane enhancement estimates from NJU for Sentinel-2 retrievals. Surface imagery © 2023 Google Earth, CNES/Airbus, Maxar Technologies, USDA/FPAC/GEO.

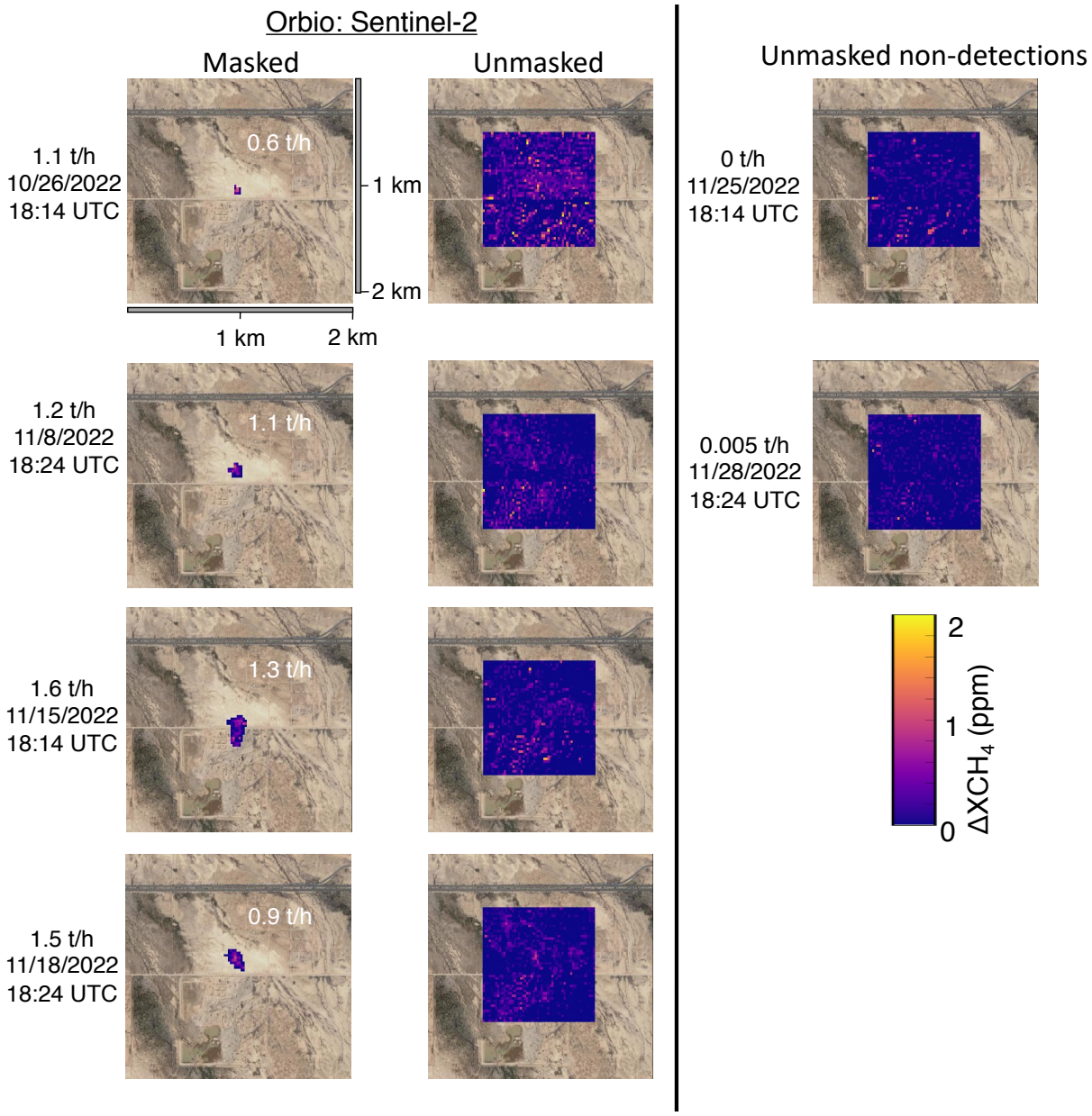


Figure 47. Provided masked and unmasked methane enhancement estimates from Orbio Earth for Sentinel-2 retrievals. Surface imagery © 2023 Google Earth, CNES/Airbus, Maxar Technologies, USDA/FPAC/GEO.

S.4.6.8. WorldView-3

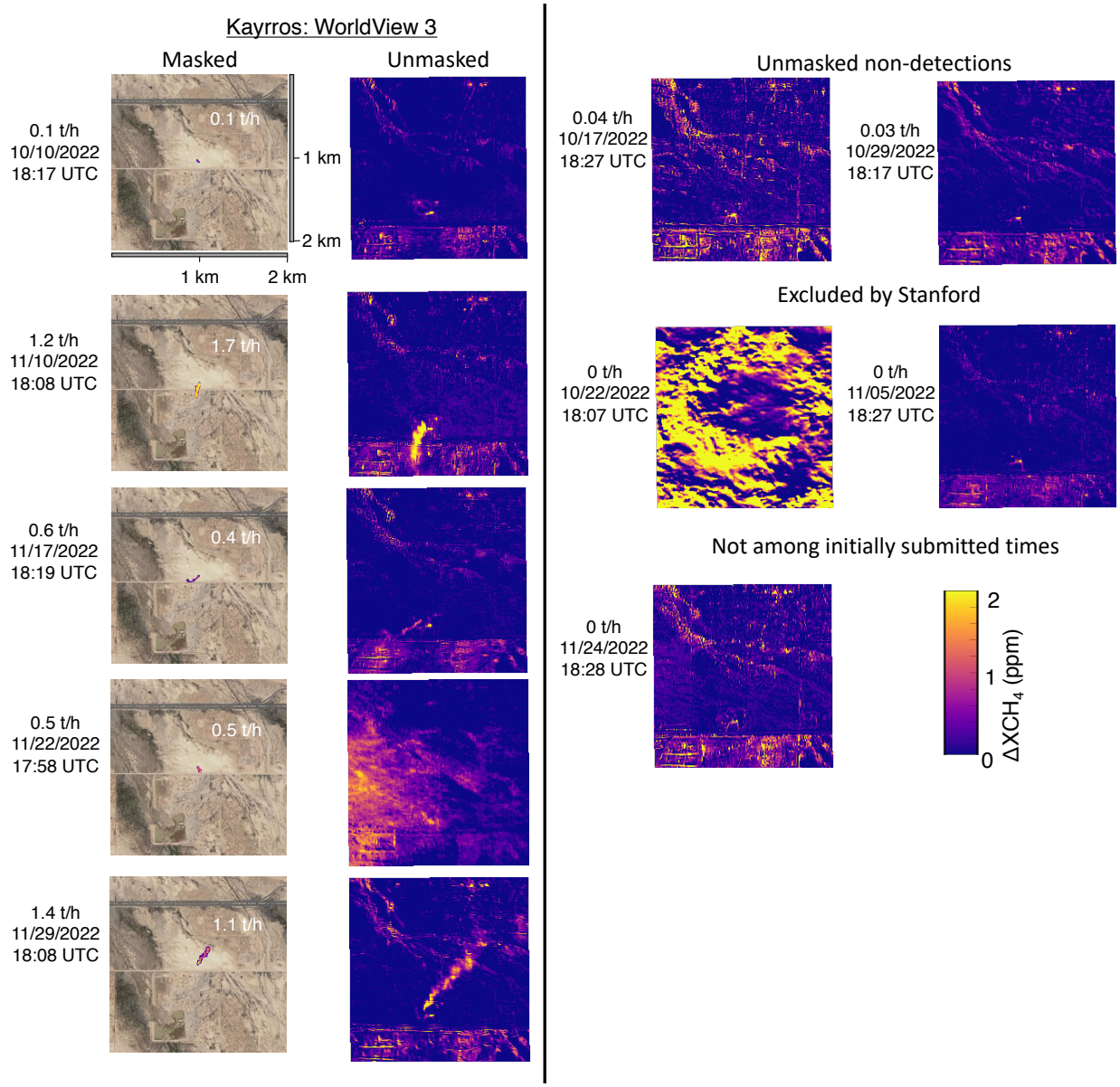


Figure 48. Provided masked and unmasked methane enhancement estimates from Kayrros for WorldView-3 retrievals. Note that unmasked images shift the frame roughly 1 km north compared with the masked images and zoom in on a smaller area. Surface imagery © 2023 Google Earth, CNES/Airbus, Maxar Technologies, USDA/FPAC/GEO.

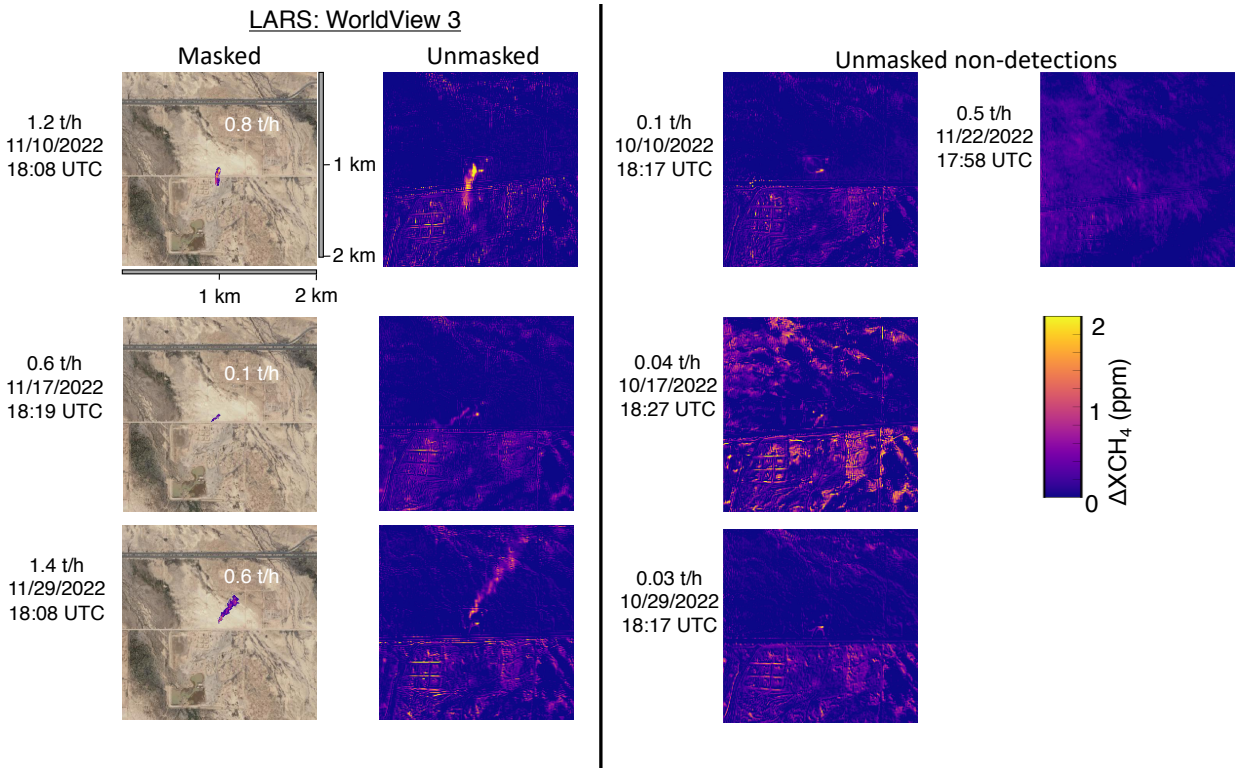


Figure 49. Provided masked and unmasked methane enhancement estimates from LARS for WorldView-3 retrievals. Note that unmasked images focus on a smaller area. Surface imagery © 2023 Google Earth, CNES/Airbus, Maxar Technologies, USDA/FPAC/GEO. Note that LARS researcher Javier Gorroño submitted Stage 1 WorldView 3 estimates after LARS researcher Javier Roger Juan had received unblinded in situ wind data. Javier Gorroño then submitted Stage 2 WorldView 3 estimates, not included in the main manuscript, after release volumes were unblinded. Although Stanford researchers believe LARS WorldView 3 estimates did not use the ground truth wind data for their Stage 1 estimates or the metered volumes for their Stage 2 estimates, we include them only in the SI to maintain strict adherence to our experimental design.

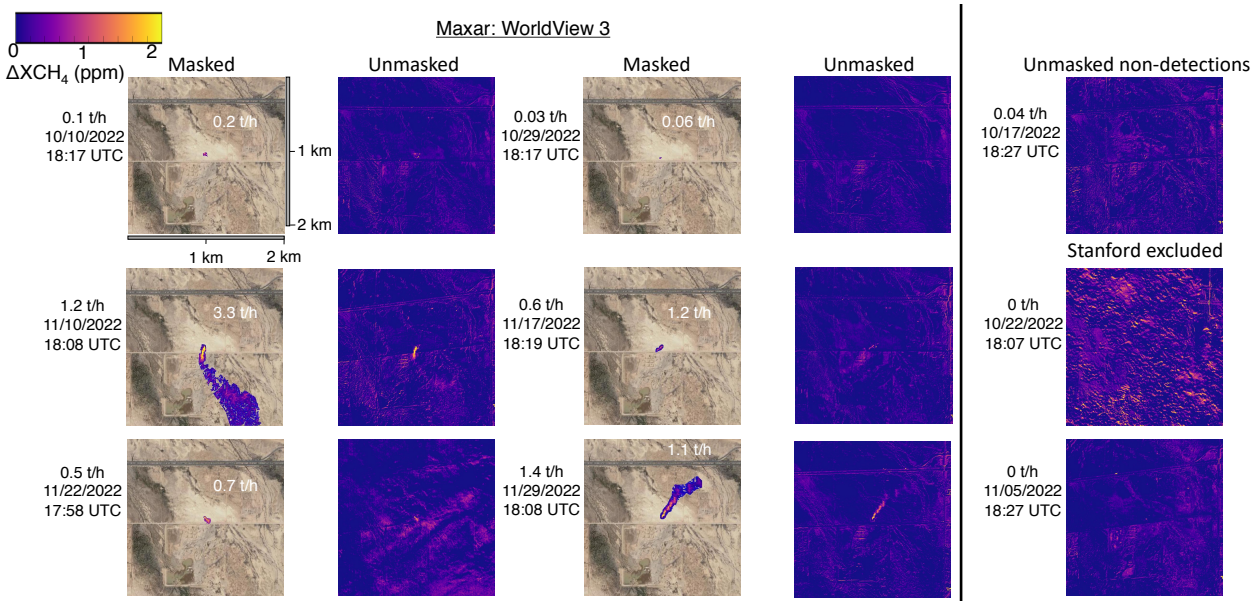


Figure 50. Provided masked and unmasked methane enhancement estimates from Maxar for WorldView-3 retrievals. Surface imagery © 2023 Google Earth, CNES/Airbus, Maxar Technologies, USDA/FPAC/GEO.

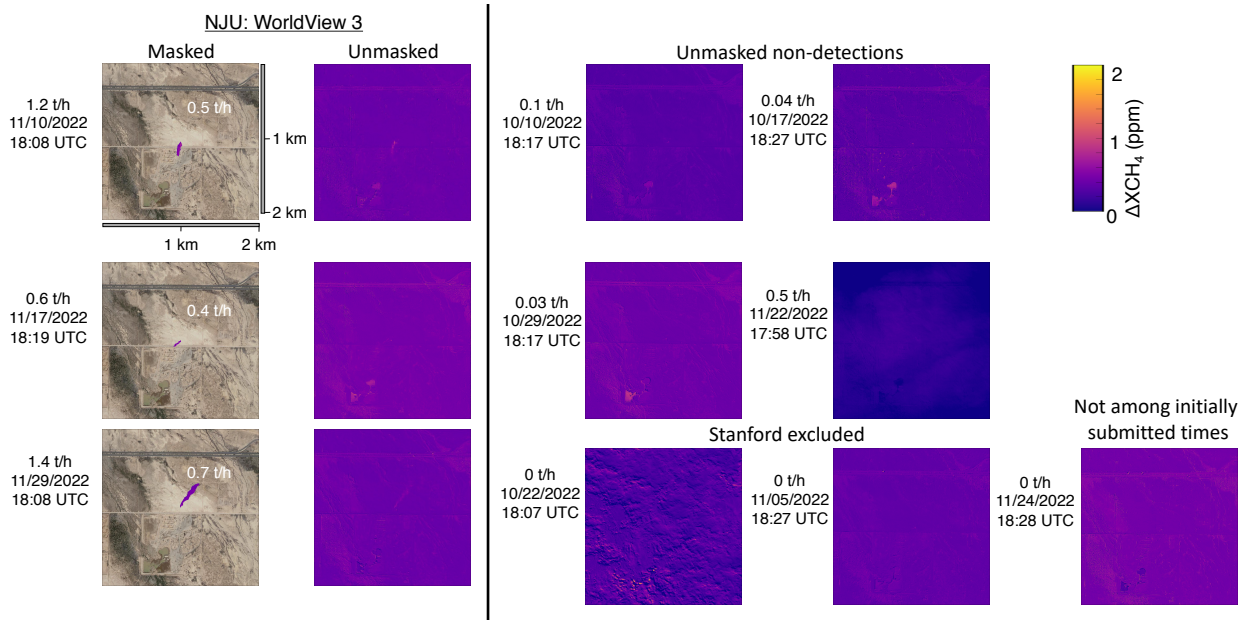


Figure 51. Provided masked and unmasked methane enhancement estimates from NJU for WorldView-3 retrievals. Surface imagery © 2023 Google Earth, CNES/Airbus, Maxar Technologies, USDA/FPAC/GEO.

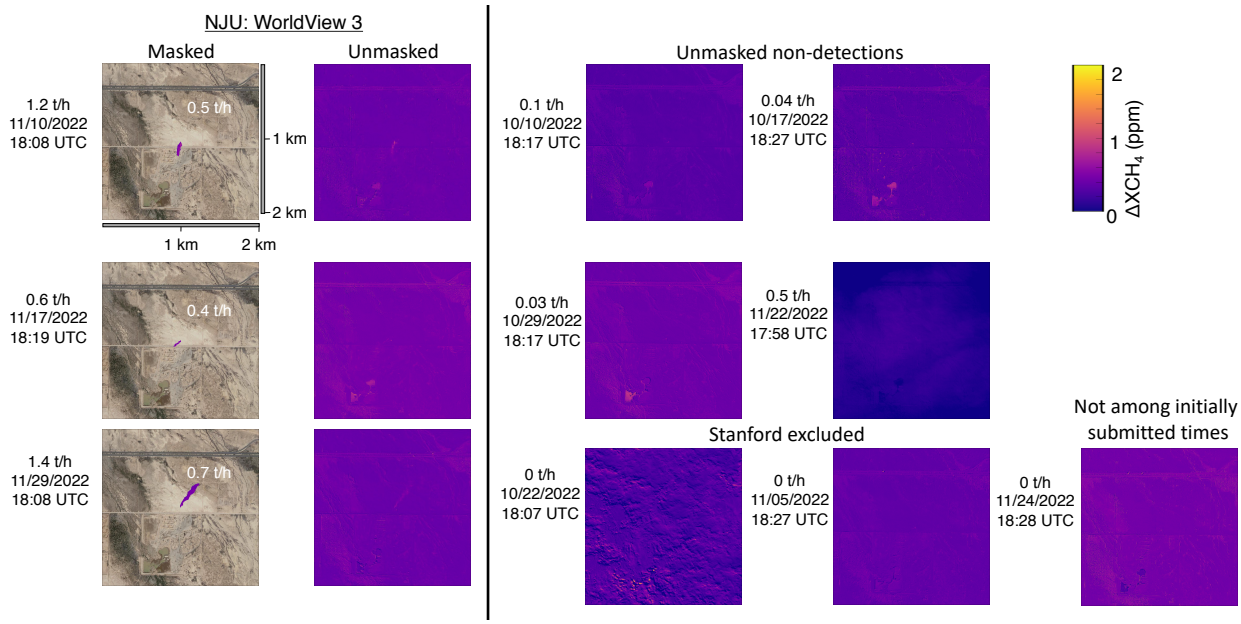


Figure 52. Custom-PPM scale, provided masked and unmasked methane enhancement estimates from NJU for WorldView-3 retrievals. Surface imagery © 2023 Google Earth, CNES/Airbus, Maxar Technologies, USDA/FPAC/GEO.

S.4.6.9. Ziyuan (ZY1)

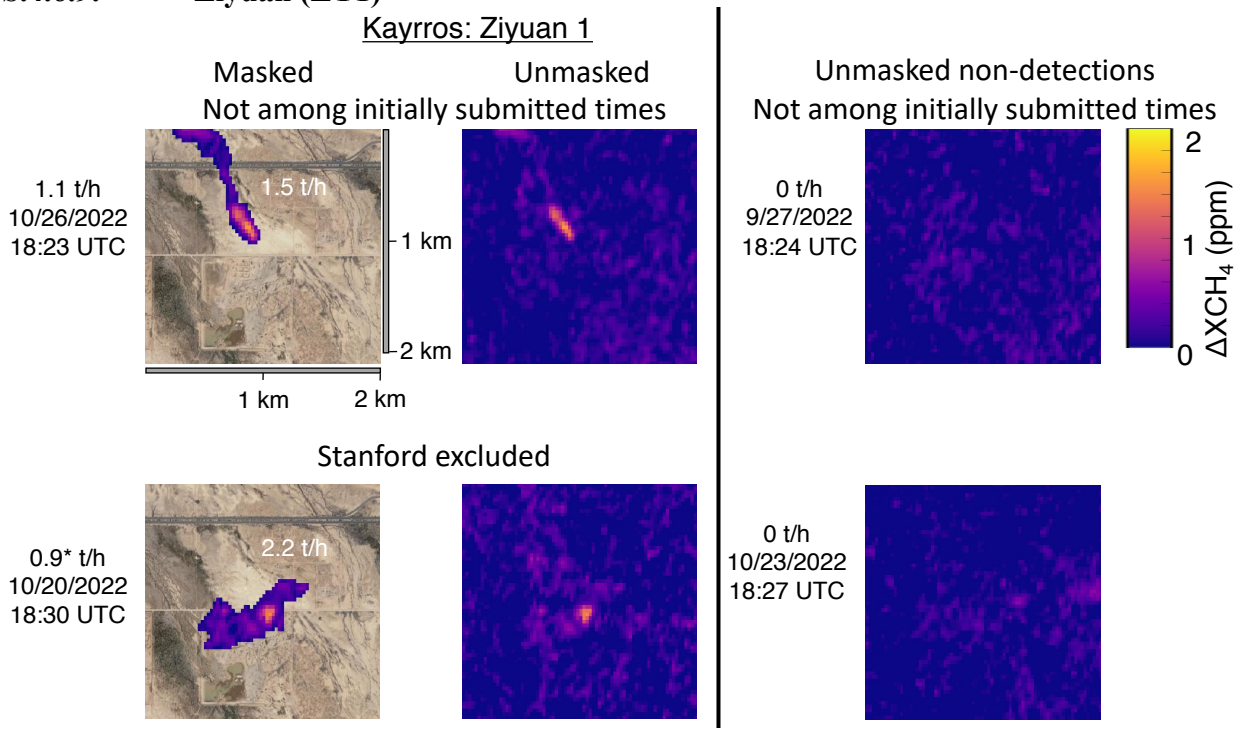


Figure 53. Provided masked and unmasked methane enhancement estimates from Kayrros for ZY1 retrievals. *The October 20th release volume is estimated, as described in S3.3, due to a system malfunction that prevented data logging. Surface imagery © 2023 Google Earth, CNES/Airbus, Maxar Technologies, USDA/FPAC/GEO.

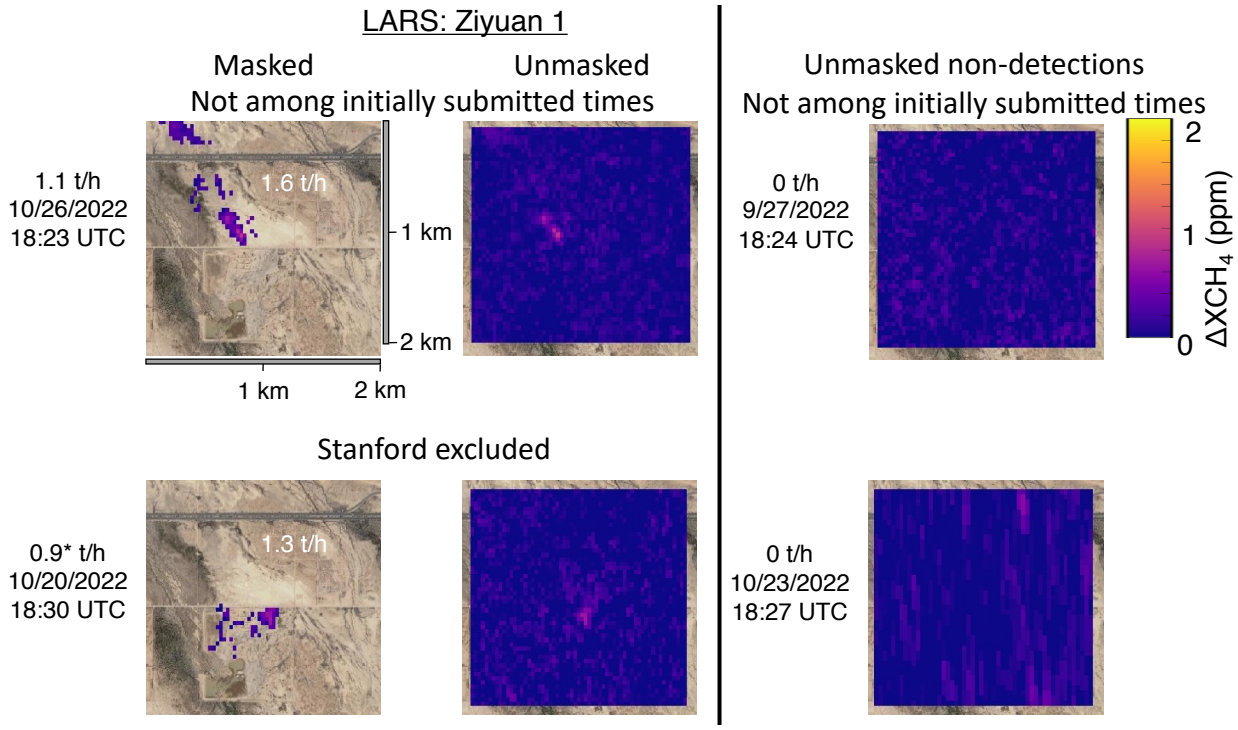


Figure 54. Provided masked and unmasked methane enhancement estimates from LARS for ZY1 retrievals. *The October 20th release volume is estimated, as described in S3.3, due to a system malfunction that prevented data logging. Surface imagery © 2023 Google Earth, CNES/Airbus, Maxar Technologies, USDA/FPAC/GEO.

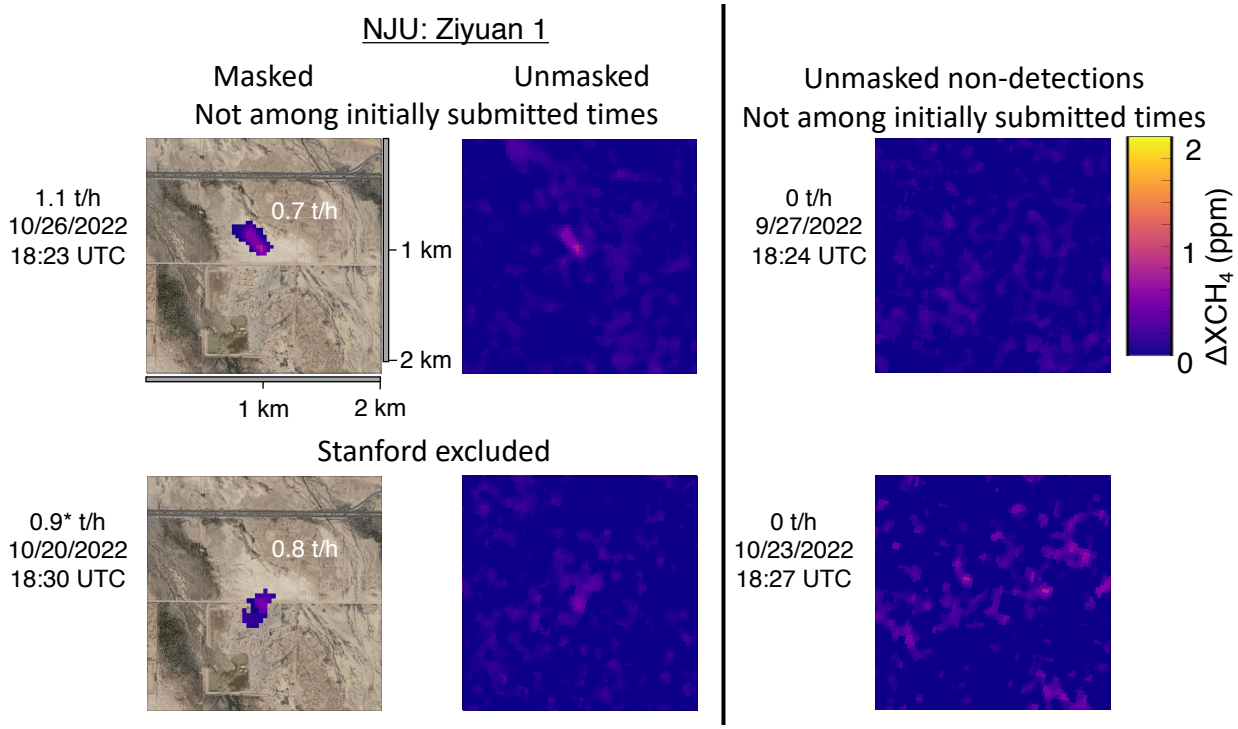


Figure 55. Provided masked and unmasked methane enhancement estimates from NJU for ZY1 retrievals. *The October 20th release volume is estimated, as described in S3.3, due to a system malfunction that prevented data logging. Surface imagery © 2023 Google Earth, CNES/Airbus, Maxar Technologies, USDA/FPAC/GEO.

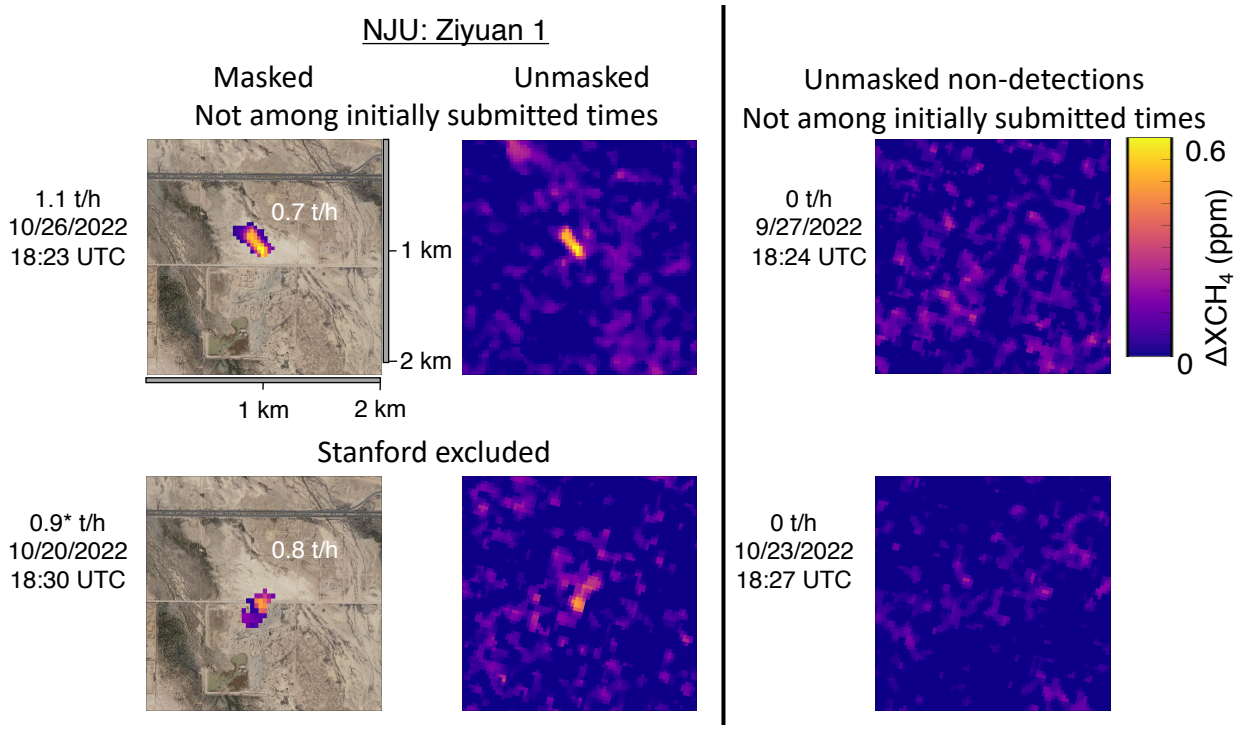


Figure 56. Custom-PPM scale, provided masked and unmasked methane enhancement estimates from NJU for ZY1 retrievals. *The October 20th release volume is estimated, as described in S3.3, due to a system malfunction that prevented data logging. Surface imagery © 2023 Google Earth, CNES/Airbus, Maxar Technologies, USDA/FPAC/GEO.

S.4.7. Optical satellite images

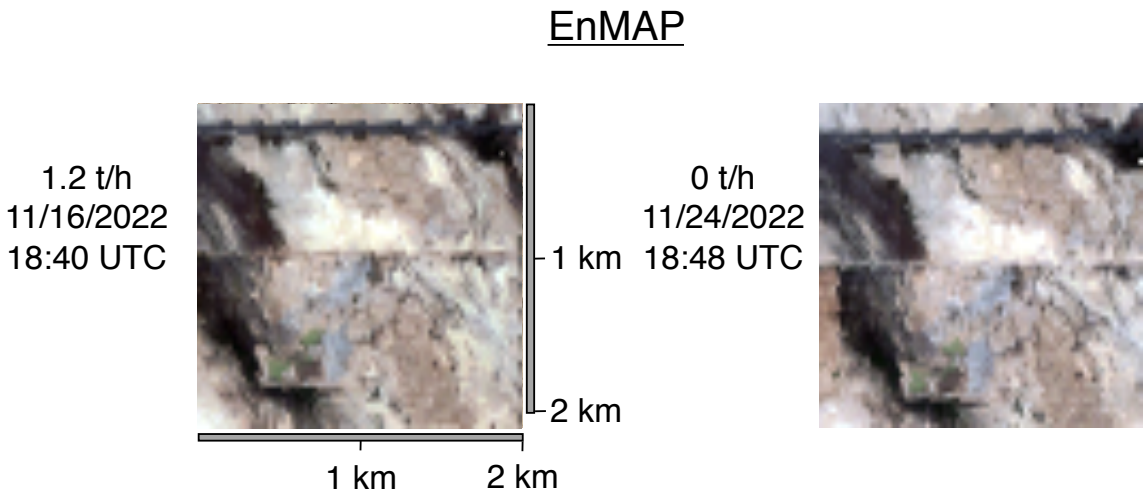


Figure 57. Optical images of the release site derived from EnMAP spectral data.

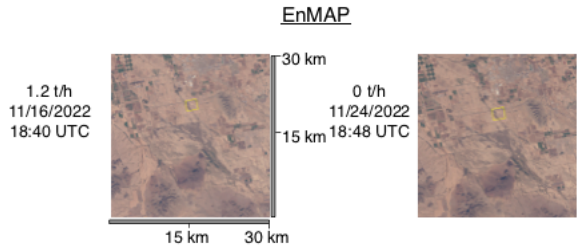


Figure 58. Wider field-of-view optical images of the release site derived from EnMAP spectral data. The 2x2 km area around the release point is highlighted in a yellow square.

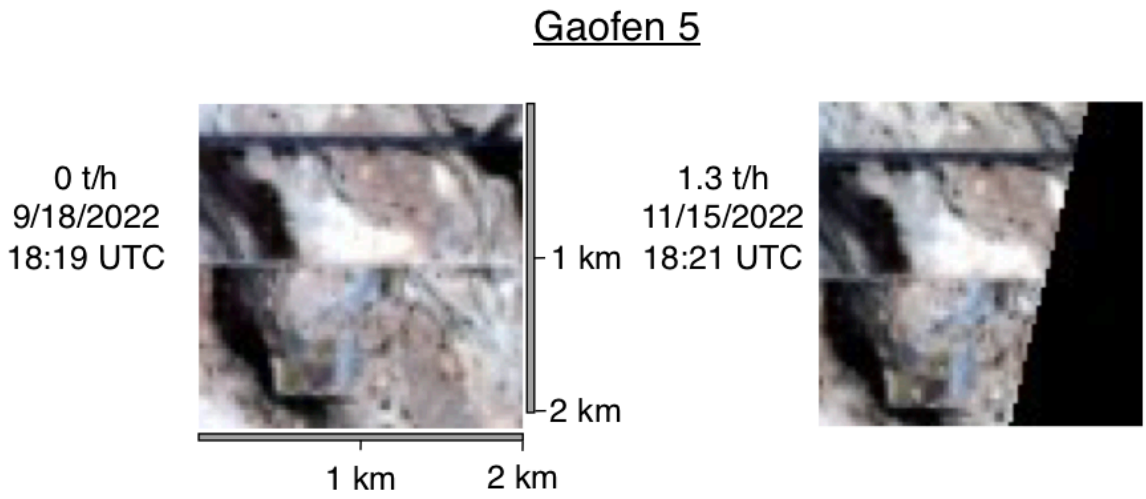


Figure 59. Optical images of the release site derived from Gaofen 5 spectral data.

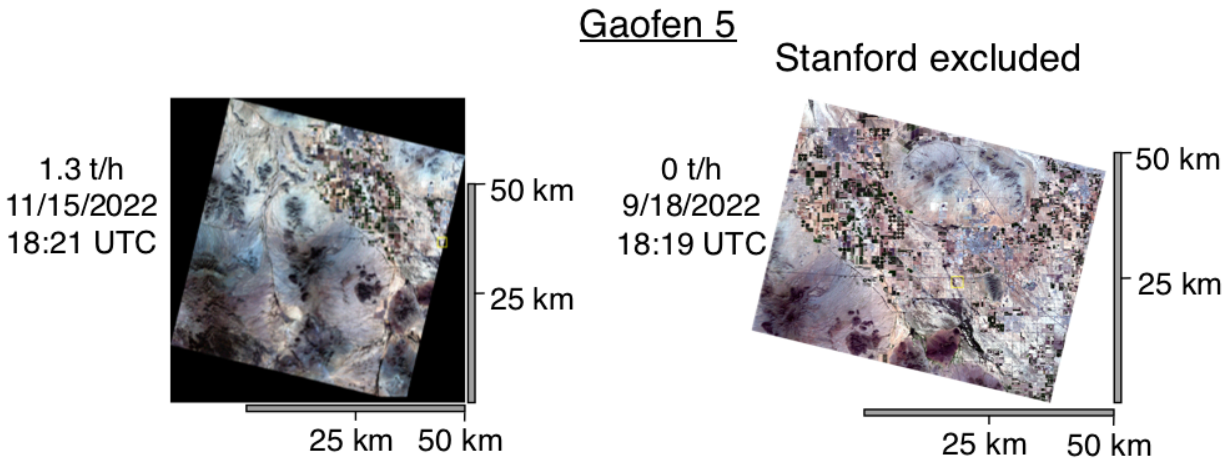


Figure 60. Wider field-of-view optical images of the release site derived from Gaofen 5 spectral data. The 2x2 km area around the release point is highlighted in a yellow square.

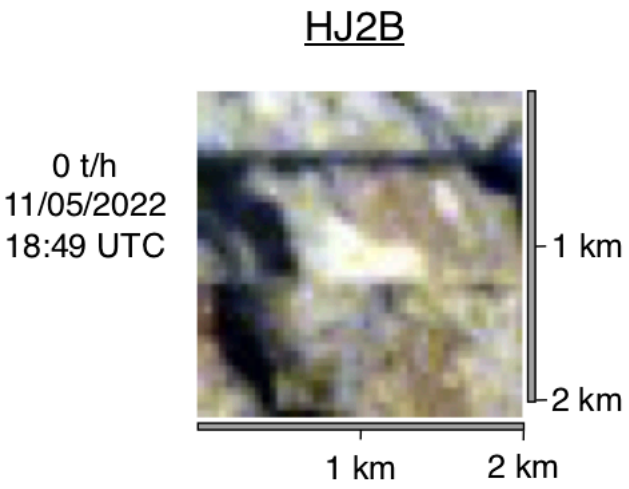


Figure 61. Optical images of the release site derived from Huanjin 2B spectral data.

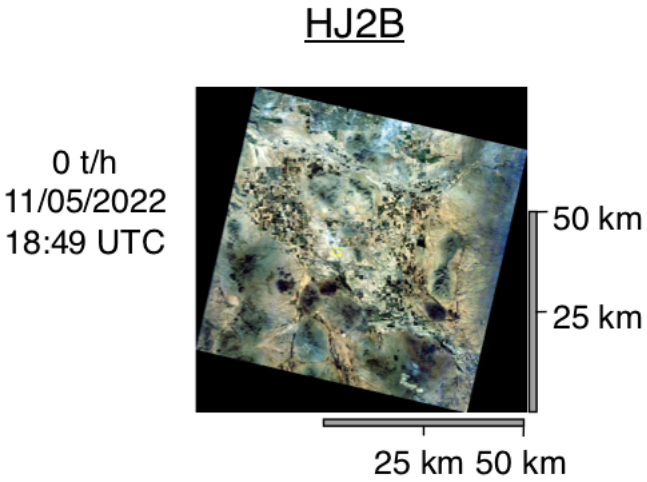


Figure 62. Wider field-of-view optical images of the release site derived from Huanjin 2B spectral data. The 2x2 km area around the release point is highlighted in a yellow square.

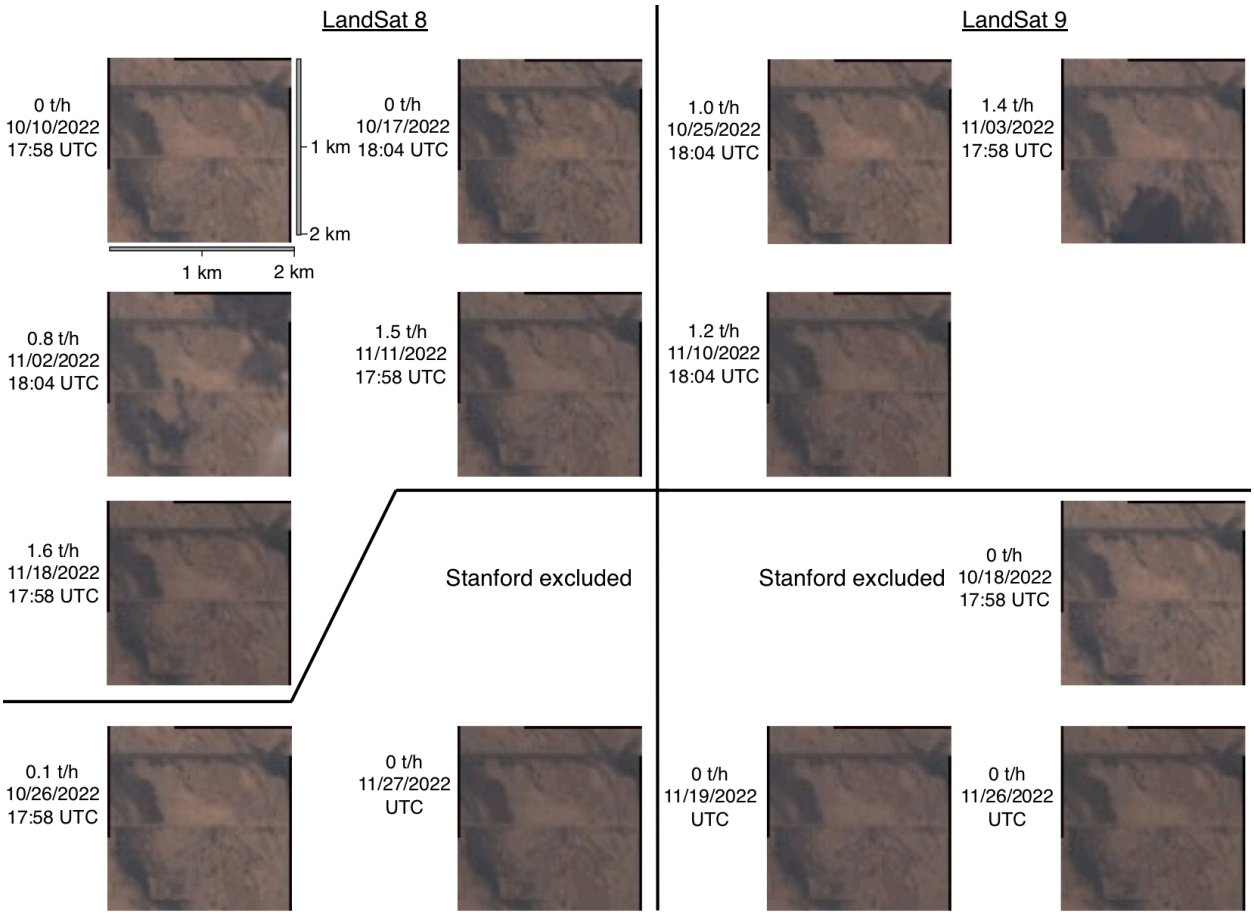


Figure 63. Optical images of the release site derived from LandSat 8/9 spectral data.

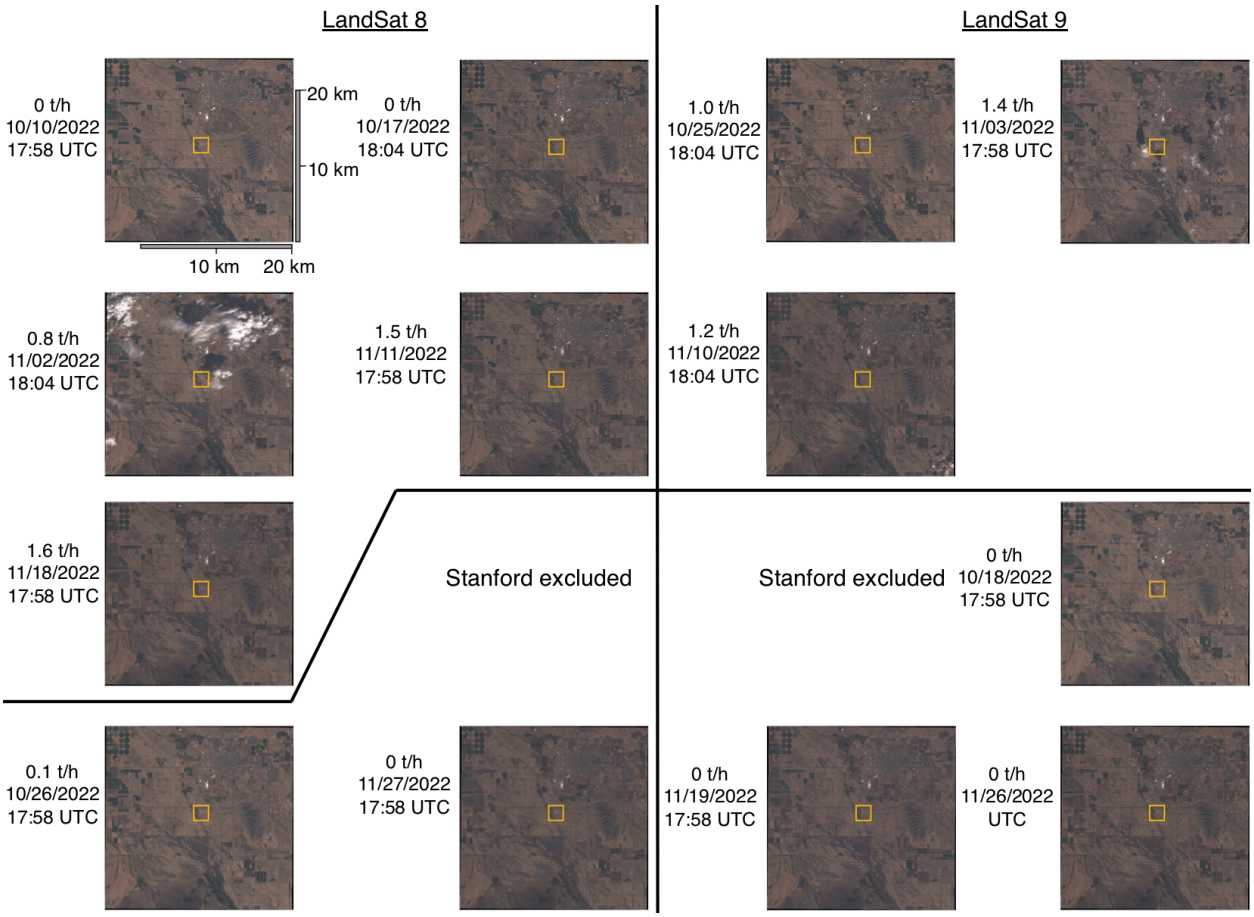


Figure 64. Wider field-of-view optical images of the release site derived from LandSat 8/9 spectral data. The 2x2 km area around the release point is highlighted in a yellow square.

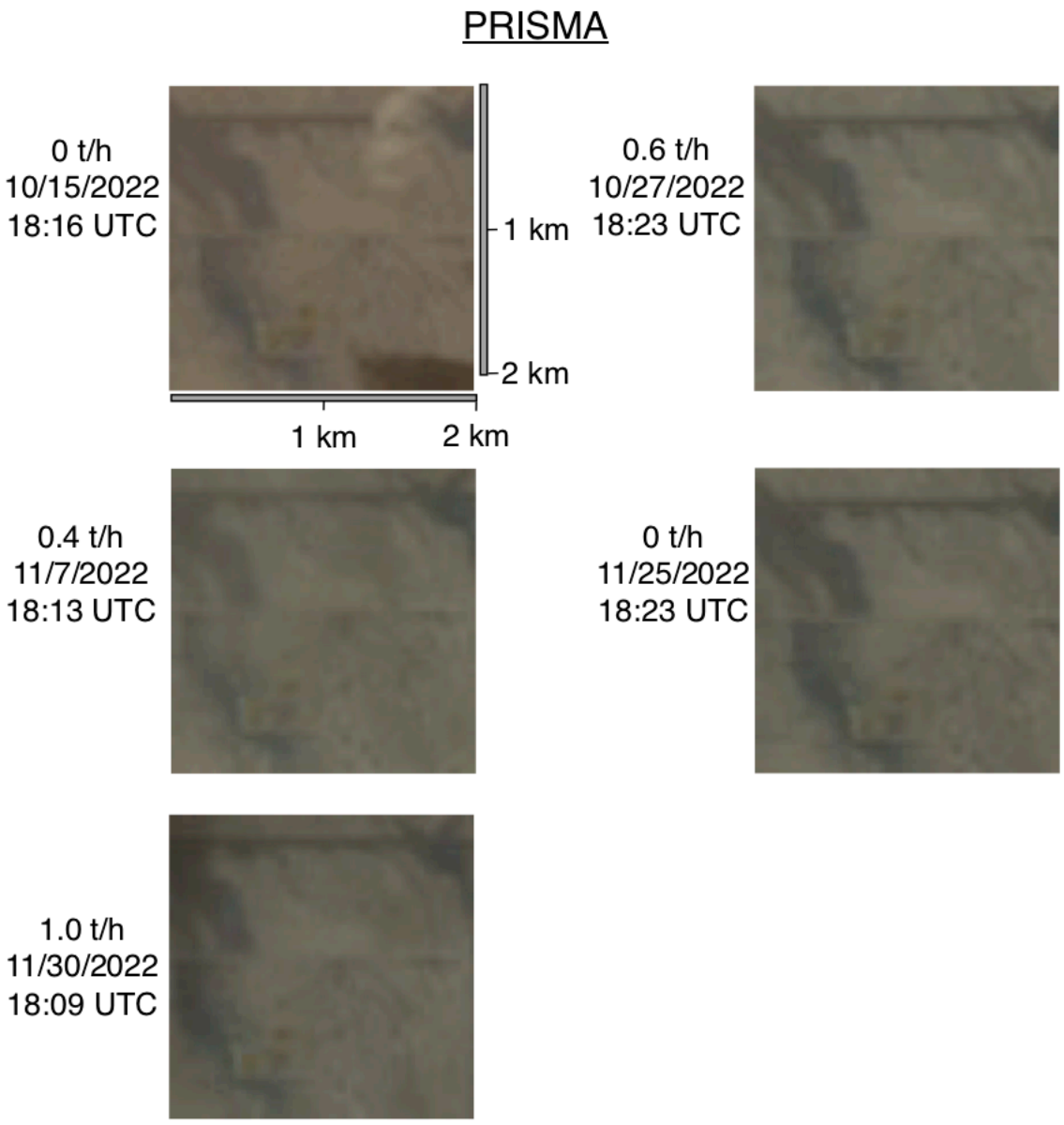


Figure 65. Optical images of the release site derived from PRISMA spectral data.

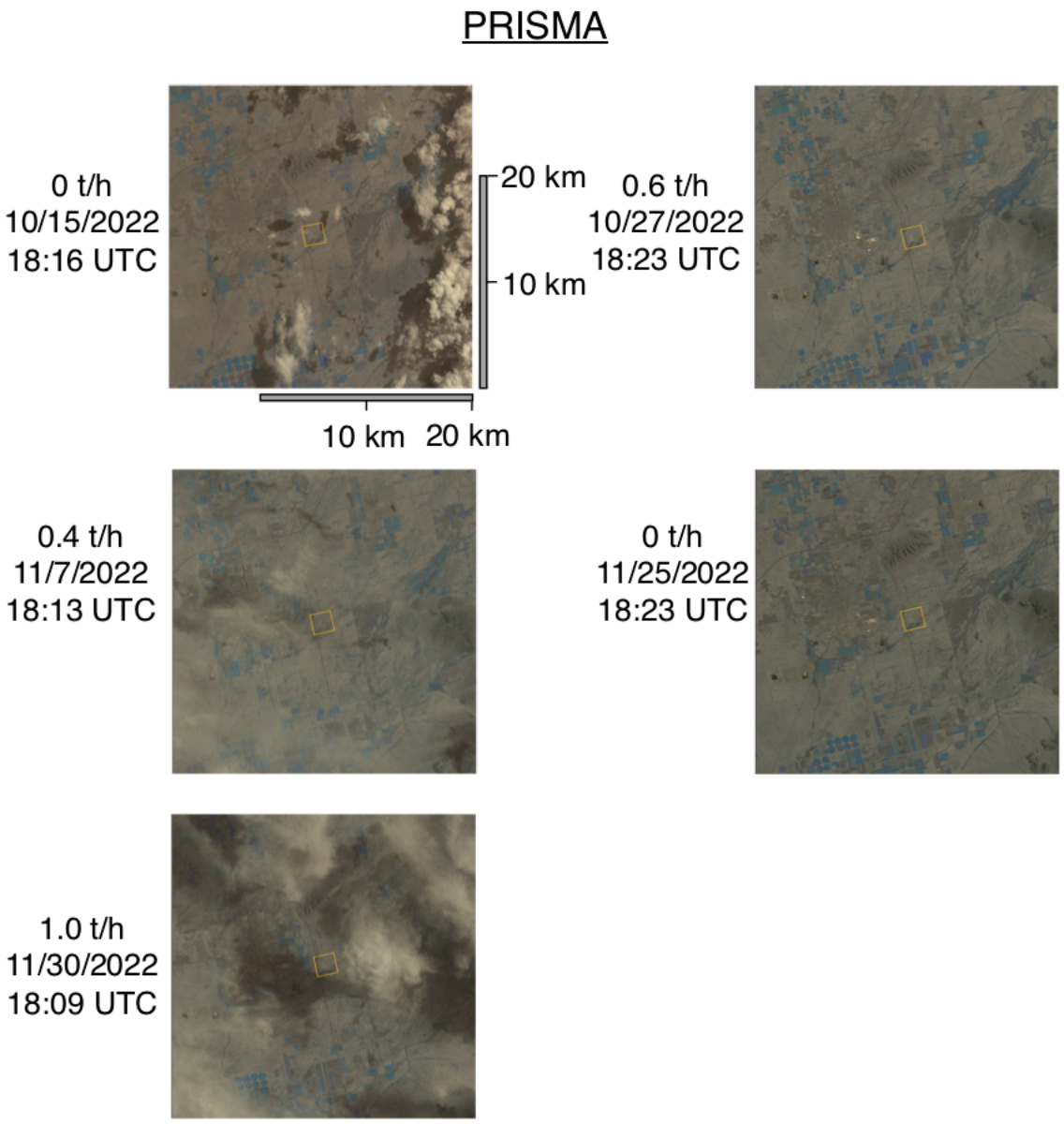


Figure 66. Wider field-of-view optical images of the release site derived from PRISMA spectral data. The 2x2 km area around the release point is highlighted in a yellow square.

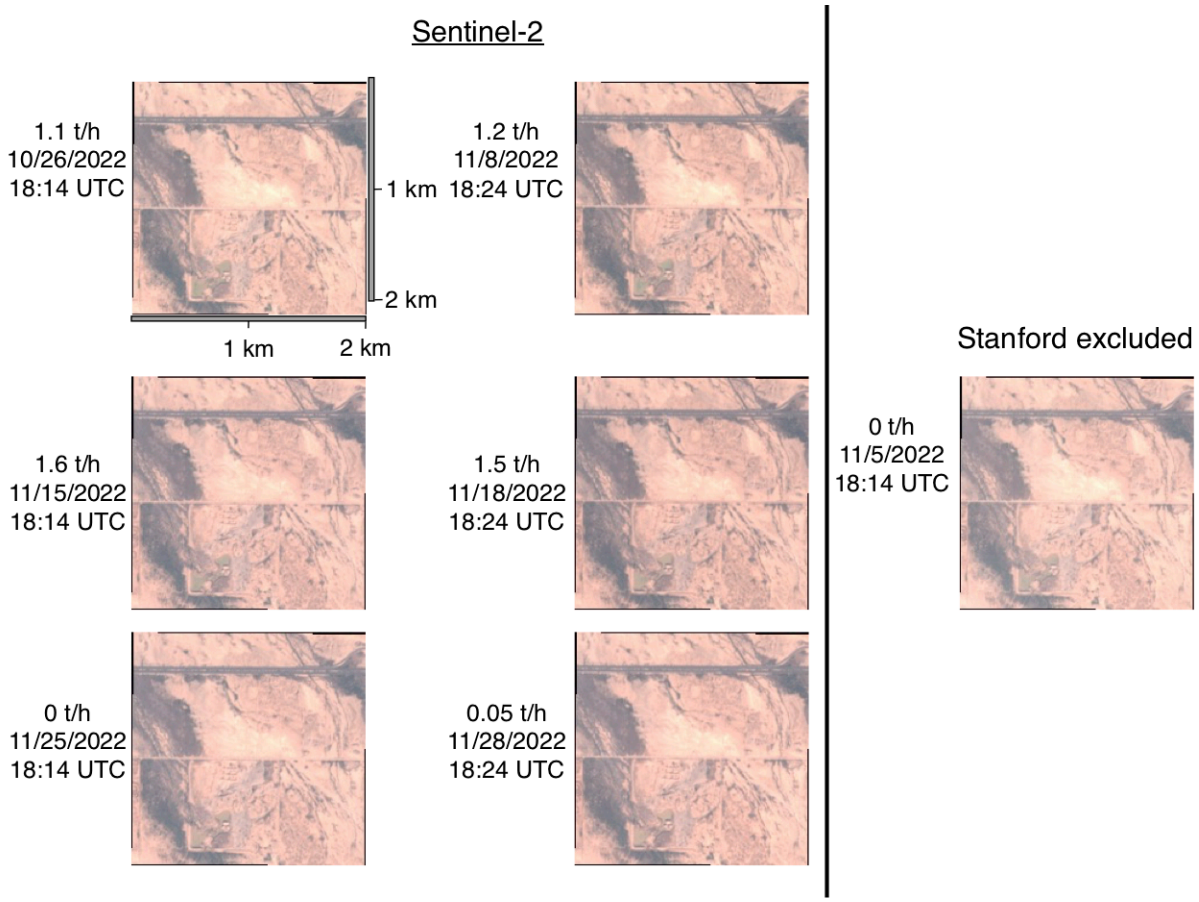


Figure 67. Optical images of the release site derived from Sentinel-2 spectral data.

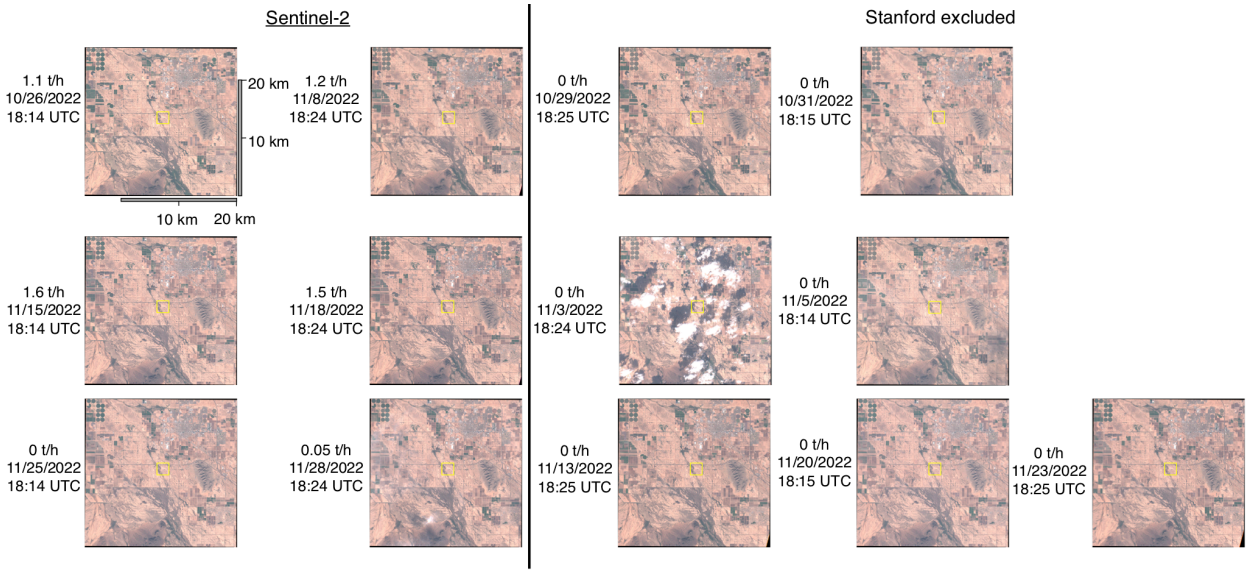


Figure 68. Wider field-of-view optical images of the release site derived from Sentinel-2 spectral data. The 2x2 km area around the release point is highlighted in a yellow square.

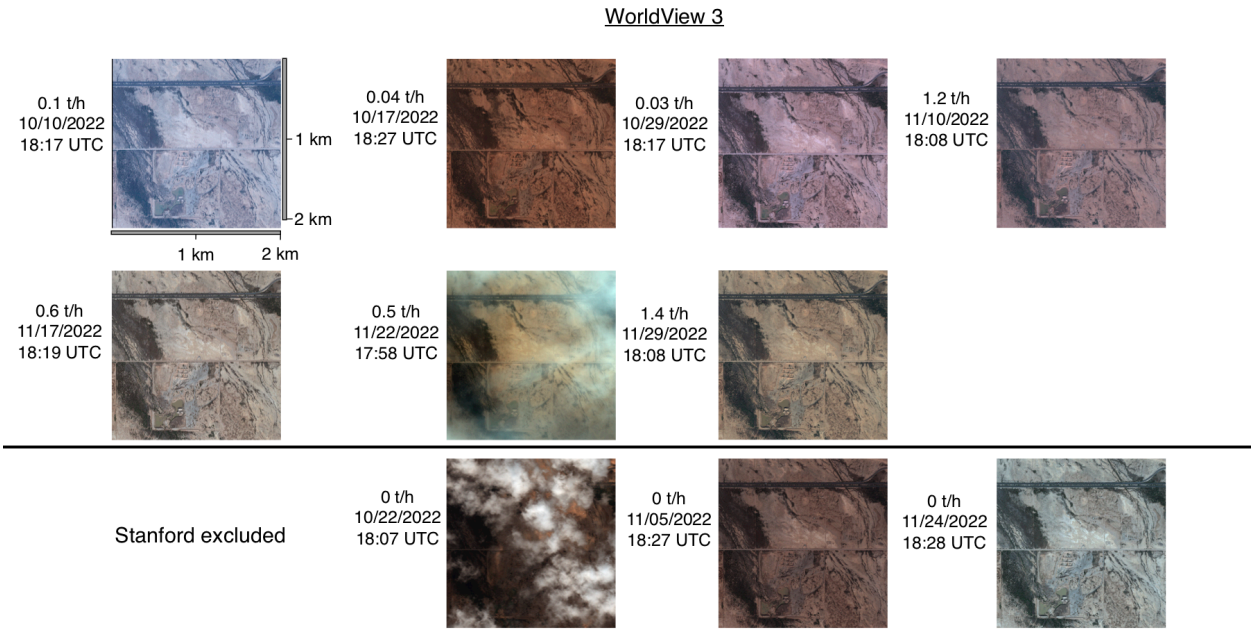


Figure 69. Optical images of the release site derived from WorldView-3 spectral data.

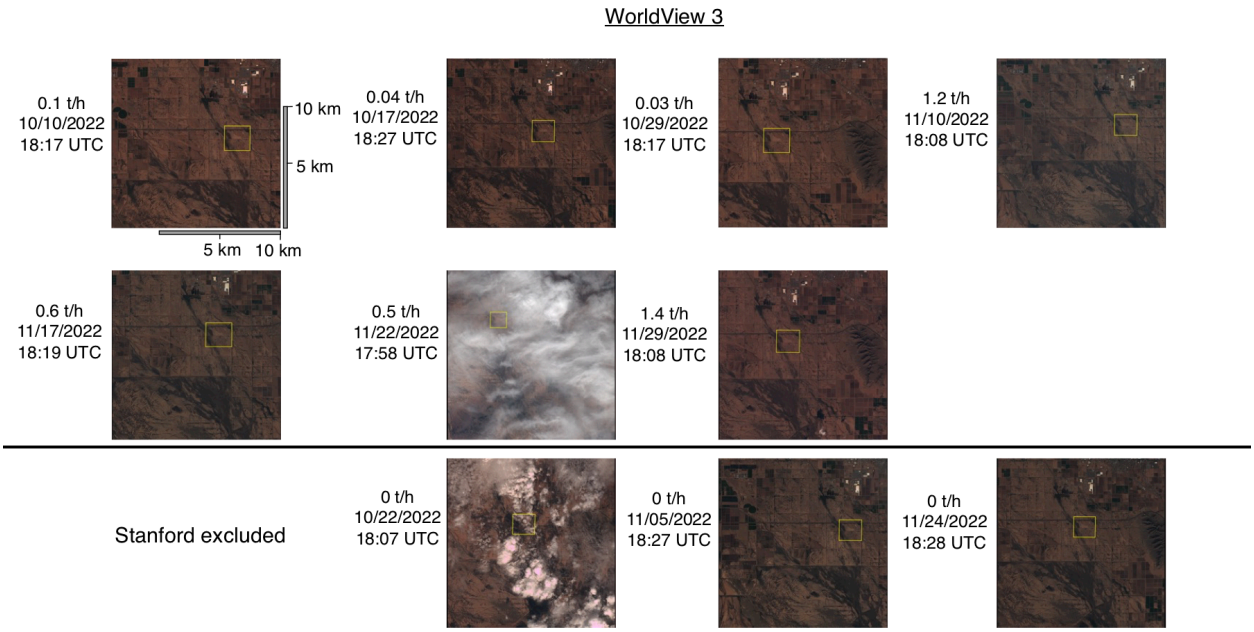


Figure 70. Wider field-of-view optical images of the release site derived from WorldView-3 spectral data. The 2x2 km area around the release point is highlighted in a yellow square.

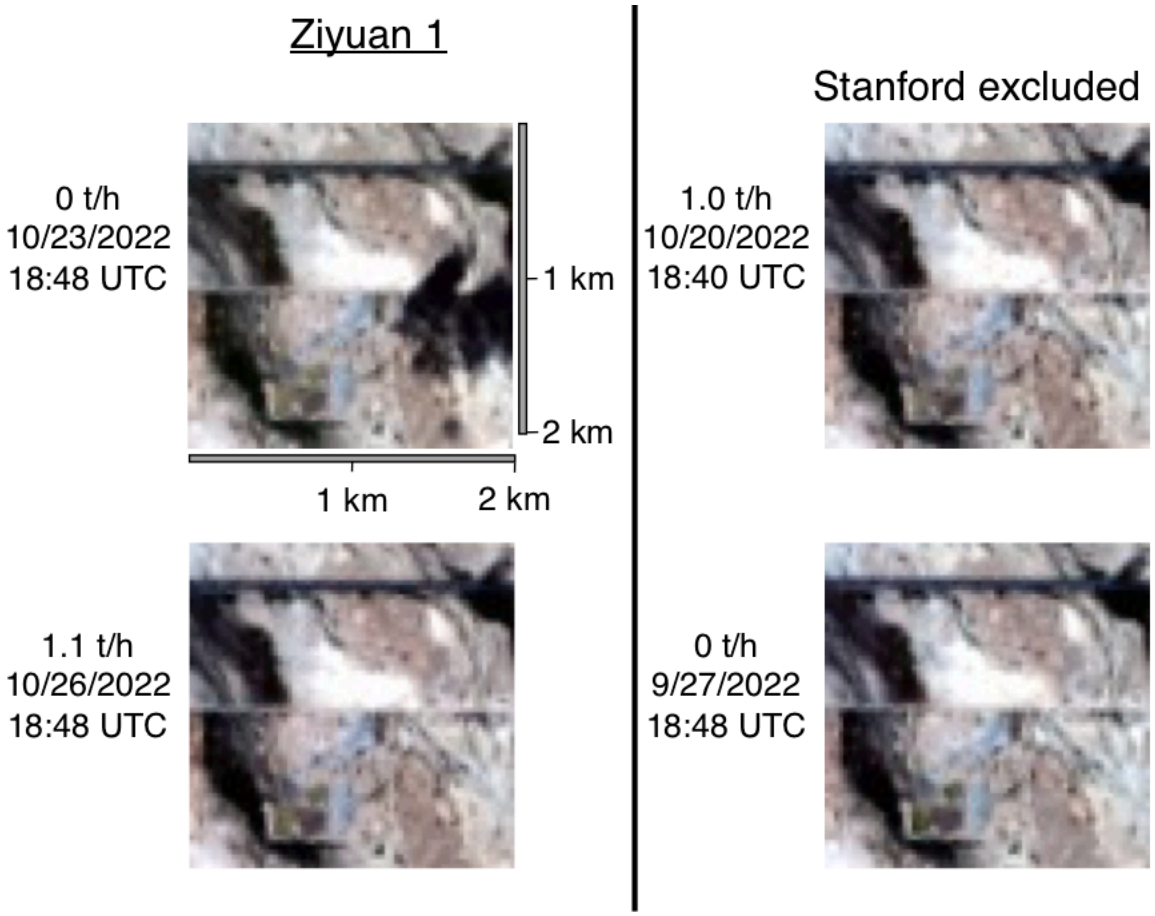


Figure 71. Optical images of the release site derived from Ziyuan 1 spectral data.

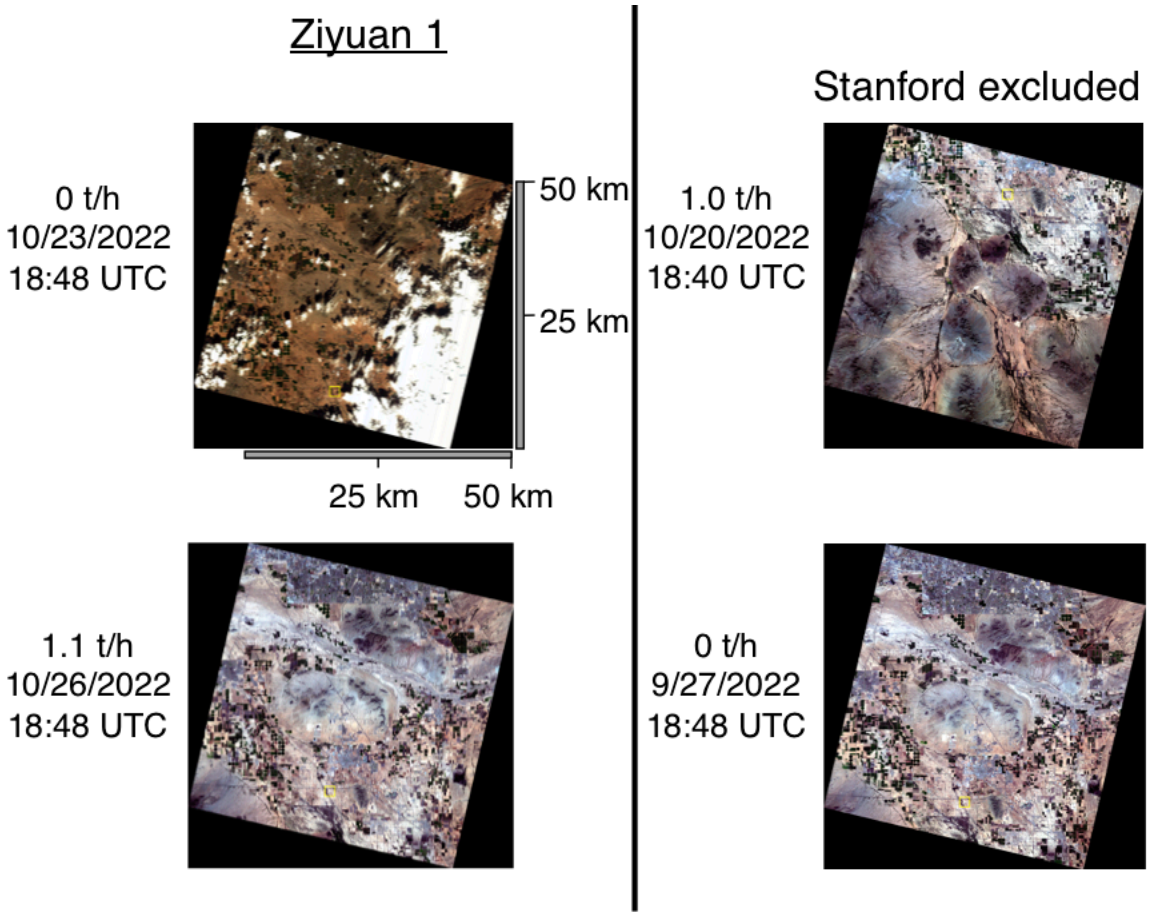


Figure 72. Wider field-of-view optical images of the release site derived from Ziyuan 1 spectral data. The 2x2 km area around the release point is highlighted in a yellow square.

S.4.8. Sky photographs

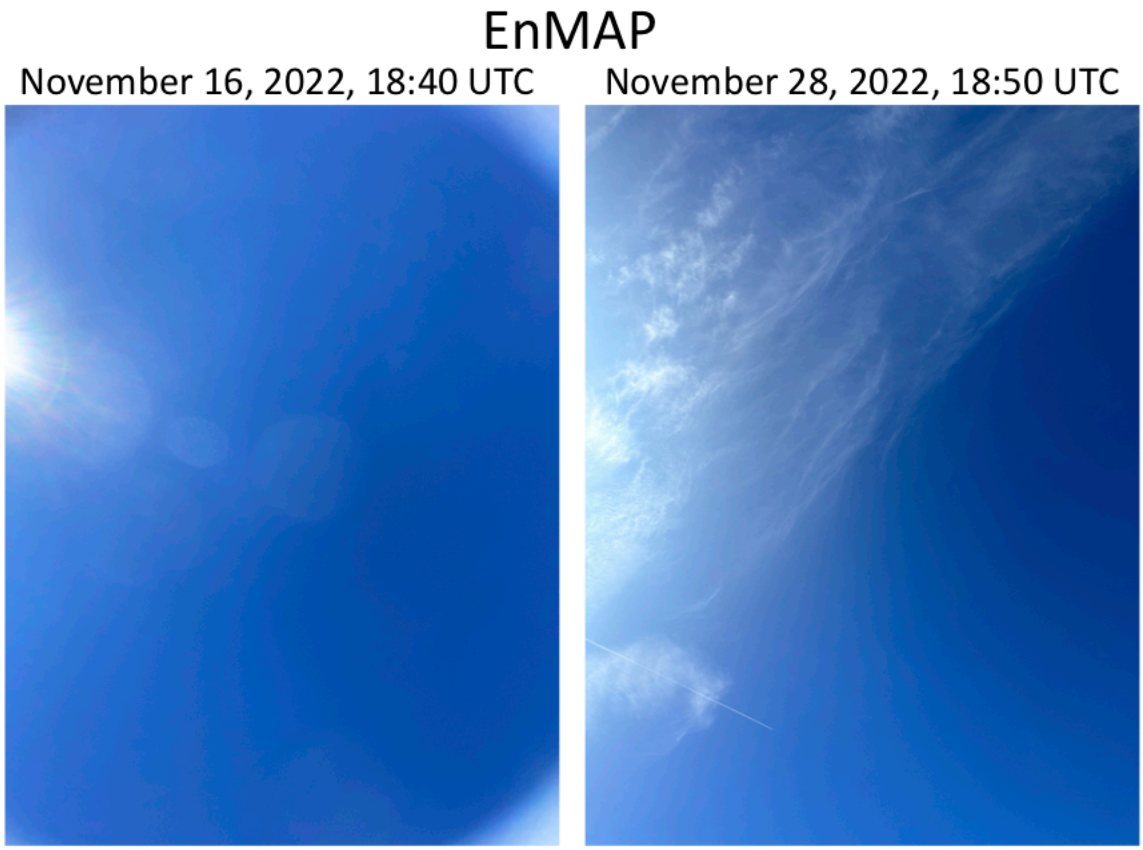


Figure 73. Photographs of the sky above the release site, taken by Stanford researchers near EnMAP satellite overpass times. The Stanford team did not take sky photographs for the November 11th, 13th, 20th, or 24th overpasses, all of which had zero methane emissions.

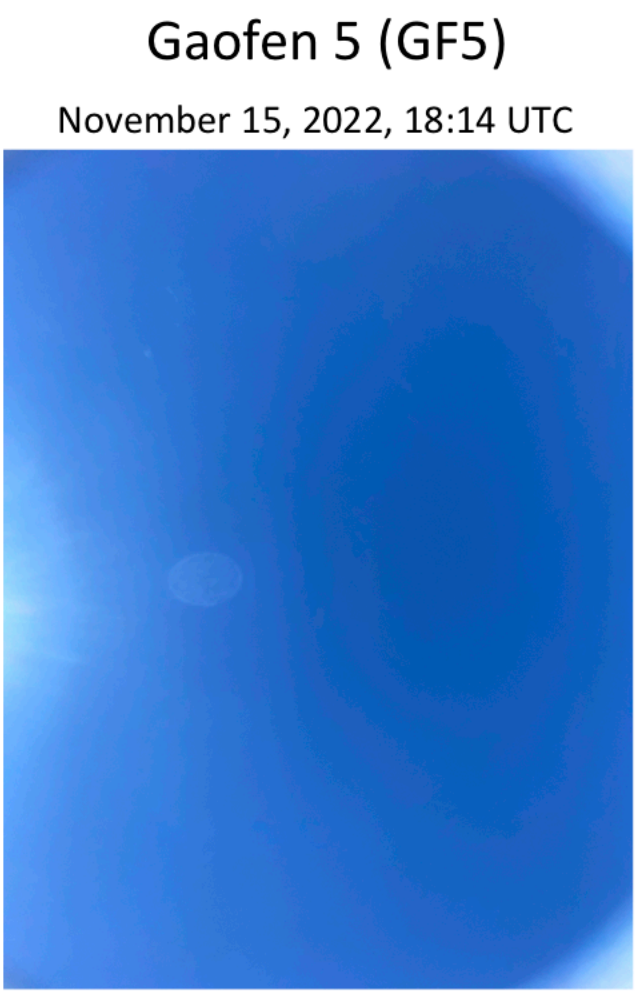


Figure 74. Photographs of the sky above the release site, taken by Stanford researchers near Gaofen 5 (GF5) satellite overpass times. The Stanford team did not take sky photographs for the September 18th overpass, which had zero methane emissions and occurred prior to the start of the experiment.

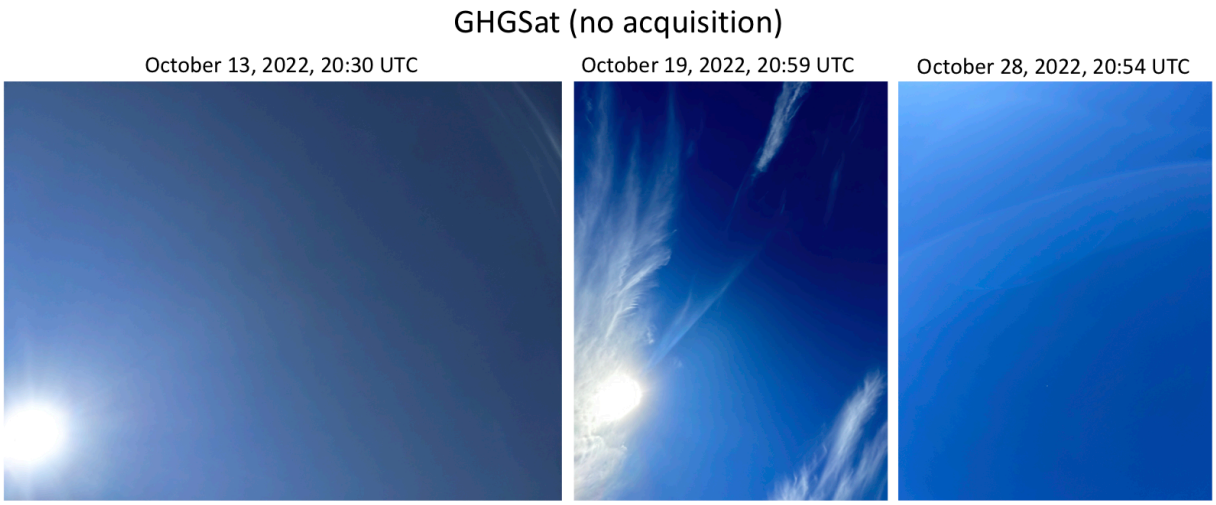


Figure 75. Photographs of the sky above the release site, taken by Stanford researchers near GHGSat satellite overpass times during October, when the satellite was not tasked due to a miscommunication. The Stanford team did

not take sky photographs for the October 21st and 22nd overpasses, during which the Stanford team was troubleshooting on-site hardware systems.

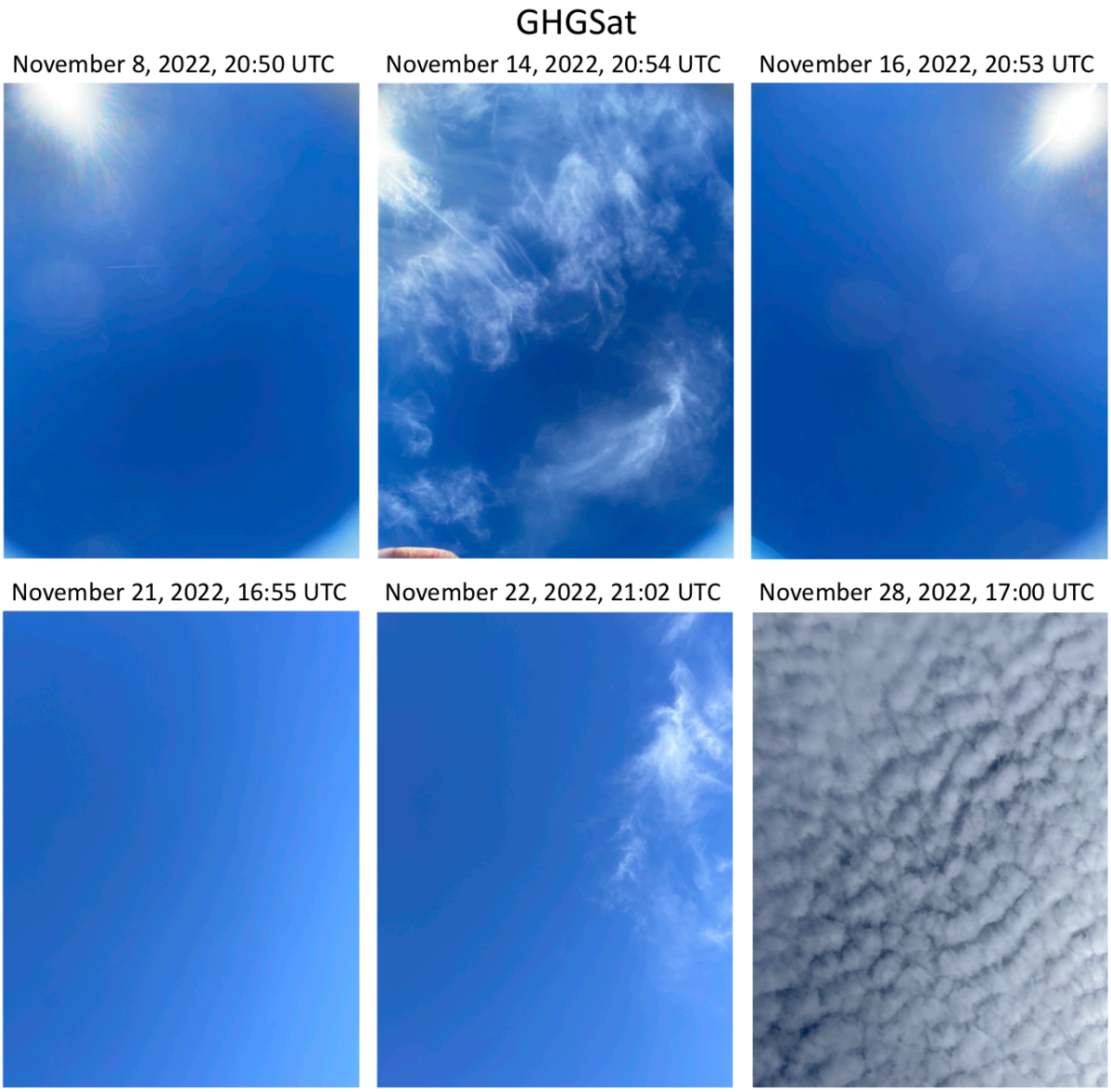


Figure 76. Photographs of the sky above the release site, taken by Stanford researchers near all GHGSat overpass times in November.

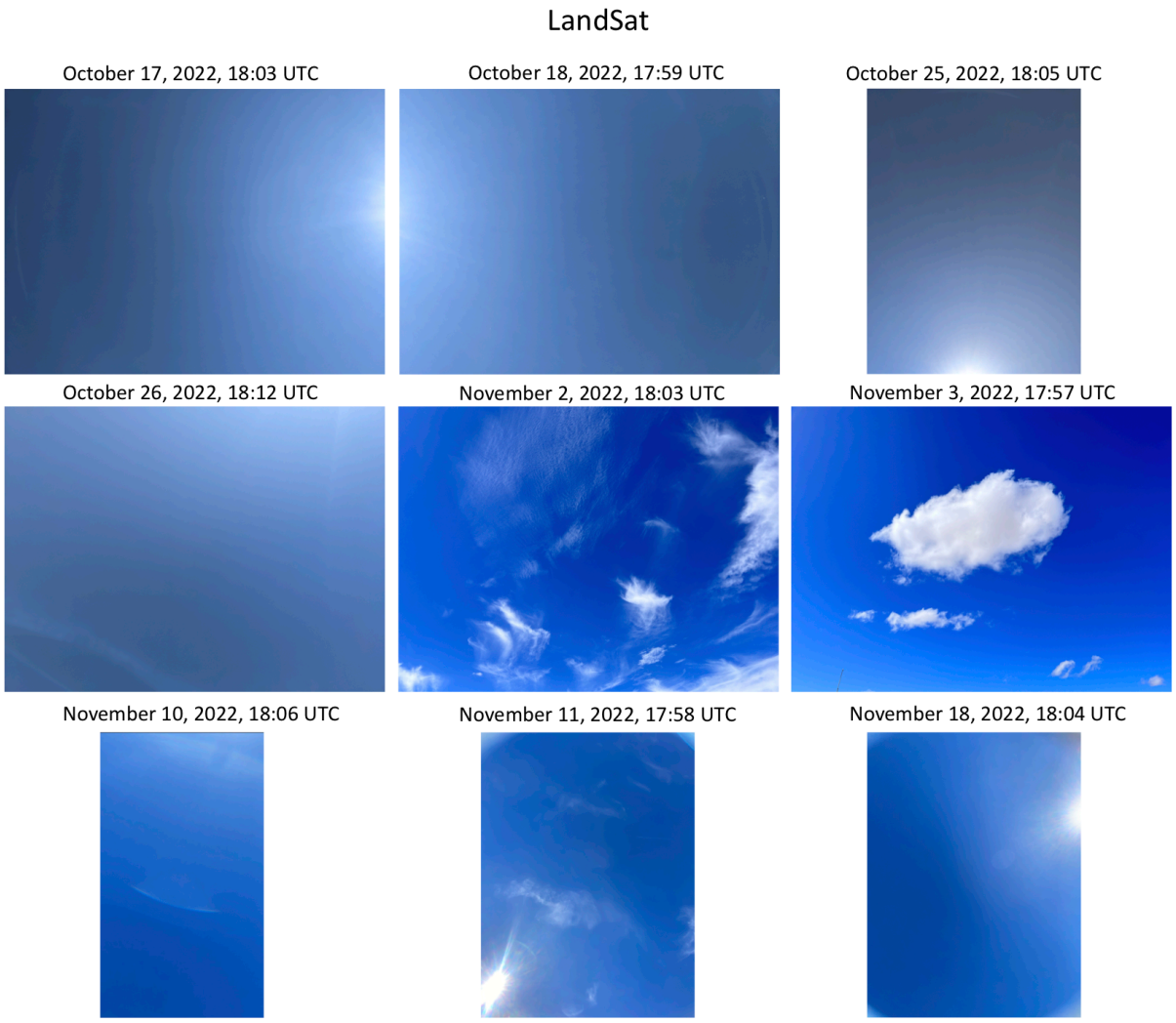


Figure 77. Photographs of the sky above the release site, taken by Stanford researchers near LandSat overpass times. The Stanford team did not take a sky photographs for the October 10th overpass, which had zero methane emissions.

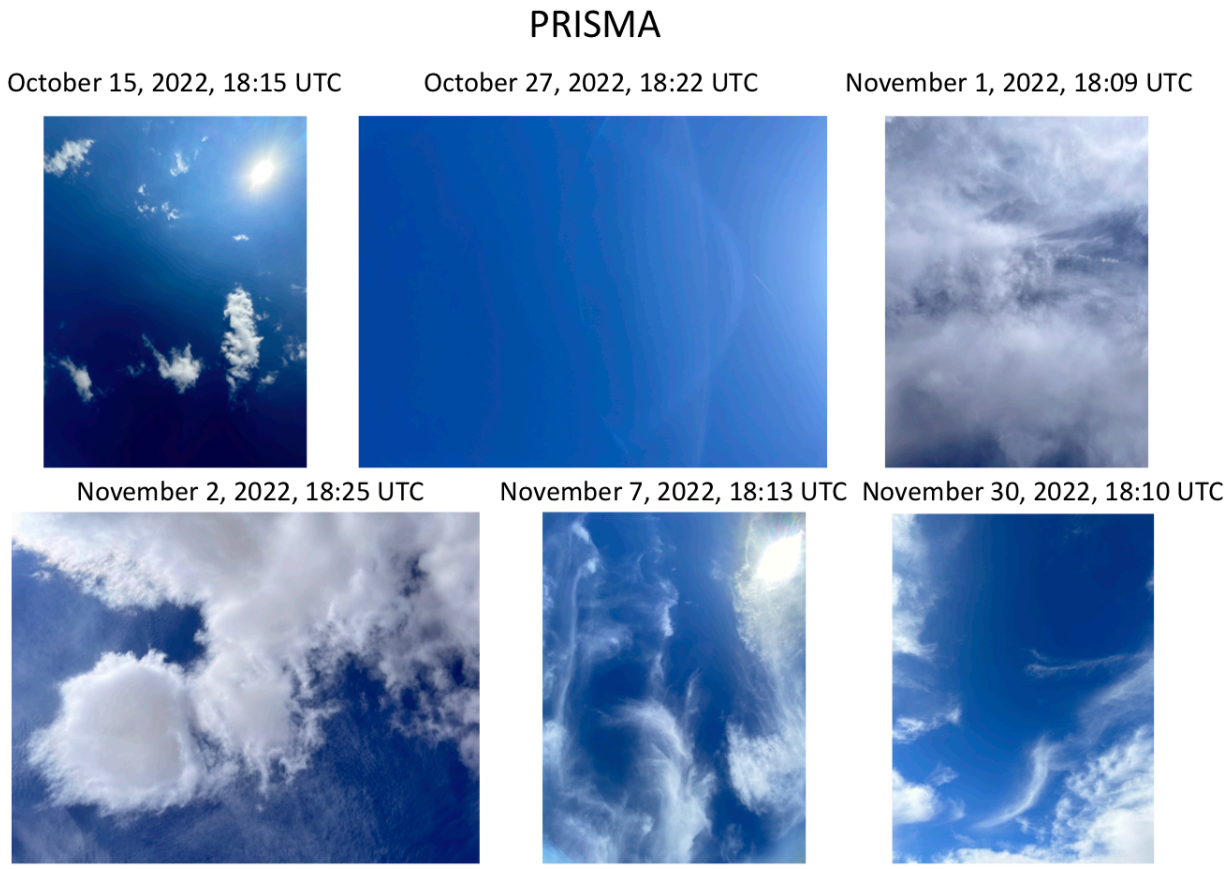


Figure 78. Photographs of the sky above the release site, taken by Stanford researchers near PRISMA overpass times. The Stanford team did not take a sky photographs for the October 21st and November 13th, 19th, and 25th overpasses, all of which had zero methane emissions. On October 21st, the Stanford team was conducting system troubleshooting and cancelled gas releases; all the November dates were weekends, and the Stanford team could not be present at the field site due to personnel shortage.

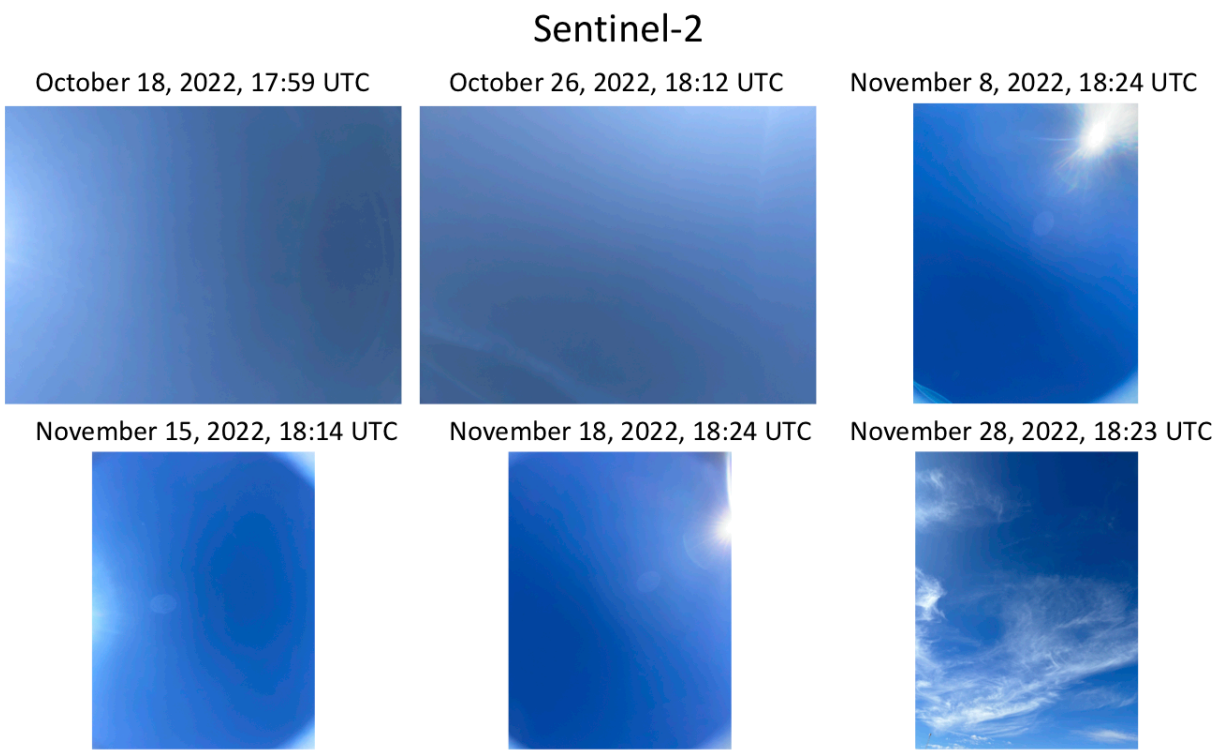


Figure 79. Photographs of the sky above the release site, taken by Stanford researchers near Sentinel-2 overpass times. The Stanford team did not take a sky photographs for the November 5th and 25th overpasses, which had zero methane emissions. The Stanford team could not be present at the field site on these dates due to personnel shortage.

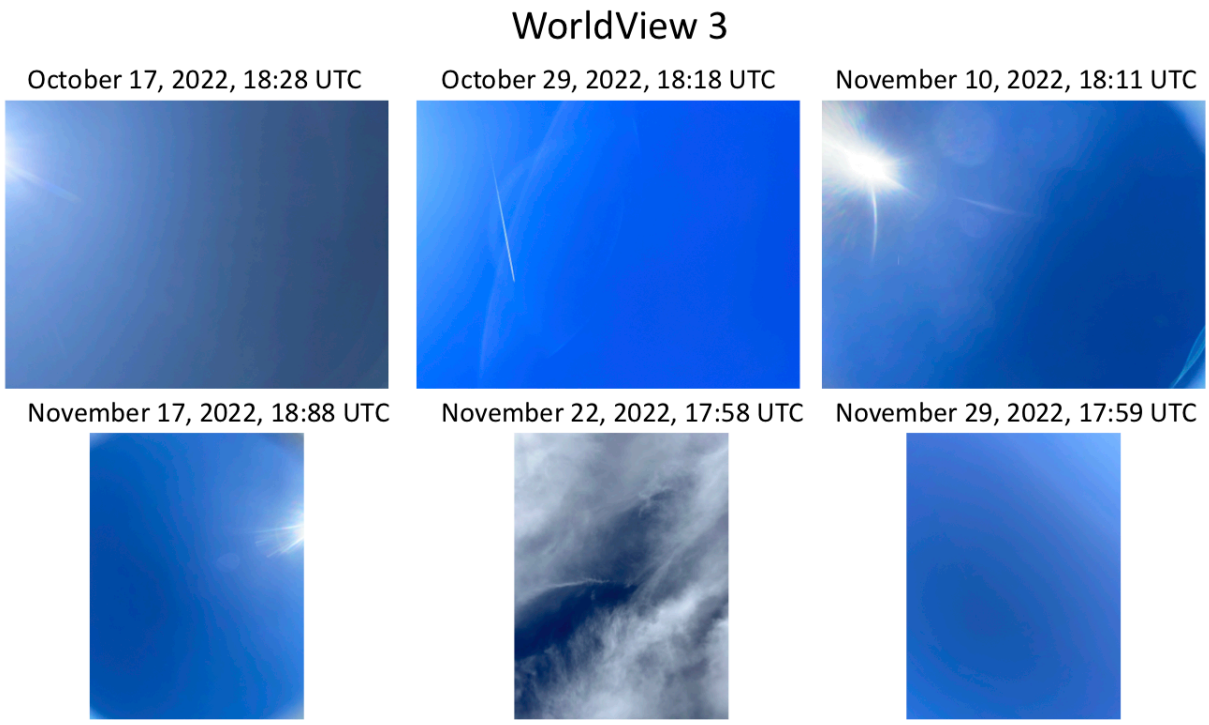


Figure 80. Photographs of the sky above the release site, taken by Stanford researchers near Sentinel-2 overpass times. The Stanford team did not take a sky photographs for the October 10th and 22nd and November 5th and 24th overpasses, all of which had zero methane emissions.

S5. Supplementary references

(1) Sherwin, E. D. Single-Blind Validation of Space-Based Point-Source Detection and Quantification of Onshore Methane Emissions. *Scientific Reports* **2023**. https://doi.org/10.1038/s41598-023-30761-2.
(2) Hayden, A.; Christy, J. Maxar's WorldView-3 Enables Low-Concentration Methane Detection from Space.